

Adam Mickiewicz University in Poznan
Faculty of Physics
Division of Molecular Biophysics



Mechanical properties of polymer colloidal crystals exposed to supercritical fluids

*A thesis submitted in partial fulfillment of the requirements for the degree of
Doctor of Philosophy in Physics*

Mgr Jeena Varghese

PhD Supervisor:

Dr. hab. Bartłomiej Graczykowski, prof. UAM

Poznań, September 2023

Declaration

I hereby declare that except where specific references are made to the work of others, the contents of this dissertation are original and have not been submitted in whole or part for consideration for any other degree or qualification in this or any other university. This dissertation is my work, and all the contents of the dissertation have been obtained by legal means.

Poznan, 14.09.2023

Jeena Varghese

This research work has received funding from:

Foundation for Polish Science (FNP) under the project entitled:

“*Photomechanical hybrid membranes nanomechanics* (PHNOM). (POIR.04.04.00-00-5D1B/18);

Principal Investigator: Dr. hab. Bartłomiej Graczykowski

(MARCH 2019 - JUNE 2022)



“ID-UB” and “University of Tomorrow” project under Adam Mickiewicz University - for participation in international conferences and summer school.

Let there be light, and there was light

Genesis 1:3

Dedication

To my beloved amma and papa for their generous love and support throughout my life.

To all my dearest teachers who inspired me to learn and explore.

Contents

ABSTRACT.....	7
STRESZCZENIE.....	9
LIST OF PUBLICATIONS.....	11
LIST OF ABBREVIATIONS.....	12
FREQUENTLY USED SYMBOLS.....	13
CHAPTER 1 INTRODUCTION.....	15
1.1 Colloidal Assembly.....	15
1.1.1 Applications of colloidal assembly.....	19
1.1.2 Nanoscale soldering of CCs.....	20
1.2 Theory of Elasticity.....	23
1.2.1 Strain Tensor.....	23
1.2.2 Stress tensor.....	25
1.2.3 Hooke's Law.....	26
1.3 Vibration spectroscopy of Colloidal crystals.....	28
1.3.1 Lamb modes in spherical particles.....	28
1.3.2 Colloidal crystals as phononic crystals.....	30
1.3.3 Core-shell structures.....	32
1.3.4 Temperature-dependent vibrational modes.....	34
1.3.5 Mechanical reinforcement of PS CCs by supercritical fluids.....	36
1.4 Thesis outline.....	41
CHAPTER 2 BRILLOUIN LIGHT SCATTERING.....	42
2.1 Theory of light scattering	42
2.2 Brillouin light scattering.....	45
2.3 BLS instrumentation.....	48
2.3.1 Tandem Fabry-Perot interferometer.....	48

CHAPTER 3 SYNTHESIS AND CHARACTERIZATION OF POLYSTYRENE COLLOIDAL CRYSTALS.....	53
3.1 Synthesis of polystyrene NPs.....	53
3.2 Fabrication of PS CCs.....	54
3.3 Characterization by in-situ high-pressure BLS and SEM.....	55
CHAPTER 4 ELASTIC PROPERTIES OF SUPERCRITICAL FLUIDS.....	64
CHAPTER 5 PS CCS IN HIGH PRESSURE HE GAS.....	73
5.1 Brillouin light scattering experiment	73
5.2 Pressure-dependent vibrational frequencies.....	73
5.3 Acoustic impedance contrast between PS and gas.....	76
5.4 BLS experimental results.....	78
CHAPTER 6 PS CCS IN HIGH PRESSURE AR GAS	86
6.1 BLS experimental results.....	87
CHAPTER 7 PS CCS IN HIGH PRESSURE N2 GAS.....	93
7.1 BLS experimental results.....	93
7.2 Size-dependence of nano-scale soldering of PS CCs with different supercritical gases.....	96
CONCLUSION AND OUTLOOK.....	98
REFERENCES	100
JOURNAL CONTRIBUTIONS	111
ACKNOWLEDGEMENTS.....	125

Abstract

Engineering materials at the nanoscale has been a matter of great excitement to the scientific community, with the growing potential applications in daily life. The advances in nanofabrication technologies and multifunctional materials have led to research on novel effects and inventions. When confined at the nanoscale, materials exhibit unique properties that are different from their bulk counterparts. Therefore, evaluating their fundamental properties is as critical as developing novel materials and structures.

Colloidal crystals (CCs), created by the self-assembly of micro- or nanoparticles, have promising applications in phononics, photonics, and nanolithography. However, CCs are fragile due to the weak van der Waals forces that bind the self-assembled particles. The fragility of CCs is a critical issue that can affect the efficiency of devices made out of self-assembled CCs. Moreover, micro and nano contamination, resulting from the disassembled parts of the CCs, can lead to significant environmental and health hazards. To this date, several methods have been introduced to fabricate robust CCs, which include both physical and chemical methods. Some examples are thermal annealing, surfactant decoration, core-shell-based method, and UV irradiation, to name a few. “Cold soldering” is a novel, low-cost, low-effort, chemical-free, and homogeneous method for the fabrication of large-area mechanically reinforced polymer CCs ¹. Cold soldering is based on the plasticization of polymer nanoparticles by exposure to high hydrostatic gas pressure. Cold soldering at specific gas and pressure treatment can occur at temperatures much lower than the glass transition temperature of the polymer. This process leads to permanent physical bonding between the particles in the CC while maintaining their shape and periodicity.

This thesis reports the experimental studies of using different supercritical fluids, such as He, N₂, and Ar, for the mechanical reinforcement of polystyrene (PS) CCs at room temperature, examined by Brillouin light scattering (BLS). Brillouin light scattering is a non-destructive and contactless optical technique that probes acoustic vibrations of CCs in situ. Foremost, BLS enables in situ the evaluation of mechanical properties, such as the effective elastic modulus of CCs at varied gas pressure and temperature.

This work investigates CCs made of PS NPs of different particle sizes ranging from 143 nm to 830 nm. Evaluating the permanent change in the effective elastic modulus of CCs following cold soldering, enabled quantification of the dependence of nanoparticle size on the strengthening of

interparticle contacts. The most efficient soldering occurs for mid-sized nanoparticles (approximately 610 nm diameter) that exhibit nonmonotonic dependence on the particle size. This behavior can be related to intrinsic fabrication impurities, which play a vital role in reducing the free surface of nanoparticles exposed to plasticization by supercritical fluids. The most efficient soldering of PS NPs is made possible by supercritical Ar, a good solvent for polystyrene. The exposure to supercritical N₂ results in the moderate soldering of PS CCs. In contrast, high-pressure He treatment gives negligible soldering. Thus, the process is entirely reversible.

The experimental results can be utilized in the mechanical engineering of 2D and 3D structures based on polymer CCs. Utilizing different parameters like pressure-temperature conditions, nanoparticle size, shape, material, time of gas exposure, and solubility of gas, we can engineer the mechanical properties of polymer CCs, thus leading to robust structures. Brillouin light scattering as a non-destructive tool is very helpful in measuring the contact mechanics of colloidal nanostructures.

Streszczenie

Właściwości mechaniczne polimerowych kryształów koloidalnych poddanych działaniu płynów nadkrytycznych

Materiały wytwarzane w nanoskali wzbudzają ogromne zainteresowanie społeczności naukowej ze względu na ich rosnący potencjał zastosowań w życiu codziennym. Postęp w technologiach projektowaniu i nanoprodukcji materiałów wielofunkcyjnych doprowadził do odkrycia nowych zjawisk i opatentowania związanych z tym wynalazków. Materiały ograniczone do nanoskali wykazują unikalne właściwości, różniące się od tych, które obserwujemy w makroskali. Dlatego ocena podstawowych właściwości nanomateriałów jest tak samo ważna, jak dalsze projektowanie i wykonanie nowych struktur i urządzeń, które na nich bazują.

Kryształy koloidalne (CC) powstałe w wyniku samoorganizacji mikro- i nanocząstek, mają obiecujące zastosowania w fononice, fotonice i nanolitografii. Jednakże CC są kruche ze względu na niewielką wielkość sił van der Waalsa, które wiążą samoorganizujące się cząstki. Kruchość CC jest kluczowym problemem, który może mieć wpływ na wydajność urządzeń wykonanych z samoorganizujących się CC. Co więcej, mikro- i nanostruktury powstałe w wyniku uszkodzeń CC mogą prowadzić do zanieczyszczeń środowiska naturalnego. Do chwili obecnej wprowadzono kilka metod wytwarzania wytrzymałych CC, które obejmują zarówno metody fizyczne, jak i chemiczne. Są to m.in.: wygrzewanie, chemiczna funkcjonalizacja powierzchni, metoda oparta na nanocząstkach typu rdzeń-powłoka, czy napromienianie UV. „Lutowanie na zimno” to nowatorska, niskokosztowa, niewymagająca wysiłku, wolna od środków chemicznych i jednorodna metoda wytwarzania wielkopowierzchniowych, wzmocnionych mechanicznie polimerowych CC. Lutowanie na zimno polega na plastyfikacji nanocząstek polimerowych pod wpływem gazów o wysokim ciśnieniu. Lutowanie na zimno przy określonej obróbce gazowej i ciśnieniowej może zachodzić w temperaturach znacznie niższych niż temperatura zeszklenia polimeru. Proces ten prowadzi do trwałego fizycznego wiązania pomiędzy cząstkami w CC przy zachowaniu kształtu indywidualnych nanocząstek i ich uporządkowania.

Niniejsza praca opisuje badania eksperymentalne wykorzystania różnych płynów nadkrytycznych, takich jak He, N₂ i Ar, do mechanicznego wzmocnienia polistyrenowych (PS) CC w temperaturze pokojowej, badanych metodą rozpraszania światła Brillouina (BLS). Rozpraszanie światła Brillouina to nieniszcząca i bezdotykowa technika optyczna, która pozwala na badania termicznie

wzbudzonych wibracji akustyczne (GHz). Przede wszystkim, BLS umożliwia ocenę *in situ* właściwości mechanicznych, takich jak efektywny moduł sprężystości CC przy różnym ciśnieniu i temperaturze gazu.

W pracy tej zbadano CC wykonane z nanocząstek PS o różnych średnicach w zakresie od 143 nm do 830 nm. Ocena trwałej zmiany efektywnego modułu sprężystości CC po lutowaniu na zimno umożliwiła ilościowe określenie zależności wzmocnienia kontaktów międzycząstkowych od wielkości nanocząstek. Zależność ta okazała się niemonotoniczna z maksimum dla nanocząstek o średnicy około 610 nm. Wiążemy to zachowanie z wewnętrznymi zanieczyszczeniami produkcyjnymi, które odgrywają istotną rolę w zmniejszaniu swobodnej powierzchni nanocząstek podlegającej plastyfikacji przez płyny nadkrytyczne. Najbardziej wydajne lutowanie nanocząstek PS zachodziło przy udziale nadkrytycznego argonu, który jest dobrym rozpuszczalnikiem dla polistyrenu. Ekspozycja na nadkrytyczny N₂ powodowała umiarkowane lutowanie PS CC. Natomiast obróbka wysokociśnieniowa He wykazała na bardzo słaby efekt lutowania, który w tym przypadku jest całkowicie odwracalny.

Wyniki eksperymentów można wykorzystać w projektowaniu mechanicznych struktur 2D i 3D w oparciu o polimerowe CC. Wykorzystując różne parametry, takie jak warunki ciśnienia i temperatury, wielkość, kształt, materiał nanocząstek, czas ekspozycji na gaz i rozpuszczalność gazu, możemy uzyskać właściwości elastyczne polimerowych CC prowadzące do wytworzenia trwałych struktur o pożądanym właściwościach mechanicznych. Rozpraszanie światła Brillouina jako narzędzie nieniszczące jest bardzo pomocne w pomiarach mechaniki kontaktowej nanostruktur koloidalnych.

List of publications

1. **Jeena Varghese**, Reza Mohammadi, Mikolaj Pochylski, Visnja Babacic, Jacek Gapinski, Nicolas Vogel, Hans-Juergen Butt, George Fytas, Bartlomiej Graczykowski, Size-dependent nanoscale soldering of polystyrene colloidal crystals by supercritical fluids, *Journal of Colloid and Interface Science* 633 (2023) 314–322. <https://doi.org/10.1016/j.jcis.2022.11.090>

Ministerial points: 100 IF_(3 years): 8.613 IF₍₂₀₂₃₎: 9.965

2. Visnja Babacic, **Jeena Varghese**, Emerson Coy, Eunsoo Kang, Mikolaj Pochylski, Jacek Gapinski, George Fytas, Bartlomiej Graczykowski, Mechanical reinforcement of polymer colloidal crystals by supercritical fluids, *Journal of Colloid and Interface Science*, 579, 786–793787, (2020). <https://doi.org/10.1016/j.jcis.2020.06.104>

Ministerial points: 100 IF_(3 years): 8.613 IF₍₂₀₂₀₎: 8.128

3. Thomas Vasileiadis, **Jeena Varghese**, Visnja Babacic, Jordi Gomis-Bresco, Daniel Navarro Urrios, and Bartlomiej Graczykowski, Progress and perspectives on phononic crystals, *Journal of Applied Physics*, 129, 160901 (2021). <https://doi.org/10.1063/5.0042337>

Ministerial points: 70 IF_(5 years): 2.389 IF₍₂₀₂₀₎: 2.546

4. **Jeena Varghese**, Mikolaj Pochylski, Jacek Gapinski, Brillouin Spectroscopy: probing the acoustic vibrations in colloidal nanoparticles, In the book: “Design, Fabrication and Characterization of multifunctional nanomaterials”, Elsevier Ltd. (2022); [10.1016/B978-0-12-820558-7.00010-8](https://doi.org/10.1016/B978-0-12-820558-7.00010-8).

List of abbreviations

CC	colloidal crystal	vdW	van der Waals
NP	nanoparticle	NP-NP	nanoparticle to nanoparticle
PS	polystyrene	PMMA	polymethylmethacrylate
SiO ₂	silicon dioxide	PDMS	Polydimethylsiloxane
<i>fcc</i>	face centered cubic	<i>hcp</i>	hexagonal close packed
1D	one-dimensional	2D	two-dimensional
3D	three-dimensional	3DOMS	3D macroporous materials
UV	ultraviolet	pH	potential of hydrogen
PhCs	photonic crystals	PnCs	phononic crystals
BG	Bragg gap	HG	hybridization gap
BLS	Brillouin light scattering	SEM	scanning electron microscope
RT	room temperature	Ar	argon
N ₂	nitrogen	He	helium
FPI	Fabry-Perot interferometer	BS	back scattering
M	mirror	L	lens
R	reflection	T	transmission
CBS	non-polarizing cube beam splitter	PCBS	polarizing cube beam splitter
CW	continuous wave		

Frequently used Symbols

d (nm) – particle diameter

R (nm) – particle radius

R_{eff} (GPa) – effective radius

p (bar) – gas pressure

T (K) – temperature

T_g (K) – glass transition temperature

T_s (K) – softening temperature

V ($\text{kg}\cdot\text{m}^{-3}$) – volume

f (GHz) – frequency of vibration

f_{11} – frequency of dipolar mode of vibration

f_{12} – frequency of quadrupolar mode of vibration

ω – angular frequency

λ (nm) – wavelength of the laser beam

\mathbf{q} – phonon wave vector

\mathbf{k}_i – incident light wave vector

\mathbf{k}_s – scattered light wave vector

v_l ($\text{m}\cdot\text{s}^{-1}$) – longitudinal sound velocity

v_t ($\text{m}\cdot\text{s}^{-1}$) – transverse sound velocity

$v_{[100]}$ – longitudinal sound velocity in the [100] direction of an *fcc* crystal

n – refractive index

E (GPa) – Young modulus

E_{eff} (GPa) – Effective Young modulus

B (GPa) – Bulk modulus

G (GPa) – Shear modulus

C_{eff} (GPa) – Effective elastic constant

ν – Poisson ratio

ρ ($\text{kg}\cdot\text{m}^{-3}$) – mass density

ρ_{eff} ($\text{kg}\cdot\text{m}^{-3}$) – effective mass density

ρ_{PS} ($\text{kg}\cdot\text{m}^{-3}$) – mass density of Polystyrene

ρ_{air} ($\text{kg}\cdot\text{m}^{-3}$) – mass density of air

M (kg) – mass of the particle

K_{eff} ($\text{kg}\cdot\text{s}^{-2}$) – effective stiffness constant

W (J) – work

$W_{\text{PS-PS}}$ ($\text{J}\cdot\text{m}^{-2}$) – work of adhesion between two PS particles

a_0 (nm) – contact radius

a_0^{JKR} (nm) – contact radius predicted by JKR model

λ', μ' (GPa) – Lamé constants

a, b, c (GPa) – Murnaghan constants

Z ($\text{kg}\cdot\text{m}^{-2}\cdot\text{s}^{-1}$) – acoustic impedance

A (J) – Helmholtz free energy

S ($\text{J}\cdot\text{K}^{-1}$) – entropy

U (J) – internal energy of the system

u_{ik} – strain tensor

δ_{ik} – Kronecker delta function

F_i (N) – force per unit volume

σ_{ik} ($\text{N}\cdot\text{m}^{-2}$) – stress tensor

C_{ijkl} (Pa) – stiffness tensor

(n) – radial component of displacement field

(l, m) – angular component of displacement field

\mathbf{r} – position vector

\mathbf{u} – displacement vector

Chapter 1

Introduction

1.1 Colloidal assembly

“The principles of physics, as far as I can see, do not speak against the possibility of maneuvering things atom by atom. It is not an attempt to violate any laws; it is something, in principle, that can be done; but in practice, it has not been done because we are too big.”

Richard P. Feynman

The art of manipulating individual blocks of structures in the “colloidal world“ has greatly impacted the development of tunable materials and their applications²⁻⁴. Colloidal particles can be considered as building blocks for colloidal crystals (CCs), the same as atoms, molecules, or ions for standard crystals. A colloid generally refers to solid particles or droplets (typically size ranges from 1 nm to 1000 nm) suspended in a solid, liquid, or gaseous medium. In this thesis, colloidal crystals are defined as a highly ordered arrangement of monodispersed micro/nano particles without any suspending medium. The ordered arrangement of mesoscopic particles in CCs makes a periodic superlattice, which offers fascinating properties much different from standard crystals. For example, gem opals, naturally occurring colloidal crystals made out of ordered silica particles formed by sedimentation and hydrostatic compression on the earth crust, show vivid structural colors (Figure 1.1)². The artificially engineered crystals referred to as “synthetic opals” can be made in different environmental effects, such as gravitational sedimentation, electrophoretic deposition, or vertical deposition⁵⁻⁸. Such self-assembled colloidal particles form face-centered cubic (*fcc*) or hexagonal close-packed (*hcp*) structures with a packing fraction of 74% (void volume of 26%)^{2,3}. Therefore, they can be used as templates for fabricating macro-mesoporous materials, often called inverse opals⁹. Although there is no practical limitation with the size range of colloidal particles in a crystal, micrometer or sub-micrometer length scales seem potentially crucial for applications¹⁰. This size range is also convenient for optical and electron microscopic studies, facilitating fine-tuning of particle arrays and architecture^{11,12}. Moreover, CCs made of nanoparticles (NPs) can exhibit unique properties at the nanoscale^{2,3,13,14}.

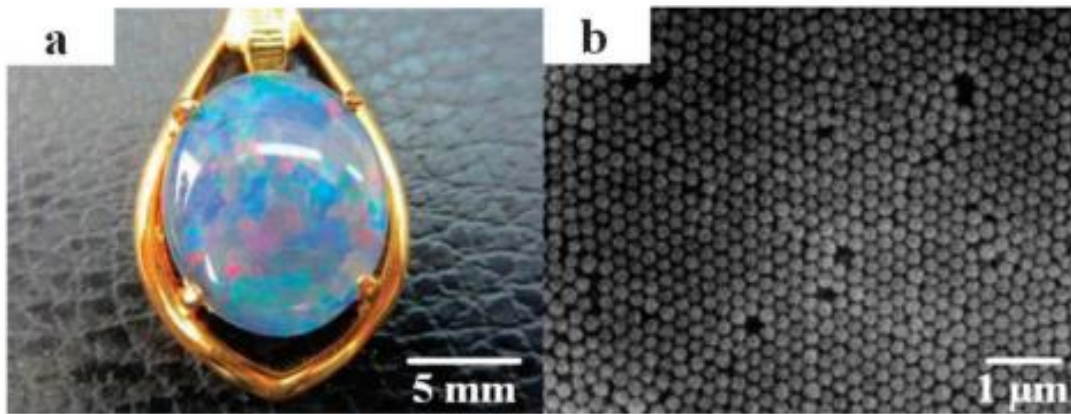


Figure 1.1: (a) The optical image of gem opal-natural colloidal crystal showing structural color (b) SEM image of the silica particle assembly. Adapted with permissions from ref. ².

The possibility of self-assembling monodispersed particles into a perfectly close-packed crystal in a simple and cheap way facilitated the development of fabrication processes and possible applications. Colloidal crystals can be classified into one-dimensional (1D), two-dimensional (2D), or three-dimensional (3D) arrays depending on their spatial structure ^{2,4,15,16}. In recent years, 3D CCs have attained much attention in research due to their ease of fabrication and the highly ordered periodic architecture favorable for photonic and phononic applications ^{17,18}. 3D CCs can be formed by drop casting the particle suspension on a glass slide or silicon wafer, as described in this thesis ^{1,19}. Vertical deposition is another commonly used approach in which a hydrophilic substrate is immersed in colloidal dispersion ²⁰. As shown in Figure 1.2 ²¹, a meniscus is formed in the substrate, and due to the evaporation taking place at the contact phases (substrate, colloidal dispersion, and air), the colloidal particles are transported to the meniscus ²². Thus, an ordered array of particles is formed in the substrate. The thickness of these 3D crystals can be controlled by the withdrawal speed of the substrate from the dispersion. Moreover, the crystallization process is influenced by environmental parameters like temperature and humidity of the surrounding air ^{14,21}.

Two-dimensional CCs, referred to as colloidal monolayers, are potential candidates for functional surface patterns used as templates for nanolithography, filtration membranes, and plasmonic devices ^{23–25}. A vast number of methods have been developed for 2D CC's fabrication so far. Among them, two known approaches are (i) direct assembly at the solid surface and (ii) liquid interface-mediated assembly ^{3,25}. The first approach is based on the deposition of colloidal particles

directly on a substrate. Some examples include spin coating, electrostatic deposition, sedimentation, controlled evaporation, and vertical deposition²⁶⁻²⁹.

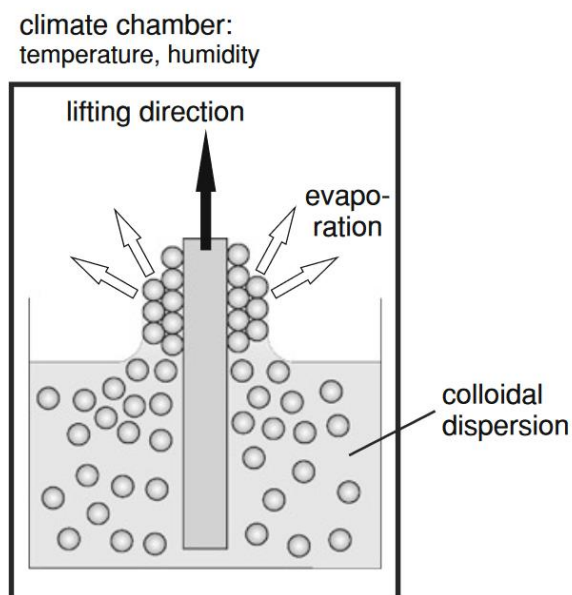


Figure 1.2: Schematic illustration of 3D colloidal crystallization in vertical lifting deposition method. Adapted with permissions from ref.²¹.

Direct assembly methods are the most straightforward approach as they do not need any specialized equipment. However, the choice of transferring substrate is limited and requires properties like hydrophobicity and surface charges. In addition, strict control of experimental and environmental conditions is to be maintained for the perfect crystallization of monolayers. In liquid interface-mediated assembly, the crystallization occurs at the interface between two liquids (e.g., oil-water interface) or on the surface of a liquid (e.g., air-water interface). The formed monolayer is transferred to hydrophobic or topologically modified solid substrates by vertical lifting. As shown in Figure 1.3³⁰, colloidal monolayers can be produced by assembling particles on an air-water interface. The 2D nature of the interface enables crystallization into a perfect close-packed monolayer without forming multiple layers. The colloidal particles on the liquid surface maintain lateral mobility, which permits the particles to assemble in the minimum free energy position, resulting in a hexagonally close-packed crystal. Unlike in direct assembly methods, one major factor in controlling the crystallization process is tuning the composition and nature of the subphase, for example, by changing the pH or adding electrolytes in the subphase. Four forces are critical in this crystallization process: capillary or flotation forces (long-range attractions) and van

der Waals (vdW) forces (short-range attraction), which are counterbalanced by electrostatic repulsion forces and dipole interactions. Lacking the electrostatic repulsion forces can result in disordered particle assembly. Therefore, tuning the nature of the subphase is critical to create a close-packed assembly^{3,25,30}. The nature of the substrate is less important in the liquid-interface mediated method, as the particle assembly is formed on the interface and subsequently transferred to the desired substrate²⁵. The particle size is another important parameter that can influence the self-assembly on the liquid-interface^{31–33}. The monolayer formation is complex for particles less than 100 nm in size compared to bigger particles. Smaller particles experience larger capillary attraction, and hence, they get easily aggregated. Therefore, the surfactant concentration must be adjusted to achieve fewer defects in assembling smaller NPs.

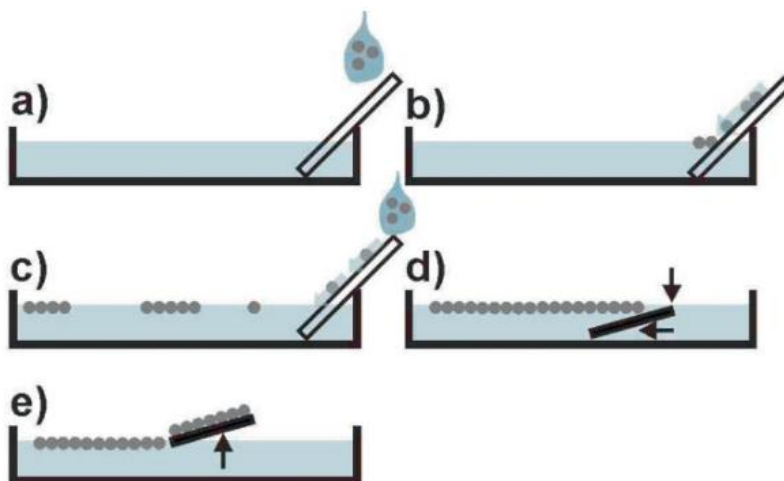


Figure 1.3: Schematic illustration of particle monolayer fabrication. (a, b) addition of particle suspension on the air-water interface using a tilted glass slide. (c) formation of particle monolayer on the interface (d, e) transfer of monolayer by vertical lifting of the glass slide. Adapted with permissions from ref.³⁰.

The fabrication of a one-dimensional chain is quite difficult due to the isotropic gravitational pull in the structure, which limits the formation of the assembly in a particular direction. Special methods, like surface relief grafting, modify the substrate and deposition process to enable the formation of a one-dimensional chain of particles. A Langmuir-Blodgett-based assembly of 1D particle array is shown in Figure 1.4¹⁵. Initially, a 2D particle assembly is formed in the Langmuir-Blodgett trough. By vertically immersing a substrate in the subphase, colloidal particle strings are developed at the contact line of intersection between the substrate and the floating particle monolayer^{2,15}. Recently, silver-coated hollow silica microspheres are assembled using the electric field-induced method to develop conductive one-dimensional particle chains. These particles are

connected through liquid bridges, and the formed 1D array can remain stable outside the synthesizing medium³⁴.

Besides the development of simple architectures, more complex CCs, such as binary³⁵, ternary structures³⁶, size gradient - colloidal crystal³⁷, or supraparticle assembly^{38,39} can also be formed. Moreover, functionalized and core-shell particle assemblies are also widely explored^{2,14,22}.

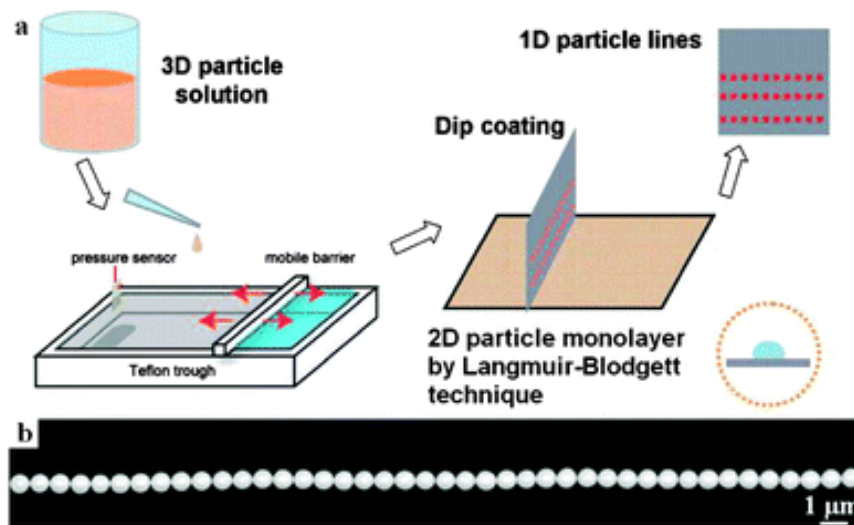


Figure 1.4: (a) Schematic illustration of producing 1D particle strings from the 2D monolayer in Langmuir-Blodgett trough. (b) SEM of the 1D colloidal crystal array. Adapted with permissions from ref. ¹⁵.

Among the various materials available, self-assembled polymer CCs have significant advantages, such as cost-effectiveness, super hydrophobicity, and the possibility to tune geometric features like size and shape⁴⁰⁻⁴². The characteristics of the CCs depend on their architecture and the individual building blocks. From an application point of view, a fundamental understanding of the thermomechanical properties of these structures is inevitable. Notably, such information can help the structural engineering of the CCs for specific purposes^{5,43}. Employing Brillouin light scattering as a powerful, non-destructive optical tool in monitoring the acoustic vibrations of mesoscopic colloidal particles can determine the preferential conditions for the structural engineering of CCs^{1,5,44}.

1.1.1 Applications of colloidal crystals

Highly ordered colloidal crystals have shown great potential in nanolithography^{3,25,45}, coating systems^{40,46-48}, biomolecule separation⁴⁹, photonic devices⁴¹ and materials engineering². Colloidal lithography, using particle monolayers as the lithographic masks, is a flexible and cost-

effective method for the fabrication of nanostructures in long-range order. It has shown great potential in fabricating ordered arrays of nanoparticles, nanotips, nanovoids, nanowires, nanoholes, nanopillars, nanorings, and nanonets^{50,51}. Some examples are; electroless deposition based on polystyrene colloidal masks, which can generate copper nanogrid patterns; floating monolayers can generate silver sulfide nanonets on the air-water interface². Using colloidal monolayers, different shapes of metal nanoarrays can be created. Such ordered metallic arrays based on localized surface plasmon resonance are used to design sensors^{52,53}, photonic devices^{54,55}, and biochips⁵⁶.

Similarly, three-dimensional CCs, due to the 26% void volume, are used as sacrificial templates to create 3D macroporous materials (3DOM)⁵⁷⁻⁵⁹. Subsequently, 3DOMs are used as photonic crystals, sensors, fuel cells, catalysts, and drug-release materials⁶⁰⁻⁶⁵. In addition to 3DOMs, CCs can directly be used as photonic bandgap materials^{66,67}. The perfectly coherent crystals on white light exposure give structural color due to Bragg diffraction, which plays a major role in designing sensors based on photonic crystals⁶⁸⁻⁷¹. Several bioinspired materials- bionic films and coatings mimicking the structural coloration in nature have been realized with self-assembled CCs⁷²⁻⁷⁵. Moreover, the periodic arrangement of particles in CCs can allow or forbid the propagation of classical waves, realizing photonic crystals (PhCs), phononic crystals (PnCs), and plasmonic devices^{55,76-81}.

1.1.2 Nano-scale soldering of CCs

Self-assembled CCs are fragile since they are weakly bonded by short-range van der Waals (vdW) forces^{1,2}. Therefore, the particles can easily detach from the crystal structure under external stress. This is a critical issue that can limit the efficiency of devices made out of CCs, leading to the malfunctioning of these devices. Another major concern is the contamination caused by releasing fragile micro and nano components into the environment. This can accumulate in the body of aquatic organisms, resulting in their mortality, and can be life-threatening⁸²⁻⁸⁴. Thus, colloidal crystals must be structurally robust for different applications². So far, several methods have been reported for producing robust polymer CCs, which include physical and chemical methods^{1,19}. Examples are: making core-shell architecture, plasma-assisted treatment, UV irradiation, thermal annealing, surfactant decoration, and chemical-assisted treatments⁸⁵⁻⁸⁸. Thermal annealing below the glass transition (T_g) of polymer CCs is one of the most straightforward methods to achieve

strong bonding between particles in the self-assembled CCs. However, thermal annealing is not suitable for certain thermosensitive systems, where it can result in sample destruction.

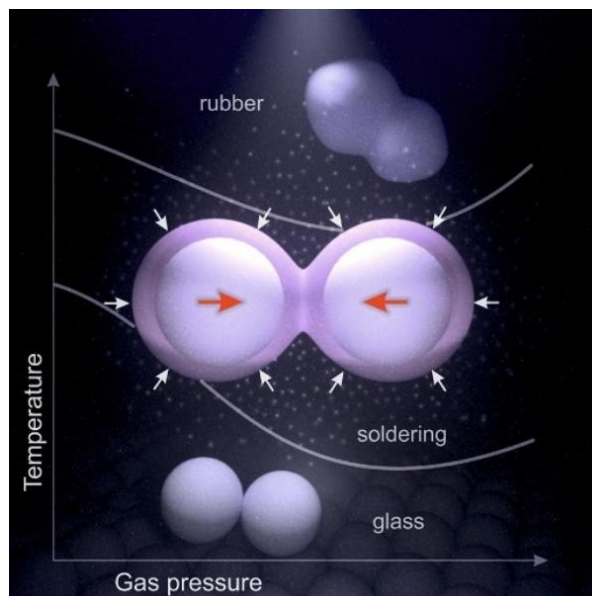


Figure 1.5: (a) Schematic illustration of the concept of cold soldering of PS CCs using supercritical fluids occurring at specific (p, T) conditions. Adapted with permission from ref. ¹.

Cold soldering ¹ based on the plasticization of polymer NPs by exposure to supercritical fluids at high pressure is a simple, low-cost, chemical-free, and homogeneous method for the fabrication of robust CCs. The term “cold” is used as the method does not require high-temperature treatments, which fall close to the glass transition range at normal conditions. In fact, cold soldering refers to the method of increasing NP-NP contact area using supercritical fluids at temperatures well below the glass transition (T_g) of the polymer. The schematic illustration of the concept of cold soldering of PS CCs is shown in Figure 1.5 ¹. Compared to different physical methods for the structural strengthening of CCs, cold soldering gives a global treatment that does not damage the CC by heating. Furthermore, the chemical methods, including pH-based assembly ⁸⁹, surfactant-mediated assembly ³⁸, and core-shell structures of polystyrene with silica/other polymers ^{90,91}, lead to chemical modification of the CC, which is completely avoidable in our technique. Another advantage is that cold soldering does not require sophisticated instrumentation. It has been reported that thermal annealing of PS CCs at 348 K results in 12% increase of NP-NP contact area. However, CCs exposed to 200 bar Ar pressure at the same temperature show 280% increase in the contact area.

Table 1.1: Methods for preparing robust colloidal crystals - comparison

Method	Explanation	Advantage	Disadvantage
Physical Methods			
Cold soldering ¹	Using supercritical fluids - based on gas plasticization	2D/3D Homogeneous, simple and cheap laboratory method Global treatment, no chemical modification of sample.	Works for polymer/soft colloidal crystals depends on solubility of gas, highly modulated elasticity.
Thermal annealing ^{44,92,93}	Annealing within and above glass transition temperature to form thick polymer films from colloidal mono/multilayers	2D/3D systems	Not good for thermosensitive systems, not homogeneous-local treatment Material destruction-periodicity and shape being lost Unable to control the process
Optical microlensing ⁹⁴	Illuminating the colloidal crystal sample with a pulsed laser beam	2D/3D systems Local heating	Non-homogeneous method, sample destruction under laser heating, difficult to control
UV irradiation ⁹⁵	Photochemical crosslinking of PS spheres	2D/3D systems Chemical free	Instrumentation Difficulty in controlling
Chemical methods			
Surfactant-mediated ³⁸	Non-ionic surfactant enhances mechanical stability.		Chemical modification of sample
Crosslinking by organic ligands ⁹⁶	hydrogen/covalent-bonded hydroxyl groups to connect the colloidal particles, sample by dip-coating	Characterization possible by pump-probe spectroscopy	Not uniform method
Haloing type ⁹⁷	segregation of highly charged nanoparticles to regions near negligibly charged colloidal microspheres		Chemical nature of NP becomes different. Affects the chemical stability, No rigid contacts
pH-based particle assembly ⁸⁹	Supraparticle assembly		Chemical modification
Core-shell structure ⁹⁰	PS with other polymers	Room temperature process	Continuous film without voids
PS-Silica core shell ⁹¹	Sol-gel method to produce raspberry structures, altering the electrostatic surface interactions in core-shell		Not uniform, chemically modified structures

Additionally, the effective elastic modulus of CCs is almost doubled after the high-pressure-based treatment ¹. Therefore, treating polymer colloidal crystals at preferential gas pressure and temperature conditions is a much more efficient method for structurally strengthening CCs. The advantages and disadvantages of different methods for preparing robust CCs are listed in Table 1.1.

1.2 Theory of elasticity

The theory of elasticity deals with the deformation of a solid object under the application of any external forces. In this section, we describe the fundamental concepts of stress, strain, and elastic tensors ⁹⁸. For infinitesimally small deformations on solid bodies, linear elasticity, i.e., Hooke's law, can be applied.

1.2.1 Strain tensor

Consider any point P in a solid body, described by the position vector \mathbf{r} with coordinates given by x_i , where $i = 1,2,3$. After the deformation, every point in the body undergoes displacement. Thus, the point P changes to P', the initial position vector \mathbf{r} changes to \mathbf{r}' with coordinates x'_i . The displacement vector is given by,

$$\mathbf{u} = \mathbf{r}' - \mathbf{r} \quad (1.1)$$

In terms of coordinates,

$$u_i = x'_i - x_i, \quad (1.2)$$

where u_i denotes components of the displacement vector.

When the body is deformed, the distance between the points also changes. Consider any two adjacent points, and let dx_i give the position vector that joins them before deformation. The distance between these points is $dl = \sqrt{dx_1^2 + dx_2^2 + dx_3^2} = \sqrt{dx_i dx_i}$. After deformation, the position vector becomes $dx'_i = dx_i + du_i$, and the distance between the points can be given as $dl' = \sqrt{dx_1'^2 + dx_2'^2 + dx_3'^2} = \sqrt{dx'_i dx'_i}$, where the last transformation was obtained using the Einstein summation convention. Consequently:

$$dl'^2 = dx'_i dx'_i = (dx_i + du_i)(dx_i + du_i) \quad (1.3)$$

By substituting $du_i = (\partial u_i / \partial x_k) dx_k$, we can write eq. (1.3) as:

$$dl'^2 = dl^2 + 2 \frac{\partial u_i}{\partial x_k} dx_i dx_k + \frac{\partial u_i}{\partial x_k} \frac{\partial u_i}{\partial x_l} dx_k dx_l. \quad (1.4)$$

In the second term on the right side of Eq. (1.4), the summation is taken over indices i and k . And therefore, we can rewrite it as:

$$\frac{\partial u_i}{\partial x_k} dx_i dx_k = \frac{\partial u_k}{\partial x_i} dx_i dx_k \quad (1.5)$$

By interchanging i and l in the third term of Eq. (1.4), we obtain the final form for dl'^2 as:

$$dl'^2 = dl^2 + 2u_{ik} dx_i dx_k \quad (1.6)$$

where, u_{ik} is the second-order strain tensor defined by:

$$u_{ik} = \frac{1}{2} \left(\frac{\partial u_i}{\partial x_k} + \frac{\partial u_k}{\partial x_i} + \frac{\partial u_l}{\partial x_k} \frac{\partial u_l}{\partial x_i} \right). \quad (1.7)$$

Neglecting the second order term in Eq. (1.7) we obtain:

$$u_{ik} = \frac{1}{2} \left(\frac{\partial u_i}{\partial x_k} + \frac{\partial u_k}{\partial x_i} \right). \quad (1.8)$$

The strain tensor can be represented as a 3×3 matrix given by:

$$u_{ik} = \begin{pmatrix} u_{11} & u_{12} & u_{13} \\ u_{12} & u_{22} & u_{23} \\ u_{13} & u_{23} & u_{33} \end{pmatrix} \quad (1.9)$$

Note that the strain tensor is symmetric ($u_{ik} = u_{ki}$) and it can be diagonalized at any given point. Such obtained diagonal components u_{11} , u_{22} , u_{33} are called principal values of strain tensor and can be named as $u^{(1)}$, $u^{(2)}$, and $u^{(3)}$. The distance dl'^2 can then be expressed by the sum of three independent terms:

$$dl'^2 = (\delta_{ik} + 2u_{ik}) dx_i dx_k = (1 + 2u^{(1)}) dx_1^2 + (1 + 2u^{(2)}) dx_2^2 + (1 + 2u^{(3)}) dx_3^2, \quad (1.10)$$

where $\delta_{ik} = 1$ ($i = k$) or $= 0$ ($i \neq k$) is the Kronecker delta function.

The relative change of elongation along i -th principal axis is given by:

$$\frac{dx'_i - dx_i}{dx_i} = \sqrt{1 + 2u^{(i)}} - 1 \approx u^{(i)}. \quad (1.11)$$

Eq (1.11) is valid for small deformations in the body. With that approximation, the relative volume change of an infinitesimally small volume, $dV \rightarrow dV'$ is given as the sum of the diagonal components (trace) of the strain tensor:

$$\frac{dV' - dV}{dV} = u_{ii} = u_{11} + u_{22} + u_{33}. \quad (1.12)$$

1.2.2 Stress Tensor

For a solid body that is not deformed, the arrangement of molecules remains in a state of thermal equilibrium. The molecular arrangement changes from the initial equilibrium condition when the body is deformed. Therefore, internal forces arise which tend to restore the initial state. These restoring forces associated with deformation are called internal stresses. They are short-range forces acting only with the neighboring points.

Consider a closed volume V ; the total internal force acting on all volume elements in the body is expressed as $\int F_i dV$, where F_i is the force per unit volume. According to Newton's third law, the internal forces within the volume cancel each other, and the resultant force can be written as the sum of the forces acting on the surface. Therefore, F_i can be expressed as the divergence of a second-order tensor:

$$F_i = \frac{\partial \sigma_{ik}}{\partial x_k}. \quad (1.13)$$

The resultant force can be written as an integral over the closed surface bounded by the volume:

$$\int F_i dV = \int \frac{\partial \sigma_{ik}}{\partial x_k} dV = \oint \sigma_{ik} df_k, \quad (1.14)$$

where df_k is the surface element vector normally directed outward and σ_{ik} is the Cauchy stress tensor. The stress tensor is also symmetric, which means $\sigma_{ik} = \sigma_{ki}$. The six independent components of the stress tensor are represented in a matrix form:

$$\sigma_{ik} = \begin{pmatrix} \sigma_{11} & \sigma_{12} & \sigma_{13} \\ \sigma_{12} & \sigma_{22} & \sigma_{23} \\ \sigma_{13} & \sigma_{23} & \sigma_{33} \end{pmatrix} \quad (1.15)$$

where, $\sigma_{11}, \sigma_{22}, \sigma_{33}$ are the normal components that result in the dilation or contraction of the body, while $\sigma_{12}, \sigma_{13}, \sigma_{23}$ are the shear components leading to the change of shape of the body.

The work δW for performing a deformation is related to a change of strain as:

$$\delta W = -\sigma_{ik} \delta u_{ik}. \quad (1.16)$$

If the deformation of the body is small, it can return to its original state when the external forces are removed. Such deformation is called an elastic one. However, if the body continues to stay deformed even after the removal of the external forces, it is called plastic deformation.

For a reversible, elastic deformation, the Helmholtz free energy is given as $A = U - TS$, where T is the temperature, S is the entropy, and U internal energy of the system. Considering an infinitesimal change in internal energy gives $dU = TdS - \delta W = TdS + \sigma_{ik} \delta u_{ik}$.

For the elastic isothermal process, the strain and stress are related to the Helmholtz free energy,

$$\sigma_{ik} = \left(\frac{\partial A}{\partial u_{ik}} \right)_T. \quad (1.17)$$

1.2.3 Hooke's law

For a perfectly elastic body, generalized Hook's law states that each component of the stress tensor is linearly related to each component of the strain tensor⁹⁹:

$$\sigma_{ij} = C_{ijkl} u_{kl}, \quad (1.18)$$

Here, C_{ijkl} are components of a fourth-rank stiffness tensor having $3^4 = 81$ components. Considering the stress and strain symmetry, $C_{jikl} = C_{ijkl}$ and $C_{ijlk} = C_{ijkl}$, the number of components reduces to $6^2 = 36$. The elastic tensor is symmetric, therefore, it can be further reduced to 21 independent components.

The Hooke's law can be written in the matrix form:

$$\begin{pmatrix} \sigma_{11} \\ \sigma_{22} \\ \sigma_{33} \\ \sigma_{23} \\ \sigma_{13} \\ \sigma_{12} \end{pmatrix} = \begin{pmatrix} C_{1111} & C_{1122} & C_{1133} & C_{1123} & C_{1113} & C_{1112} \\ & C_{2222} & C_{2233} & C_{2223} & C_{2213} & C_{2212} \\ & & C_{3333} & C_{3323} & C_{3313} & C_{3312} \\ & & & C_{2323} & C_{2313} & C_{2312} \\ & \text{Symmetric} & & & C_{1313} & C_{1312} \\ & & & & & C_{1212} \end{pmatrix} \begin{pmatrix} u_{11} \\ u_{22} \\ u_{33} \\ 2u_{23} \\ 2u_{13} \\ 2u_{12} \end{pmatrix} \quad (1.19)$$

or in the Voigt notation ¹⁰⁰⁻¹⁰²: $C_{ijkl} \rightarrow C_{KL} (ij \rightarrow K, kl \rightarrow L; K, L = \{1, 2, \dots, 6\})$:

$$\begin{pmatrix} \sigma_1 \\ \sigma_2 \\ \sigma_3 \\ \sigma_4 \\ \sigma_5 \\ \sigma_6 \end{pmatrix} = \begin{pmatrix} C_{11} & C_{12} & C_{13} & C_{14} & C_{15} & C_{16} \\ & C_{22} & C_{23} & C_{24} & C_{25} & C_{26} \\ & & C_{33} & C_{34} & C_{35} & C_{36} \\ & & & C_{44} & C_{45} & C_{46} \\ & \text{Symmetric} & & & C_{55} & C_{56} \\ & & & & & C_{66} \end{pmatrix} \begin{pmatrix} u_1 \\ u_2 \\ u_3 \\ u_4 \\ u_5 \\ u_6 \end{pmatrix} \quad (1.20)$$

The reduction of the independent components of the elastic tensor depends on the symmetry considerations for different crystallographic classes. In the general case, for an elastic isotropic body, the elastic tensor has the form:

$$C_{KL} = \begin{pmatrix} C_{11} & C_{12} & C_{12} & 0 & 0 & 0 \\ C_{12} & C_{11} & C_{12} & 0 & 0 & 0 \\ C_{12} & C_{12} & C_{11} & 0 & 0 & 0 \\ 0 & 0 & 0 & C_{44} & 0 & 0 \\ 0 & 0 & 0 & 0 & C_{44} & 0 \\ 0 & 0 & 0 & 0 & 0 & C_{44} \end{pmatrix} \quad (1.21)$$

In fact, the two non-zero components hold the relation, $C_{11} = C_{12} + 2C_{44}$. The two independent components can be identified as Lamé coefficients, defined as: $C_{12} = \lambda'$ and $C_{44} = \mu'$. Here, C_{11} is called the longitudinal modulus. The shear modulus G is given by:

$$G = \mu' = C_{44}. \quad (1.22)$$

The bulk modulus B gives the material's resistance to uniform compressions:

$$B = \lambda' + \frac{2}{3}\mu', \quad (1.23)$$

where, B is defined as the ratio of the hydrostatic pressure to the fractional volume change.

The Young's modulus E , known as tensile modulus, gives the ratio of longitudinal stress to the longitudinal strain:

$$E = \frac{9BG}{3B + G} \quad (1.24)$$

The Poisson's ratio ν gives the ratio of lateral strain to the longitudinal strain:

$$\nu = \frac{3B - 2G}{2(3B + G)} = \frac{E}{2G} - 1 \quad (1.25)$$

1.3 Vibration spectroscopy of colloidal crystals

The acoustic vibrations of colloidal spheres can be determined by inelastic light scattering^{103–105} or pump-probe techniques^{106,107}. While Raman scattering^{108,109} can access the vibrations of smaller particles ($d < 100$ nm), BLS^{22,110,111} can measure the vibrational dynamics of mesoscopic colloids (size of a few hundred nanometers).

1.3.1 Lamb modes in spherical particles

Horace Lamb developed the theoretical description of the vibrational modes in free homogeneous spheres in 1881¹¹². These eigenmodes are classified as torsional and spheroidal modes and are indicated by three indices (n, l, m) , where (n) refers to the radial and (l, m) the angular dependence of the displacement field. Similar vibrational modes have been discovered in giant spheres like Earth¹¹³. Torsional modes are fully tangential. Therefore, it involves only pure shear motion and no radial displacement. Torsional modes do not contribute to the BLS intensity^{111,114}. Spheroidal modes exhibit both shear and stretching motion. Hence, they are indicated by two indices (n, l) , where $(n = 1, 2, 3, \dots)$ and $(l = 0, 1, 2, \dots)$. Spheroidal modes with $l = 0$ have purely radial displacement, and are called breathing modes. Figure 1.6 schematically illustrates breathing $(1, 0)$, dipolar $(1, 1)$ and quadrupolar $(1, 2)$ spheroidal Lamb modes.

To date, BLS selection rules for spheroidal modes have been modified several times. Duval proposed that for particles smaller than the excitation wavelength ($d \ll \lambda$), only $l = 0, 2$ are Raman active¹¹⁵. According to Li et. al. for $(d \approx \lambda)$, only even spheroidal modes are Brillouin active¹¹⁶. Recently, Montagna reported that, from the theory of Brillouin scattering, for particles having size comparable to the excitation wavelength ($d \approx \lambda$), all spheroidal modes are Brillouin active^{111,114}.

The Brillouin active spheroidal modes have a frequency close to the phonon frequency in the bulk material, $\omega(n, l) = 2\pi f(n, l) \sim qv_1$, where, q is the phonon wavevector and v_1 is the longitudinal sound velocity. The intensity of each (n, l) mode is acquired as the sum of the intensities of $2l + 1$ components¹¹⁴. An example of the BLS spectra obtained for silica CC with eigenmodes assigned are given in Figure 1.7¹¹⁰.

The intensity of a specific mode (n, l) depends on the product qR , where $R = \frac{d}{2}$, is the radius of the spherical particle. This relation shows that a distinct q - dependence is observed for the BLS spectra of all spherical particles. However, experimentally for dry colloidal opals, q - dependence is lost due to the strong multiple scattering from the particles¹¹⁰. The q - independent BLS measurements, based on the frequency of the vibrational mode, can provide information on the mechanical properties of colloidal spheres, as described in this thesis.

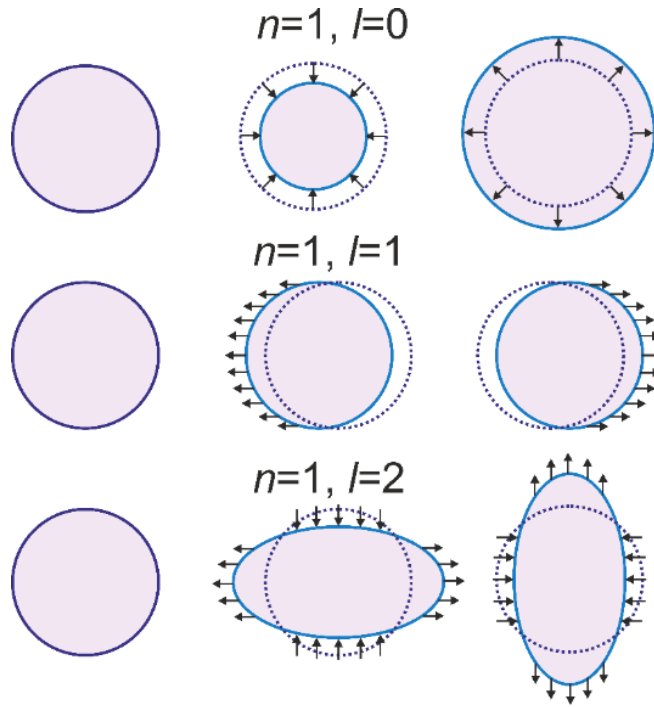


Figure 1.6: Illustration of (a) breathing, (b) dipolar, and (c) quadrupolar spheroidal Lamb modes.

Solving the wave equation for the elastic spheres, the frequency of the eigenmodes is obtained from the formula:

$$f(n, l) = \frac{A_{n,l}v_T}{d}, \quad (1.26)$$

where $A_{n,l}$ is the dimensionless factor that depends on Poisson's ratio, v_T denotes transverse velocity, and d is the diameter of the spherical particle. The sound velocity can be connected to the shear modulus as:

$$G = \rho v_T^2, \quad (1.27)$$

Therefore, the vibrational frequencies depend on the particle diameter d , the mass density ρ and the modulus of elasticity. Obtaining the eigen frequencies by appropriate theoretical fits of the observed peaks in the BLS spectra, the mechanical properties can be ascertained^{44,104}.

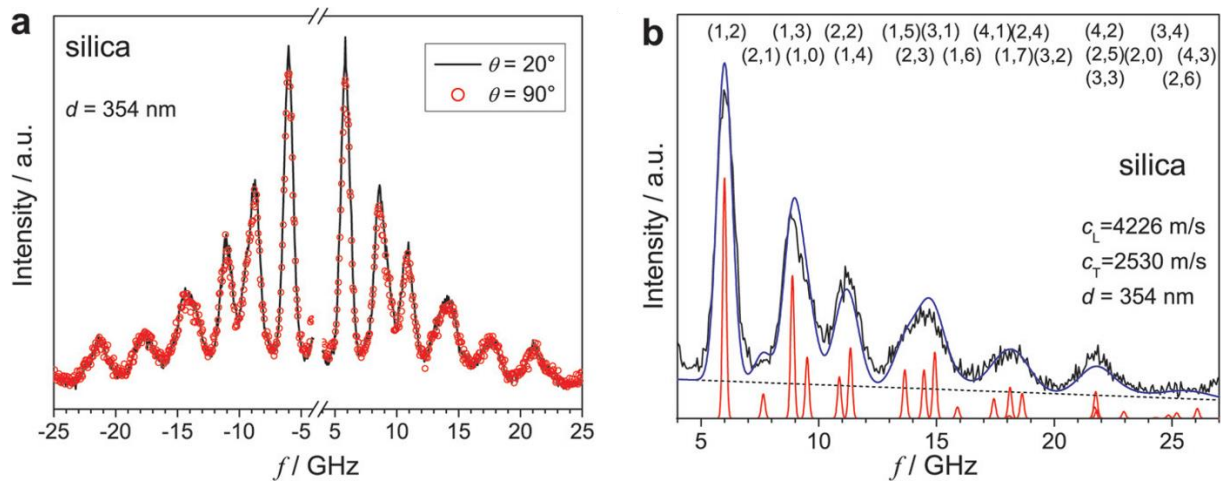


Figure 1.7: (a) BLS spectra of silica NPs measured at different scattering geometries. Comparison of experimental (black lines) and theoretical (blue lines) BLS spectra for (b) silica CCs of 354 nm diameter. The red lines show the individual contributions from various eigenmodes. Adapted with permissions from ref.¹¹⁰.

1.3.2 Colloidal crystals as phononic crystals

The possibility to control and manipulate classical waves propagating through periodic structures emerged as one of the most exciting developments of Modern Physics^{117,118}. "Photonic crystals (PhCs)," which enable the controlled propagation of optical waves through periodic dielectric changes, were first developed as a result of Yablonovitch and John's study on the inhibited emission of photons in 1987^{119,120}. These structures are of great interest because they can prevent light traveling in certain directions at specific frequencies, creating "photonic band gaps"⁷⁷. Similarly, "phononic crystals (PnCs)" - the elastic analog of PhCs, allow the propagation of elastic or acoustic waves at specific frequencies (pass band) through periodic modulation of elastic moduli or mass densities^{5,117,121}. The band gap in PnCs arises from the destructive interference of

diffracted waves in periodic structures, known as the "Bragg gap". For an isotropic medium, the propagation of acoustic waves depends on Lamé's coefficients and material density, in contrast to electromagnetic waves, where it depends on just one parameter, the dielectric constant⁵.

Phonons are produced by the random thermal vibrations of atoms in the material and are the major heat carriers in dielectrics. As a result, many crucial scientific phenomena involving heat transfer and coupling of phonons with photons and electrons can be studied using phononic crystals, with the ability to control the flow of acoustic waves⁵. Recently, hypersonic PnCs, where elastic wave propagation occurs in the GHz frequency range, have attained much attention in research^{79,122–125}. The intense photon-phonon interactions in this frequency regime triggered several communication and information technologies applications.

The fabrication of hypersonic PnCs is particularly demanding, as the periodic pattern should scale in the sub-micrometer range. The advances in nanofabrication and multifunctional materials have enhanced the construction of periodic structures for PnCs¹²². For instance, holographic interference lithography can be used to produce polymer hypersonic PnCs^{124,126}. Self-assembly is another intriguing method that enables relatively easy and affordable fabrication approaches for 2D and 3D high-quality large-area CCs. CCs with well-defined periodic patterns can provide outstanding phononic characteristics. The domain of potential phononic materials can be enriched by using binary or ternary crystals or by altering the interstitial spaces between the particles in the CCs¹²⁷.

The hypersonic bandgap was first reported by Cheng et al.⁷⁶. The sample was a dry PS colloidal opal film prepared by the vertical lifting of the glass substrate from the particle suspension. Due to the strong multiple scattering from dry colloidal opals, the Brillouin spectra of such samples were q -independent. This is caused by the high elastic form factor and significant optical contrast (large difference in refractive index) of polystyrene with the surrounding air. Therefore, it was impossible to measure the phonon dispersion relation $\omega(q)$. The subsequent dry samples can be infiltrated with a viscous, non-evaporative (inert for PS) liquid to avoid numerous scattering effects and achieve a well-defined scattering wave vector magnitude (q).

The Bragg gap develops due to the band folding, which was represented by splitting a single Brillouin peak into a doublet across the Brillouin Zone (BZ) boundary. The discovered longitudinally polarized phonon dispersion relation revealed a 0.4 GHz wide Bragg gap at 5 GHz. The propagation of phonons within this frequency range was forbidden. The absence of particle

modes after infiltration concentrated on the hybridization gap between continuum acoustic band and resonance band ($l=2$). This occurred due to the system components' poor elastic contrast and the significant dissipation of elastic energy into the liquid medium ¹²⁸. The periodic structure length, which should be in the order of the phonon wavelength, determines whether the Bragg gap forms. If it is equal, the scattered acoustic waves interfere constructively, and the incident wave is fully reflected, which opens the phononic gap ⁵. The width of the Bragg gap was increased by the elastic mismatch between the particles and the fluid. When PS (refractive index, $n = 1.59$) dry opals were infiltrated by PDMS ($n = 1.41$) instead of silicon oil ($n = 1.45$), the increase in the Bragg gap was observed. Direct measurement using BLS in these structures can address the phonon propagation and dissipation issues ⁷⁶.

Several studies on the phononic properties of mesoscopic particles were reported using high-resolution BLS, which gives access to resonance modes of particles and dispersion relations of particle assemblies in a liquid host. The hypersonic bandgap in 2D colloidal crystals was subsequently reported ¹²⁹. In addition to the Bragg gap, the experimental realization of the hybridization gap (HG) was obtained in several systems. The first mention of this is in the BLS experiments of colloidal suspensions ^{130,131} but demonstrated in PS and PMMA wet colloidal opals infiltrated by PDMS ¹³². This gap originates from the interaction between the bands of quadrupolar eigenmode (f_{12}) and the effective medium. In order to check the sensitivity of phononic gaps on the disorder, hybrid colloidal systems were investigated by BLS. Non-crystalline films of PS spheres - binary mixtures with two different diameters in various compositions were investigated, and the BLS spectra showed the superposition nature of the individual components. Interestingly, HG sustains and is inert to the structural disorder, but BG disappears, which is in accordance with the origin of gaps. BG occurs as the effect of crystal structure, whereas HG is dependent on particle resonances unmodified by the sphere arrangements. These materials may have potential applications in vibration isolators and acoustic shields ⁵.

1.3.3 Core-Shell structures

Recently, polymer-based colloidal composites have gained much attention in research. The vibrational modes of the individual spheres depend on the structural and geometrical features. Still et al., for the first time, reported the vibrational modes of core-shell structures using Brillouin light scattering ¹⁴. The sample was sub-micrometer SiO₂-PMMA core-shell spheres with a constant core

radius but variable shell thickness. BLS can investigate all of the accessible thermally stimulated vibrational modes in a single experiment.

Figure 1.8 displays BLS spectra of bare silica and core-shell particles with increasing shell thickness. The orange spheres represent the experimental frequency values, whereas the blue lines show the theoretical values; both are in agreement with one another. Only two resonance modes were observed for SiO₂ spheres. However, with the increase of PMMA shell thickness, the BLS spectra got richer, and more modes were observed. The increase in resolved vibrational modes with particle diameter d is dependent on the product qd . In the case of strong multiple scattering, q is taken as twice the back-scattering vector $q \approx 2k_i$. Therefore, the detected modes increase by a factor of $(2k_id)^{11}$.

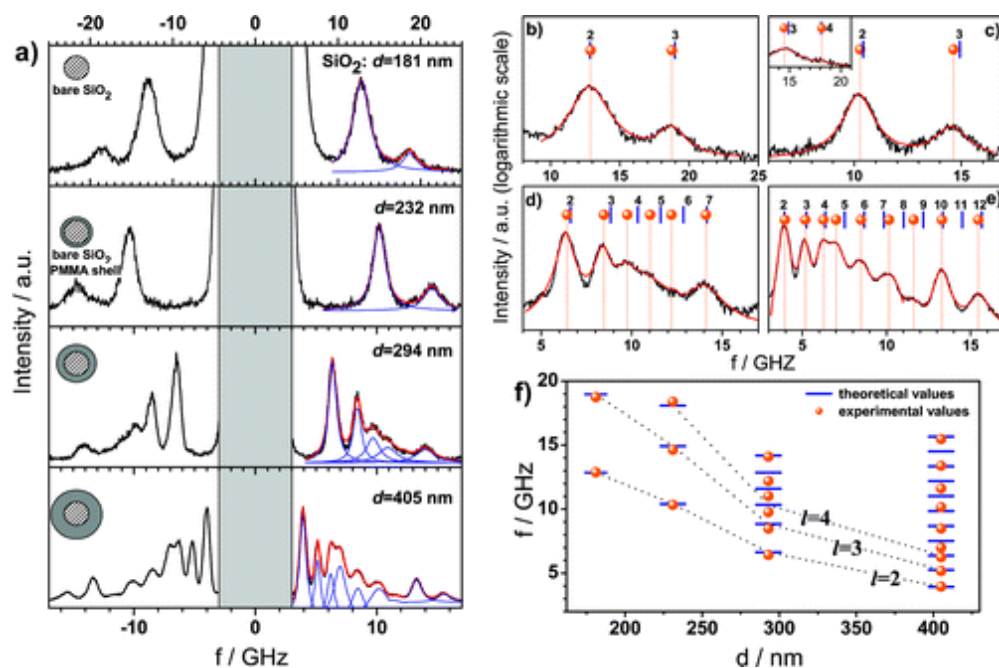


Figure 1.8: (a) Brillouin spectra of SiO₂ and SiO₂-PMMA core-shell particles. The enlarged view of Stokes side given in (a) for (b) bare silica (c-e) core-shell spheres with variable PMMA thickness. (f) comparison of experimental and theoretical frequency values. Adapted with permissions from ref. ¹⁴.

The sound velocities of the silica spheres are calculated from the experimental and theoretical data, which are significantly lower than the bulk values indicating the porosity of silica spheres. Thus, the BLS experiment becomes a necessary tool to avoid the wrong calculation assumptions. Usually, the experimental results are verified with theoretical calculations to generate a better fitting of the results. This agreement allowed the calculation of elastic constants and core density in hybrid structures. An exciting increase in the elastic moduli was observed in core-shell

structures. The nature of hollow capsules of PMMA after dissolving the silica core was also studied, and it verified that the elastic constants are not affected by the removal of the core. These studies can be extended to selectively nanostructured colloids ¹⁴.

Several core-shell particles were investigated via BLS ^{133,134}, tailoring their thermomechanical properties, such as glass transition, surface softening, and elasticity, by varying the shell layers. PS-PMMA (high T_g shell) core-shell structure exhibited an increase in the elastic modulus by shell thickness, whereas a reverse effect is observed in the PS-PBMA (low T_g shell) particles ¹³³. Also, BLS together with the computational methods, determined the elastic properties and vibrational modes of elongated PS spheres (spheroids) ⁷⁸ in the class of anisotropic colloidal crystals.

1.3.4 Temperature-dependence of vibrational modes

Recently, temperature-dependent BLS emerged as a powerful tool for the observation of glassy dynamics in polymer materials under three-dimensional confinement. The eigenmodes revealed the glass transition temperature and gave strong evidence for the existence of a mobile surface layer ⁴⁴. Dry colloidal crystals made of polystyrene nanoparticles of different sizes were measured at various temperatures, starting from room temperature to above the point of glass transition. The trend in the vibration modes lead to the first observation of softening temperature - the point at which the temperature-dependent fundamental vibrational frequency f_{12} reverses the slope just below the glass transition. Interestingly, the glass transition temperature is identified by the point where the vibrational modes disappear. The f_{12} is dependent on the spherical symmetry and elastic parameters of the particles. Beyond this, another mode of vibration given by interaction-induced mode f_{11} was identified, which expresses the interparticle interactions in a crystal and is dependent on the thermal properties of particles.

A trend in BLS spectra of $d=141$ nm sized PS particles is shown in Figure 1.9, where the fundamental vibrational modes distinctly show the peak broadening and split with increased temperature. This behavior was attributed to the interaction between the particles. As shown in the spectrum obtained at $T = 296$ K, f_{12} was fitted with a double Lorentzian function and identified as $2f_1 - f_2$ as the exact frequency value. The interaction-induced mode is well represented by $If^2(f)$, which also represents the frequency shifts, broadening of the peak, and split. It is more relevant from Figure 1.9c, where the frequency decreases with temperature, and at a certain point, it starts increasing, identified as the softening temperature. The normalization process for various

particles is done by plotting fd vs. T . Thus, this method can be an interesting approach to identify the glass transition as well as the elastic modulus of nanoparticles.

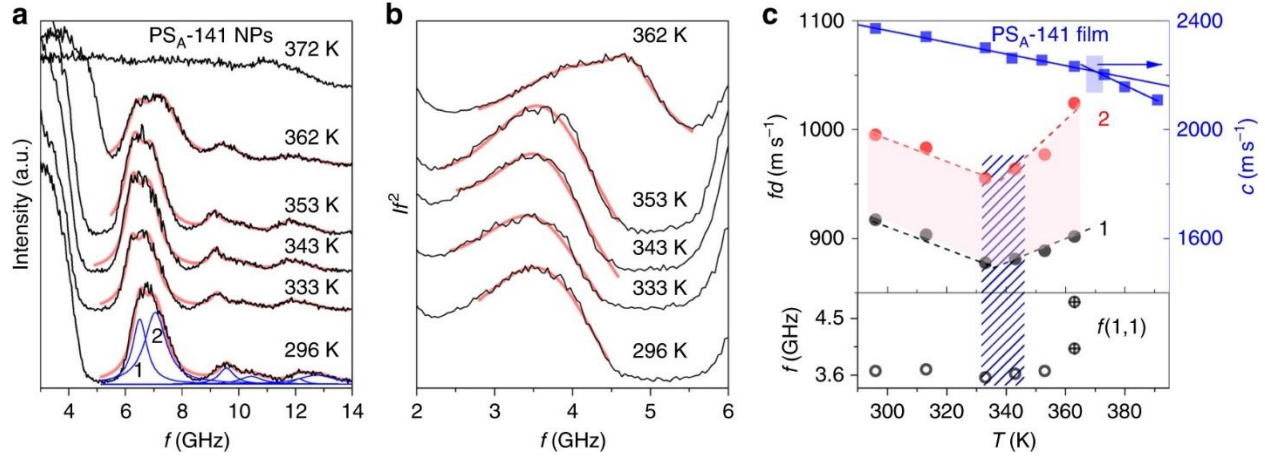


Figure 1.9: (a) BLS spectra of PS NPs of diameter $d=141$ nm measured at various temperatures (b) Normalized power spectra representing interaction induced mode of vibrations in particles (c) Temperature dependence of f_{11} (black open circle) of dipolar mode and f_1, f_2 (black and red solid circles) of quadrupolar mode f_{12} . The blue solid squares stand for the longitudinal sound velocity (v_1) for the PS-141 film annealed at 393 K. The blue shaded line region show the softening temperature (T_s), and the point at which the eigenmodes vanish corresponds to the glass transition temperature (T_g). Adapted with permissions from ref. ⁴⁴.

BLS was also used to explore the shape persistence of the particle core within a core-shell colloidal sphere ¹³⁵. A silica shell of some tens of nm surrounding a polymer core protects the core from changing its shape at a temperature above the glass transition. This was verified by a temperature-dependent eigenmode measurement in BLS. The SiO_2 shell acted as a nano armor for PS polymer core above the glass transition, and the mechanical rigidity of the core is improved compared to bare particles. Thus, BLS can provide the single sphere mechanical properties in a colloidal crystal.

The eigenmode spectra of the temperature-dependent BLS measurements of core-shell structures are shown in Figure 1.10. The quadrupolar mode frequency f_{12} was highly intense, which was quite similar to the bare PS particles spectra. This was visible even after the melting above its T_g and cooling down to room temperature. This proved the shape persistence of the core particle within the shell, which is accompanied by the enhancement of rigidity above its T_g .

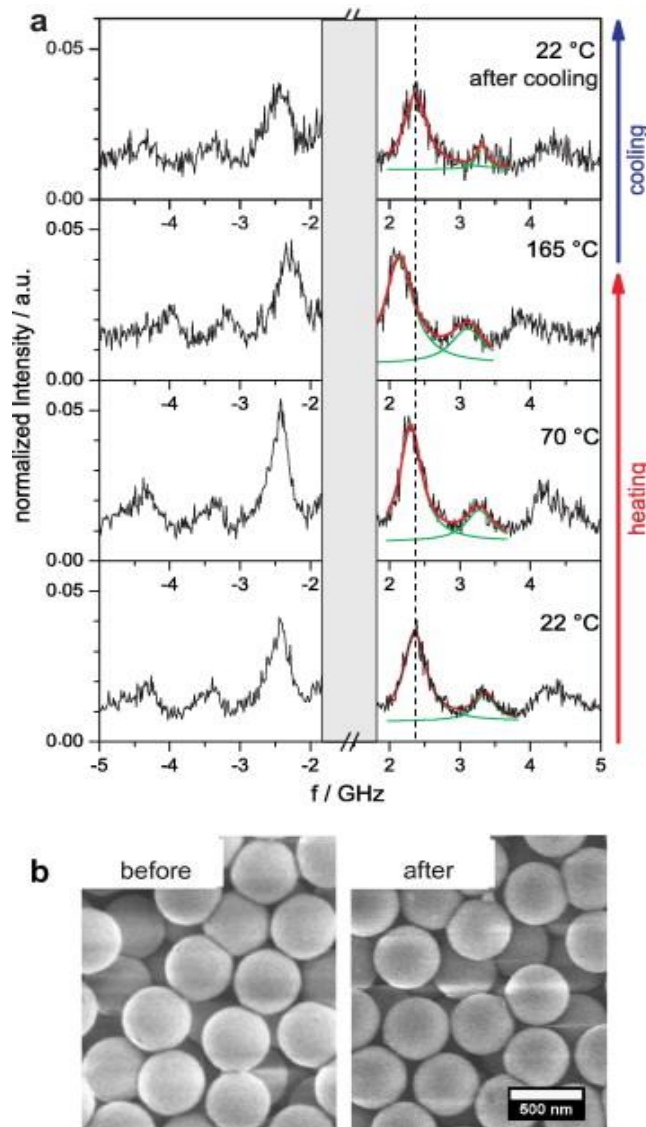


Figure 1.10: (a) Eigenmode spectra of PS-SiO₂ core-shell spheres before and after heating above the glass transition temperature. (b) SEM images of the CCs before and after heating and cooling to room temperature. Adapted with permissions from ref. ¹³⁵.

1.3.5 Mechanical reinforcement of PS CCs by supercritical fluids

Technological applications and processes based on polymer CCs demand the optimization of its properties like glass transition temperature (T_g) and elastic moduli. It has been reported that, at the nanoscale, the glass transition temperature of the polymer changes when compared to the bulk ⁴⁴. This phenomenon depends on the interfacial effects, which are influenced by environmental change. In other words, the increase in particle interactions and contact area influences the modulation of T_g ^{136–138}. Significantly, the existence of a mobile surface layer on polymer thin

films occurring at the so-called softening temperature (T_s), plays a major role in deviating T_g with nanoconfinement^{44,139–141}. As previously reported, several gases, including nitrogen, carbon dioxide, and hydrofluorocarbons, can change the T_g of bulk polymers by exposing polymers to their supercritical form at high pressure^{142,143}. An illustration of the supercritical phase of Ar gas above the critical point of temperature and pressure is shown in Figure 1.11¹⁴⁴. Note that, above 150 K and 48.7 bar, Ar gas is in its supercritical phase.

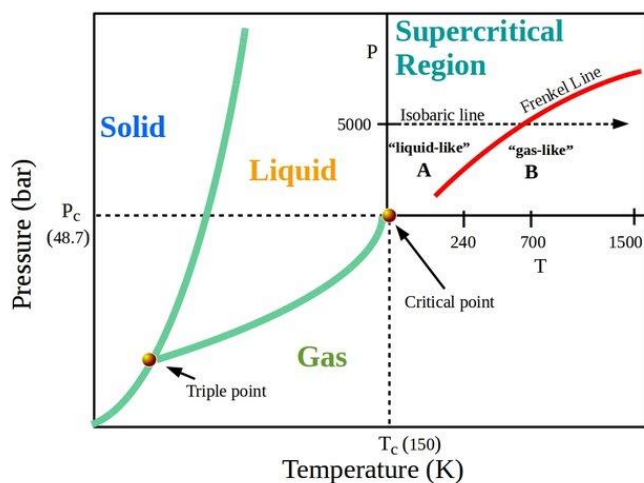


Figure 1.11: Phase diagram (pressure-temperature) of Ar gas. The region above the critical point, above its critical temperature and critical pressure (48.7 bar, 150 K), is considered as the supercritical fluid phase. Adapted with permissions from ref.¹⁴⁴.

Employing Brillouin light scattering (BLS), the influence of supercritical Ar and N_2 at high pressure on the T_s and T_g of PS NPs (diameter, $d = 268$ nm) in the self-assembled CC is investigated¹. In Figure 1.12, the frequencies of vibrational modes (1,1) and (1,2) of the NPs are shown as a function of temperature at specific gas pressure conditions. The temperature is increased from 300 K (room temperature, RT) at a rate of 0.25 K min^{-1} to a higher temperature greater than the T_g of bulk PS (373 K). The observed turnover in the slope of $f_{1,1}$ and $f_{1,2}$, represents the softening temperature, T_s . As previously mentioned, the formation of the mobile surface layer starts at this temperature. Above this temperature, PS NPs experience stronger physical interaction⁴⁴, which is shown by the steep increase of $f_{1,1}$ and $f_{1,2}$. The T_g of PS NPs is identified as the point where the vibrational modes disappear in the BLS spectra, because after attaining T_g , PS NPs lose their spherical shape and form a continuous PS film.

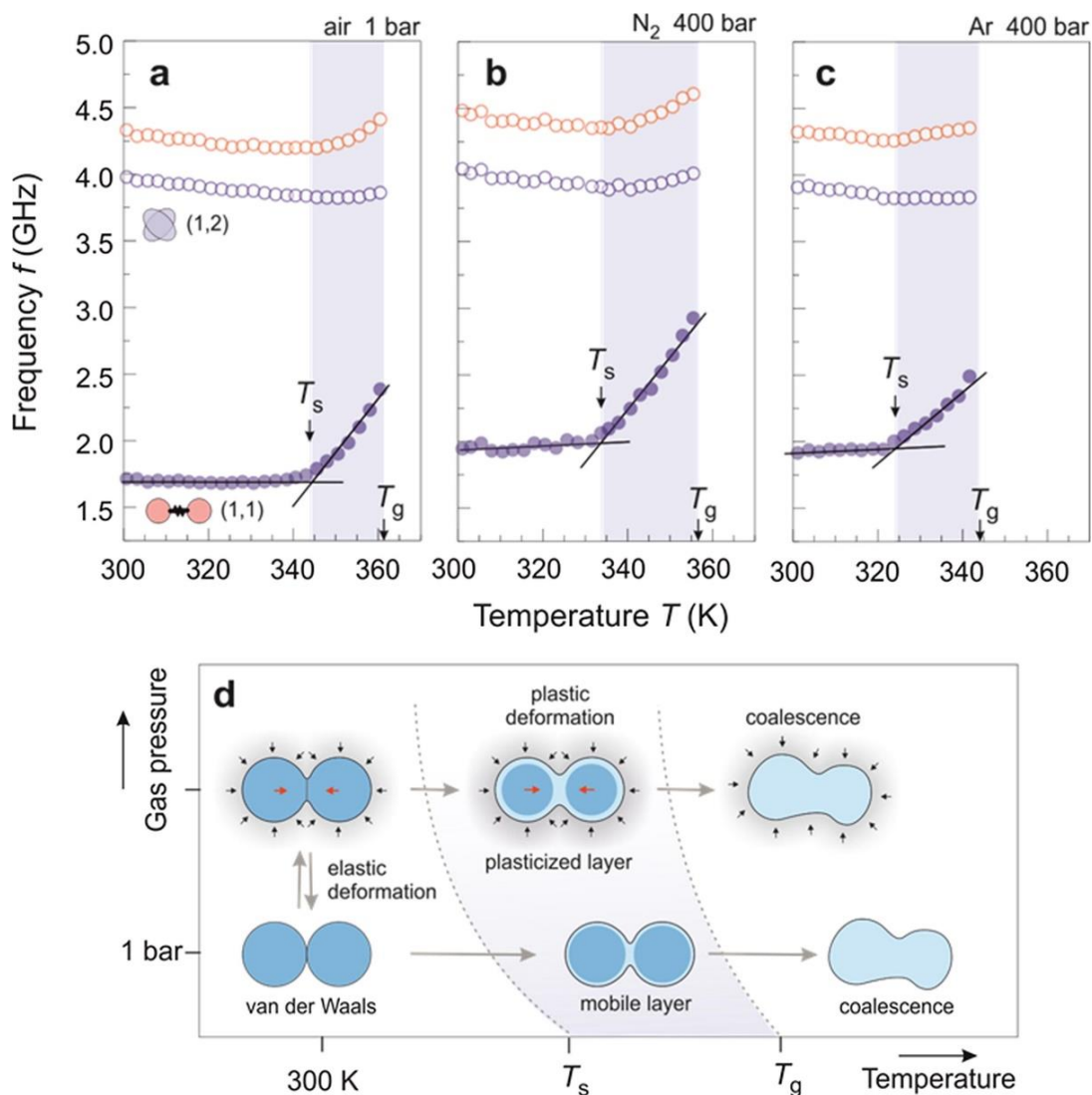


Figure 1.12: The temperature dependence of the frequency of vibrational modes of PS CCs of diameter 268 nm at (a) 1 bar air (b) 400 bar N_2 gas and (c) 400 bar Ar gas. The turnover in the trend of frequencies gives the softening temperature (T_s) and the point above which the mode disappears gives the glass transition temperature (T_g). (d) Schematic illustration of the response of PS CCs when exposed to temperature-assisted gas pressure treatments. Adapted with permissions from ref. ¹.

From Figure 1.12a, at ambient room conditions (1 bar air), the observed $T_s = 344 \pm 3$ K and $T_g = 367 \pm 3$ K. However, the exposure to 400 bar of N_2 gas decreases these values to, $T_s = 335 \pm 3$ K and $T_g = 360 \pm 3$ K, as shown in Figure 1.12b. Similarly, the exposure to 400 bar Ar gas (Figure 1.11c) results in a bigger drop of T_s to $T_s = 322 \pm 3$ K and of T_g to $T_g = 351 \pm 3$ K. At first glance, one can expect that T_g should increase with pressure due to the decrease of polymer-free surface with plasticization. Also, as reported in the literature, the T_g of bulk PS increases by about

13 K after exposure to 400 bar hydrostatic pressure¹⁴⁵. Therefore, the reduction of T_g with the gas pressure can be assigned to a gas-specific behavior, because supercritical fluids can behave as solvents for polymers and can result in their plasticization. Plasticization of PS NPs results from the gas diffusion, which is more pronounced in Ar than in N_2 gas. In general, the gas diffusion can increase the free volume in polymers and can modulate the thermo-mechanical properties^{146–148}.

The schematic representation of the response of PS CCs exposed to specific (p, T) conditions is given in Figure 1.12d. At ambient room conditions (1 bar air), NPs are weakly bonded by van der Waals interactions. Typically, the increase in temperature above T_s , results in the formation of a mobile surface layer as represented by a core-shell-like structure. Further increase in temperature above T_g , results in the coalescence of NPs forming a continuous bulk film. With the application of hydrostatic gas pressure, this process can be fastened.

At ambient room temperature and applied high pressure, the NPs are elastically deformed due to hydrostatic compression, increasing the particle contact area. However, in these conditions, this effect is completely reversible. When the temperature rises at high applied pressure, the gas diffusion inside the PS NPs also increase, resulting in the plasticized surface layer. Note that the core-shell nature of NPs is more pronounced, and the T_s is lower compared to the ambient pressure condition. The synergistic combination of plasticization of PS NPs by gas pressurization and hydrostatic compression results in the permanent soldering of NPs. However, the shape and periodic arrangement of NPs are maintained in this soldering phase. Therefore, the region in between T_s and T_g (grey shaded region in Figure 1.12c) can be identified as the soldering phase of the PS NPs. The region below the T_s is the glassy phase and above the T_g is the rubbery phase¹. Note that in the soldering phase, T_g of the outer shell is modified with gas pressurization, while the core remains in the glassy state.

Figures 1.13a, b represent the preferential (p, T) conditions for the soldering of PS NPs using supercritical N_2 and Ar, respectively. As described in the previous section, T_s and T_g of PS CCs are modified with different temperature-assisted-pressure treatments. For both gases, we can identify three regions: below the T_s , PS CCs are in the glassy state; in between T_s and T_g , PS CCs are in the soldering phase, and above T_g , in the rubbery state. The dashed lines in Figure 1.13a and b represent the calculated T_g of PS solely due to the hydrostatic compression, excluding the effect of plasticization¹⁴⁵. For both the gases, T_s and T_g decreases down to a certain cross-over pressure.

The diffusion of gases inside the polymer increases with the applied pressure and hence also the plasticization efficiency. However, above the crossover pressure, hydrostatic compression dominates over plasticization. In the phase diagram for N₂ gas (Figure 1.13a), the crossover pressure is at about 700 bar, for which T_s and T_g are identified to be 320 ± 3 K and 356 ± 3 K, respectively. In the case of Ar gas (Figure 1.13b) used as the plasticizer, the crossover occurs at a higher pressure of about 850 bar. The corresponding T_s and T_g are identified to be 303 ± 3 K and 337 ± 3 K, respectively. The above result confirms that the soldering of PS CCs using supercritical Ar is more efficient than N₂, because it can be performed at lower temperatures (close to RT) and still at reasonable pressure (850 bar).

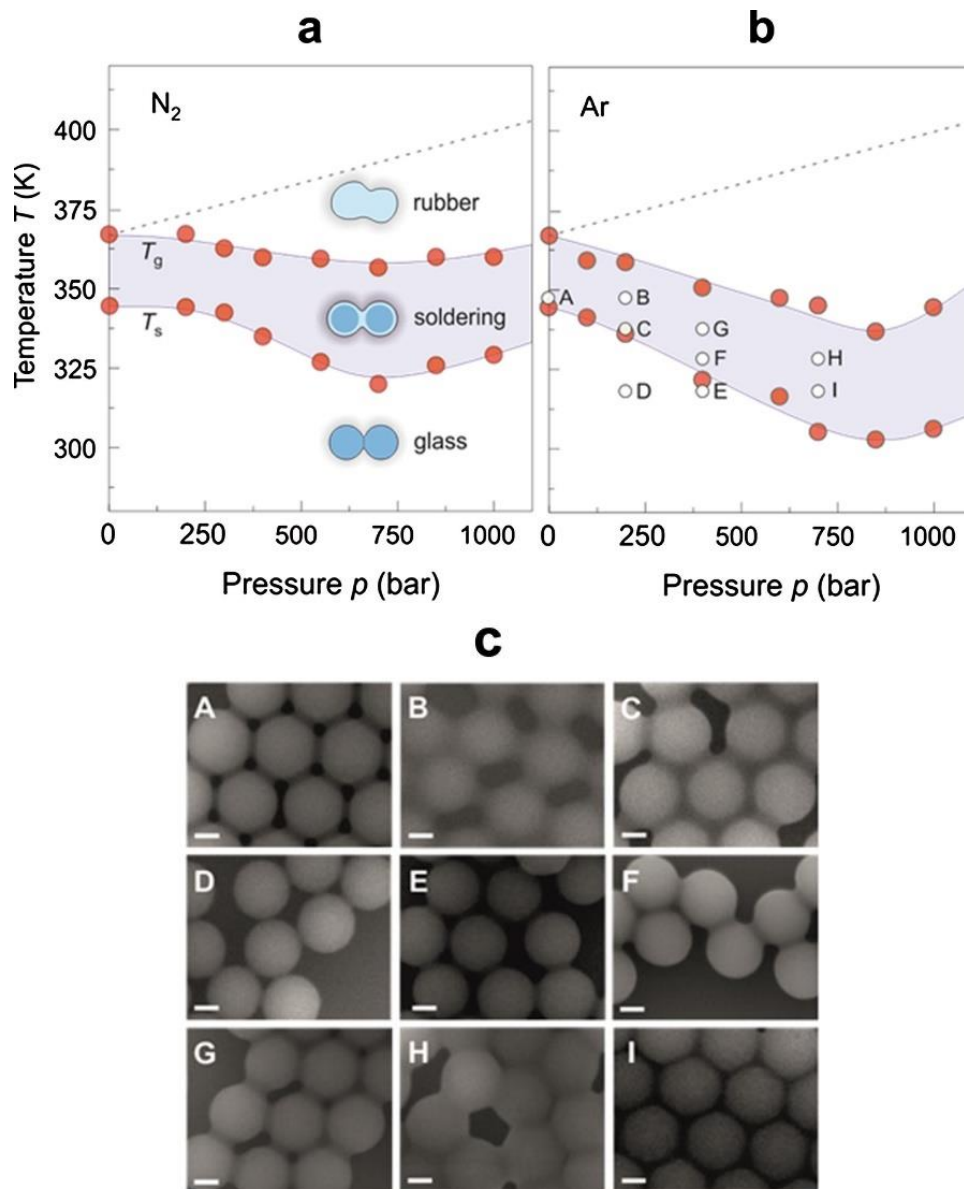


Figure 1.13: Pressure-temperature phase diagram showing the preferential (p, T) conditions of soldering (grey shaded region) for (a) N₂ and (b) Ar gas pressurization in PS CCs of diameter 268 nm. (c) SEM images of PS CCs represented after the Ar pressure treatments corresponding to the (p, T) conditions marked in (b). Adapted with permissions from ref. ¹.

Figure 1.13c shows the SEM images of PS CCs after the temperature-assisted gas pressure treatments at specific (p, T) conditions, as given in Figure 1.13b. Notably, the samples treated at conditions corresponding to the glassy state of PS CCs (labeled as D and E) appear similar to the pristine sample (labeled as A). Contrarily, the samples treated at (p, T) conditions favorable for soldering (labeled as B, C, G, F, H, I) exhibit enhanced NP-NP contacts. From the example of temperature treatment at 1 bar, soldering is also possible at a higher temperature. However, more efficient soldering occurs when gas plasticization is included. It is to be noted that above 700 bar (samples H and I), the NPs deform to a hexagonal shape.

1.4 Thesis Outline

This thesis is divided into seven chapters. Chapter 1 is an introduction to the basics of colloidal assembly, the theory of elasticity, and a literature review on the vibrational analysis of colloidal crystals. Chapter 2 discusses the basics of Brillouin light scattering theory and instrumentation. Chapters 3 to 7 give a discussion of experimental results. Chapter 3 addresses the synthesis and characterization of polystyrene CCs. Chapter 4 illustrates the evaluation of the elastic properties of supercritical gases at high pressure. Chapter 5 discusses the PS CCs exposed to supercritical He gas. Chapters 6 and 7 report the analysis of PS CCs exposed to supercritical Ar and N₂, respectively. Finally, a conclusion and outlook are provided.

The concepts discussed in Chapters 3 – 7 are the elaborated version of the following publication:

Jeena Varghese, Reza Mohammadi, Mikolaj Pochylski, Visnja Babacic, Jacek Gapinski, Nicolas Vogel, Hans-Juergen Butt, George Fytas, Bartlomiej Graczykowski, Size-dependent nanoscale soldering of polystyrene colloidal crystals by supercritical fluids, *Journal of Colloid and Interface Science* 633 (2023) 314–322. <https://doi.org/10.1016/j.jcis.2022.11.090>

Chapter 2

Brillouin Light Scattering

For an elastic medium having spatial periodicities in the sub-micrometer range, the acoustic waves propagate in the hypersonic frequency regime. Conventional ultrasonic transducer-based methods are not feasible in the measurement of such high-frequency elastic waves. In this regard, Brillouin spectroscopy has achieved a prominent place in the investigation of photon-phonon interactions in nanoscale systems^{5,43,79,149}. Brillouin Light Scattering (BLS), as a powerful nondestructive and contactless optical tool, allows the investigation of acoustic phonons in the GHz regime. Here, we discuss the spontaneous type scattering in which the incident photons are inelastically scattered by the thermally populated acoustic phonons. Let us consider the theory of light scattering and the experimental setup in this section.

2.1 Theory of light scattering

Since this thesis deals with the Brillouin light scattering in condensed matter, we consider the classical description of light and the scattering medium. The optical property of an isotropic medium can be described in terms of dielectric constant ϵ . However, the real media will have random fluctuations in the local dielectric constant due to the thermal motion of molecules in the medium. Taking into account the possible anisotropy introduced in the media due to the fluctuations, a general description of the local dielectric constant can be given as:

$$\boldsymbol{\epsilon}(\mathbf{r}, t) = \epsilon \mathbf{I} + \delta\boldsymbol{\epsilon}(\mathbf{r}, t) \quad (2.1)$$

where $\delta\boldsymbol{\epsilon}(\mathbf{r}, t)$ is the dielectric fluctuation tensor at the position \mathbf{r} and time t , ϵ is an average dielectric constant (refractive index $n_r = \sqrt{\epsilon}$), and \mathbf{I} is the second-rank unit tensor.

Considering the scattering of a plane wave with electric field amplitude E_0 , angular frequency ω_i , and the incident wave vector \mathbf{k}_i , the incident electric field can be given^{22,150} as:

$$\mathbf{E}_i(\mathbf{r}, t) = \mathbf{e}_i E_0 \exp i(\mathbf{k}_i \cdot \mathbf{r} - \omega_i t), \quad (2.2)$$

where \mathbf{e}_i is the unit vector in the direction of the incident electric field.

At a large distance M from the scattering volume, the scattered electric field $E_s(M, t)$ should be considered as $E = E_i + E_s$, satisfying the Maxwell equation throughout the space. As given in the literature ¹⁵⁰, the component of the scattered electric field at a distance M from the scattering volume V with polarization \mathbf{e}_s is,

$$E_s(M, t) = \frac{E_0}{4\pi R\epsilon} \exp i k_s M \int_V d^3 r \exp i(\mathbf{q} \cdot \mathbf{r} - \omega_i t) [\mathbf{e}_s \cdot [\mathbf{k}_s \times (\mathbf{k}_s \times (\delta\epsilon(\mathbf{r}, t) \cdot \mathbf{e}_i))]], \quad (2.3)$$

where \mathbf{k}_s denote the propagation vector. The scattering wave vector \mathbf{q} can be defined as the difference between the incident and scattered propagation vectors given by,

$$\mathbf{q} = \mathbf{k}_i - \mathbf{k}_s. \quad (2.4)$$

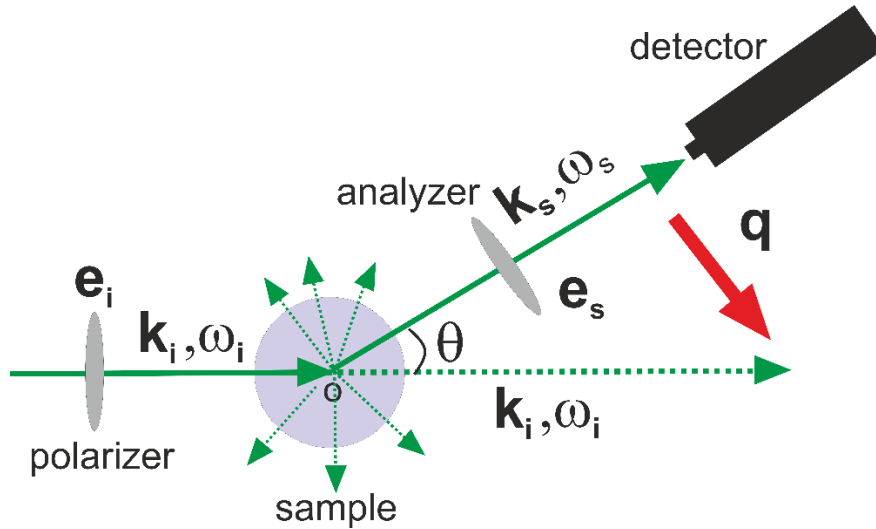


Figure 2.1: Illustration of light scattering experiment showing the incident light with polarization \mathbf{e}_i , wave vector \mathbf{k}_i and frequency ω_i . This light is being scattered in all directions by the acoustic waves in the sample. The scattered light with polarization \mathbf{e}_s , wave vector \mathbf{k}_s and frequency ω_s reaching the detector is shown. The red arrow shows the scattering wave vector \mathbf{q} as $\mathbf{k}_i - \mathbf{k}_s$. Reproduced from ref. ^{22,150}.

As given in Figure 2.1, the angle between \mathbf{k}_i and \mathbf{k}_s gives the scattering angle θ . The magnitude of wave vectors \mathbf{k}_i and \mathbf{k}_s are $2\pi n/\lambda_i$ and $2\pi n/\lambda_s$, respectively, where λ_i and λ_s denote the wavelengths corresponding to the incident and scattered light. In most light scattering experiments, the scattering is quasi-elastic and therefore $|\mathbf{k}_i| \cong |\mathbf{k}_s| = 2\pi n/\lambda$. From Figure 2.1, the magnitude of \mathbf{q} is given by,

$$q^2 = |\mathbf{k}_i - \mathbf{k}_s|^2 = k_i^2 + k_s^2 - 2\mathbf{k}_i \cdot \mathbf{k}_s = 2k_i^2 - 2k_i^2 \cos\theta \quad (2.5)$$

$$q^2 = 2k_i^2(1 - \cos\theta) = 4k_i^2 \sin^2 \frac{\theta}{2},$$

$$q = 2k_i \sin \frac{\theta}{2} = \frac{4\pi n}{\lambda_i} \sin \frac{\theta}{2}. \quad (2.6)$$

Eq. (2.6) is the Bragg condition.

In Eq. 2.3, the integration takes place over the whole space within the scattering volume V , and therefore, it influences only the variables with the space coordinate \mathbf{r} . Using the spatial Fourier transform of the dielectric fluctuation tensor: $\delta\epsilon(\mathbf{q}, t) = \int_V d^3r \exp i\mathbf{q} \cdot \mathbf{r} \delta\epsilon(\mathbf{r}, t)$, Eq. 2.3 can be rewritten as ¹⁵⁰:

$$E_s(R, t) = \frac{E_0}{4\pi R \epsilon} \exp i(k_s R - \omega_i t) [\mathbf{e}_s \cdot [\mathbf{k}_s \times (\mathbf{k}_s \times (\delta\epsilon(\mathbf{q}, t) \cdot \mathbf{e}_i))]], \quad (2.7)$$

, where $\frac{E_0}{4\pi R \epsilon} \exp i(k_s R - \omega_i t)$ denotes the spherical wave originating from the origin of the scattering volume, represented as point O in Figure 2.1.

Simplifying the vector product, Eq. 2.7 reduces to:

$$E_s(R, t) = \frac{-k_s^2 E_0}{4\pi R \epsilon} \exp i(k_s R - \omega_i t) \delta\epsilon_{is}(\mathbf{q}, t), \quad (2.8)$$

where $\delta\epsilon_{is}(\mathbf{q}, t) = \mathbf{e}_s \cdot \delta\epsilon(\mathbf{q}, t) \cdot \mathbf{e}_i$ is the component of the dielectric fluctuation tensor along the initial and final polarization directions. The time-correlation function of E_s can be written as ¹⁵⁰:

$$\langle E_s^*(R, 0) E_s(R, t) \rangle = \frac{k_s^4 |E_0|^2}{16\pi^2 R^2 \epsilon^2} \langle \delta\epsilon_{is}(\mathbf{q}, 0) \delta\epsilon_{is}(\mathbf{q}, t) \rangle \exp(-i\omega_i t). \quad (2.9)$$

And the spectral density is:

$$I_E(\omega) = \frac{1}{2\pi} \int_{-\infty}^{\infty} d\tau \langle E^*(t) E(t + \tau) \rangle \exp(-i\omega\tau), \quad (2.10)$$

where τ is the relaxation time. Substituting Eq. (2.9) into Eq. (2.10), we can obtain the spectral density of light scattered into the detector (intensity measured by the detector) with \mathbf{e}_s , \mathbf{k}_s and ω_s , given by:

$$I_{is}(q, \omega, R) = \frac{I_0 k_s^4}{16\pi^2 R^2 \varepsilon^2} \frac{1}{2\pi} \int_{-\infty}^{\infty} dt \langle \delta\varepsilon_{is}(\mathbf{q}, 0) \delta\varepsilon_{is}(\mathbf{q}, t) \rangle (\exp i(\omega_s - \omega_i)t), \quad (2.11)$$

where $I_0 \equiv |E_0|^2$. From the Eq. 2.11, the spectral density depends on the angular frequency change of the incident and scattered light in the scattering process as $\omega \equiv \omega_i - \omega_s$. Furthermore, $I_{is} \propto k_s^4 \propto \lambda^{-4}$, shows that the scattering intensity is inversely proportional to the fourth power of the light wavelength. In other words, the electromagnetic radiations of shorter wavelengths will be scattered more than the longer wavelength radiations, apparently the scientific explanation of the blue color of the sky. $I_{is} \propto R^{-2}$ expresses the attenuation of the spherical wave ²².

2.2 Brillouin Light Scattering

Brillouin light scattering refers to the inelastic scattering of monochromatic light by the acoustic waves in the medium. The first theoretical prediction of the scattering of a coherent light beam by the thermal phonons in a homogeneous medium was proposed by French physicist Léon Brillouin in 1922 ¹⁵¹. One of the distinct features of a BLS spectrum is the appearance of a frequency doublet, now termed as Brillouin doublet. In 1926, Leonid Mandelstam published his independent ideas on spontaneous scattering, later called “Brillouin-Mandelstam scattering” ¹⁵². As mentioned, the thermal motion of atoms and molecules in a medium induces position and time-dependent density fluctuations, propagating as periodic waves. These acoustic waves propagating through the medium generate variation in the local dielectric constant (refractive index) of the material, which can act as a diffraction grating for the incident monochromatic light ¹⁵³.

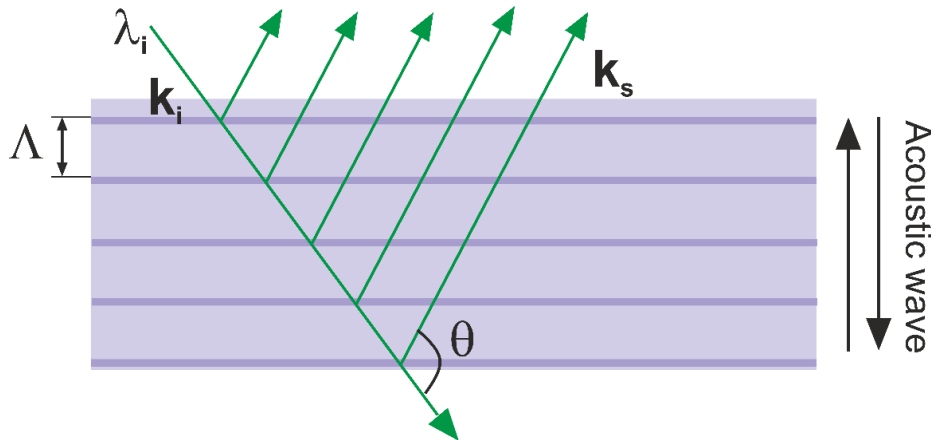


Figure 2.2: Brillouin light scattering as a process of constructive interference of the multiple reflections of the incident light beam (λ_i, \mathbf{k}_i) from the acoustic wave of wavelength Λ .

The simplest description of BLS is the constructive interference between multiple reflections of incident light beams by the propagating acoustic waves, as shown in Figure 2.2. Let the wavelength of acoustic waves be Λ . Then, the medium can be treated as a stack of periodic multilayers having periodicity Λ . According to Bragg's law, the condition for maximum reflected intensity is:

$$\lambda_i = 2n\Lambda \sin \frac{\theta}{2}, \quad (2.12)$$

Where n is the refractive index of the medium, λ_i is the wavelength of incident light and θ stands for the angle between incident and scattered light. Substituting Eq. 2.12 in Eq. 2.6 we obtain:

$$\mathbf{q} = \frac{4\pi n}{\lambda_i} \sin \frac{\theta}{2} = \frac{2\pi}{\Lambda} \quad (2.13)$$

Eq. 2.13 indicates that the magnitude of the scattering wave vector \mathbf{q} is equivalent to the phonon wave vector ($\mathbf{k} = \frac{2\pi}{\Lambda}$). By changing the scattering angle θ , \mathbf{q} vector can be varied and BLS can probe different acoustic waves. The identity $\mathbf{q} = \mathbf{k}$ reflects the momentum conservation in the scattering process, by the momentum transfer between sound waves and photons. Considering an acoustic wave having a phase velocity v , the scattered light of initial frequency f_i experiences a Doppler shift f determined by the scattering geometry, reaching the final frequency of: ¹⁵⁴,

$$f_s = f_i \pm f = f_i \pm 2f_i \frac{v}{v_m} \sin \frac{\theta}{2} = f_i \pm \frac{v}{2\pi} \frac{4\pi n}{\lambda_i} \sin \frac{\theta}{2}, \quad (2.14)$$

where v_m is the velocity of light in the medium. The plus and minus signs stand for the opposite propagation directions of the sound waves. The positive sign corresponds to the sound wave traveling towards the detector, increasing the frequency of the scattered light, termed “anti-stokes scattering (phonon annihilation)”. The negative sign corresponds to the acoustic wave traveling away from the detector, “Stokes scattering (phonon creation)”. Correspondingly, the Brillouin doublet is centered at frequencies:

$$f = \pm \frac{v}{2\pi} q, \quad (2.15)$$

or in terms of angular frequency:

$$\omega = \omega_s - \omega_i = \pm vq. \quad (2.16)$$

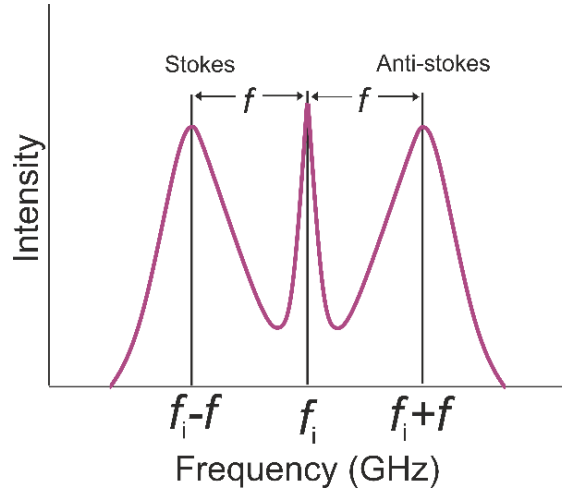


Figure 2.3: Schematic representation of a BLS spectrum showing Stokes and Anti-Stokes scattering frequencies.

Regardless of the scattering geometries, all the scattering process is governed by conservation laws. From a quantum mechanical point of view, we can consider BLS as an inelastic photon-phonon collision, where photon and phonon are the quanta of electromagnetic and acoustic fields, respectively. Consider an incident photon having energy $\hbar\omega_i$ and momentum $\hbar\mathbf{k}_i$, which is inelastically scattered by a phonon of energy $\hbar\omega$ and momentum $\hbar\mathbf{q}$ in the scattering medium. In this process, a phonon is either created (Stokes scattering) with the scattered photon losing its energy or annihilated (anti-stokes scattering) with the scattered photon gaining the corresponding energy, as illustrated in Figure 2.4. The energy and momentum conservation laws¹⁵⁵ can be given as:

$$\hbar\omega_s = \hbar\omega_i \pm \hbar\omega \quad (2.17)$$

$$\hbar\mathbf{k}_s = \hbar\mathbf{k}_i \pm \hbar\mathbf{q} \quad (2.18)$$

, where

$$\text{Stokes scattering:} \quad \begin{aligned} \omega_s &= \omega_i - \omega \\ \mathbf{k}_s &= \mathbf{k}_i - \mathbf{q} \end{aligned} \quad (2.19)$$

$$\text{Anti-Stokes scattering:} \quad \begin{aligned} \omega_s &= \omega_i + \omega \\ \mathbf{k}_s &= \mathbf{k}_i + \mathbf{q} \end{aligned} \quad (2.20)$$

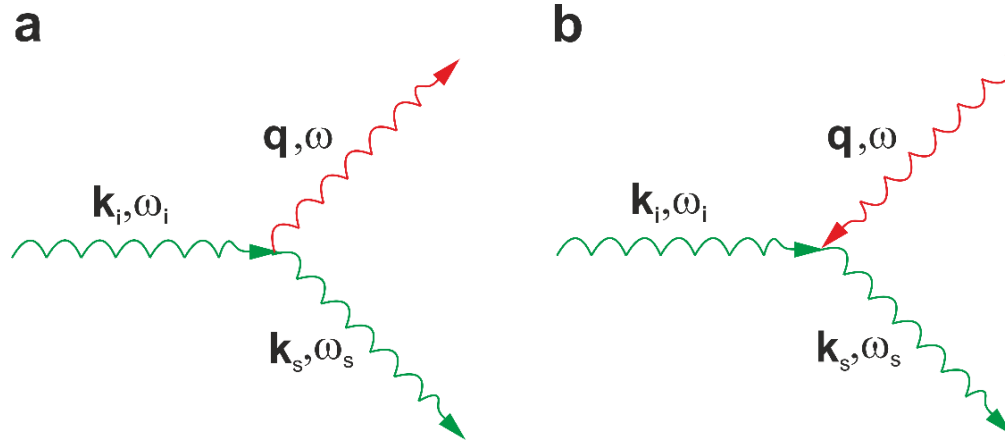


Figure 2.4: Schematic illustration of (a) Stokes scattering (phonon creation) and (b) anti-Stokes scattering (phonon annihilation).

A phonon is the acoustic analog of a photon, i.e., the quantum of the acoustic field. In this thesis, we refer to hypersonic phonons (GHz frequency) propagating in 3D colloidal crystals. For the purpose of this thesis, terms like sound waves, elastic waves, acoustic waves, elastic excitations, and phonons will be used interchangeably.

2.3 BLS instrumentation

The frequency shift determined by BLS comes in the range of 10^8 to 10^{11} GHz, which is much smaller when compared to the incident laser frequency $\sim 10^{14}$ GHz. In this case, a diffraction grating as used in Raman spectroscopy, will not be enough to resolve the vibrational modes¹⁵⁶ of CCs. Therefore, to achieve a higher spectral resolution, spectrometers based on the *Fabry–Pérot interferometer (FPI)* are used^{157–159}. A combination of a highly monochromatic laser source and two FPIs with multiple light passes can provide excellent BLS spectra.

2.3.1 Tandem Fabry-Perot interferometer

The *FPI*, a *multiple-beam interferometer*, was constructed by the physicists Charles Fabry and Alfred Perot in 1897¹⁵⁸. The most straightforward configuration of an FPI is made of two plane mirrors parallel to each other, separated at a distance L . The distance between the mirrors (typically in the air) can be varied by moving one of these mirrors while the other remains fixed. The laser light entering through the first mirror undergoes multiple reflections between the two mirrors. The reflected beams interfere, and the beams that are transmitted should satisfy the condition of constructive interference given as:

$$m\lambda_i = 2n_{FP}L\cos\theta, \quad (2.21)$$

where m is an integer, n_{FP} is the refractive index of the medium inside the FP, $\lambda_i = \frac{2\pi}{k_0}$ is the wavelength of light in vacuum, and θ is the angle between the normal to the mirrors and the light beam. For the nearly normal incidence of light to the mirror, ($\cos\theta = \cos 0 = 1$). Typically, the medium inside the FP is air, and therefore $n_{FP} = 1$. Thus, Eq. (2.21) can be thus reduced to:

$$\lambda_i = \frac{2L}{m}. \quad (2.22)$$

Eq. 2.22 shows that only the light of wavelength $\frac{2L}{m}$ will be transmitted, and the transmitted λ_i can be changed by choosing different mirror distances L . As given in Figure 2.5, the separation of two adjacent transmission maxima for a given L , is called the free spectral range ($FSR = \Delta\lambda$) and is expressed as:

$$\frac{\Delta\lambda}{\lambda_i} = \frac{\Delta m}{m}, \quad (2.23)$$

where $\Delta m = 1$. From Eq. (2.22) and (2.23), FSR ($\Delta\lambda$) can be expressed as:

$$\Delta\lambda = \frac{\lambda_i}{m} = \frac{\lambda_i^2}{2L}, \quad (2.24)$$

or in terms of frequency:

$$\Delta f = \frac{v_0}{2L}, \quad (2.25)$$

where v_0 is the velocity of light in vacuum, $v_0 = 3 \cdot 10^8 \text{ ms}^{-1}$.

FSR is a very important parameter to be set before using FPI in BLS spectroscopy. In this thesis, for working with different-sized PS NPs (frequency of Lamb modes depends on particle diameter d), we need different FSR, which is achieved by adjusting the mirror spacing L .

The full width at half maximum, FWHM ($\delta\lambda$) of the transmitted line (Figure 2.7), depends on the reflectance, \mathcal{R} . The transmission function of the FPI and reflectance is given by Airy function¹⁶⁰

$$T_{FPI} = \frac{(1 - \mathcal{R})^2}{1 + \mathcal{R}^2 - 2\mathcal{R}\cos\delta_p} = \frac{1}{1 + c_F \sin^2(\delta_p/2)}, \quad (2.26)$$

where c_F is called the coefficient of finesse \mathcal{F} , $c_F = 4\mathcal{R}^2/(1 - \mathcal{R}^2)^2$ and the phase difference between each succeeding reflection, $\delta_p = 4\pi L/\lambda_i$. FWHM is given by:

$$\delta\lambda = \frac{4}{\sqrt{c_F}} \frac{\lambda_i}{2\pi m}. \quad (2.27)$$

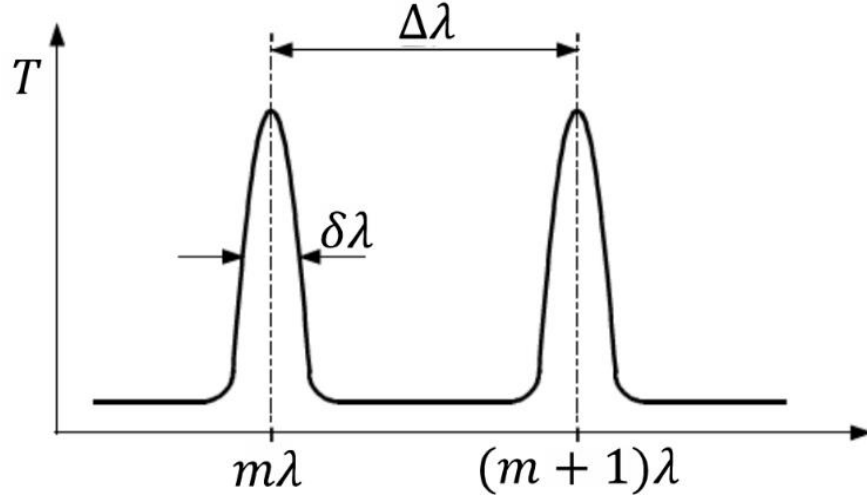


Figure 2.5: Illustration of free spectral range (FSR = $\Delta\lambda$) as the spacing between two adjacent transmission maxima. The full width at half maximum, FWHM ($\delta\lambda$) is also shown. Adapted from ref. ¹⁶¹.

Now, finesse \mathcal{F} is the ratio of FSR to the FWHM of a transmission peak, which defines the relative separation of the adjacent transmission peaks ¹⁶⁰:

$$\mathcal{F} = \frac{\Delta\lambda}{\delta\lambda} = \frac{\lambda_i \sqrt{c_F} 2\pi m}{m 4 \lambda_i} = \frac{\pi\sqrt{c_F}}{2} = \frac{\pi\mathcal{R}}{1 - \mathcal{R}^2}. \quad (2.28)$$

In general, higher finesse is intended for a better resolution of BLS spectra, but practically it cannot be made greater than 100²².

A single FP interferometer has been shown to have too low contrast to allow weak Brillouin signals to be observed due to intense elastically scattered light. This problem was solved by J. R. Sandercock by introducing a multipass FP interferometer ¹⁶². However, a multipass FP interferometer still suffers from the overlapping of neighboring interference orders, leading to unclear interpretations of the measured spectra. Later, Sandercock found a solution for this problem by using a tandem arrangement, i.e., two FP interferometers (FP1 and FP2) in series with slightly different mirror spacing, i.e., FSR ¹⁶². The wavelengths transmitted by the FP1 and FP2 combination must simultaneously satisfy:

$$\begin{aligned}
m_1 \lambda_i &= 2L_1 \quad \text{for FP1} \\
m_2 \lambda_i &= 2L_2 \quad \text{for FP2}
\end{aligned}
\tag{2.29}$$

Due to the slight difference in their FSRs, neighboring order transmission peaks of the two FP interferometers cannot coincide, as illustrated in Figure 2.6 (a). As a result, significant suppression of interference higher-order transmission is achieved. This is because one of the FP interferometers blocks the adjacent interference orders of the other.

For the tandem interferometer, it is necessary to scan FP1 and FP2 synchronously by changing L_1 and L_2 simultaneously. From Eq. (2.29), it is clear that the condition for the synchronized scanning of the two FP interferometers is that the changes ΔL_1 and ΔL_2 satisfy:

$$\frac{\Delta L_1}{\Delta L_2} = \frac{L_1}{L_2}.
\tag{2.30}$$

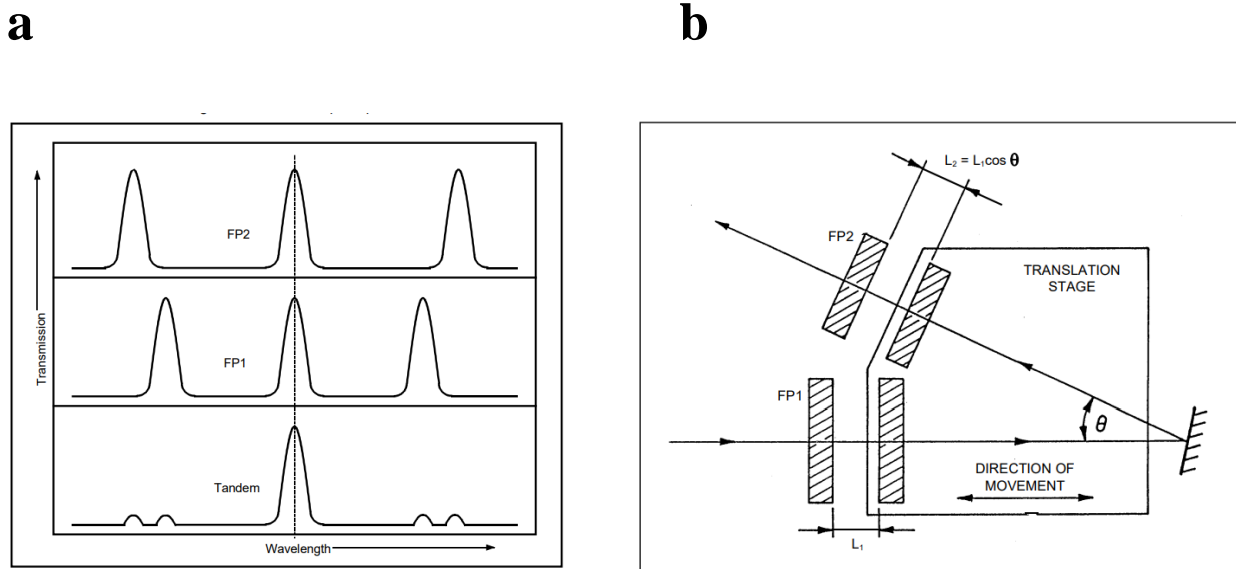


Figure 2.6: (a) Transmission spectra for two single (FP1, FP2) interferometers with different FSR and the TANDEM Fabry-Perot interferometer. (b) Schematic illustration of Sandercock's multipass TANDEM Fabry-Perot interferometer. Adapted from ref. ^{159,162}.

This is achieved by using the scanning stage that J. R. Sandercock has designed ^{159,162}. The principle of the tandem operation is illustrated in Figure 2.6b. The first interferometer FP1 lies in the direction of the translation stage movement (scan direction) such that one mirror sits on this stage while the other sits on a separate angular orientation device. The second interferometer FP2

is positioned such that its axis is at angle θ with respect to the scan direction. The relative spacing of the mirrors is set so that a movement of the translation stage to the left would bring both sets of mirrors into contact simultaneously. A movement of the translation stage to the right sets the spacing to L_1 and $L_2 = L_1 \cos\theta$. Also, the movement of the translation stage ΔL_1 leads to the change of spacing ΔL_1 in FP1 and $\Delta L_2 = \Delta L_1 \cos\theta$ in FP2. Therefore, the condition given in Eq. (2.30) is satisfied.

Besides the tandem FPI, the BLS experimental setup consists of many optical components, including beam splitters, polarizers, lenses, and mirrors. The optical arrangement for the BLS measurements will be described in the subsequent sections.

Chapter 3

Synthesis and characterization of polystyrene colloidal crystals

3.1 Synthesis of polystyrene NPs

Polystyrene (PS) NPs are synthesized by surfactant-free emulsion polymerization¹⁶³ at the Institute of Particle Technology in Erlangen and the Max Planck Institute of Polymer Research in Mainz. Styrene monomer (C_8H_8 , 99 %, Sigma-Aldrich) as the building block of PS CCs is cleaned prior to the polymerization. The commercially available styrene contains 4-tert-butylcatechol ($C_{10}H_{14}O_2$) inhibitor, which hinders the polymerization. As described in the previous literature¹⁶⁴, the styrene mixture is washed using 10% aqueous solution of sodium hydroxide (NaOH, 98 %, Roth) and transferred through an activated aluminum oxide (Al_2O_3 , Roth) column for purification.

For the polymerization reaction, we use a round bottom three-necked flask with a condenser immersed in a silicon oil bath, as shown in Figure 3.1. 240 mL of ultrapure water (18.2 M Ω) is added to the flask, and the water is degassed by passing nitrogen gas under stirring. Simultaneously, the oil bath is heated to 80°C, and the temperature is controlled using a thermometer. After the degassing procedure, the purified styrene monomer is added under stirring. After 10 minutes, ammonium persulfate ($(NH_4)_2S_2O_8$, Sigma-Aldrich) solution in ultrapure water is added as the initiator of the polymerization reaction and stirred at 600 rpm for almost 5 minutes. Later, acrylic acid ($C_3H_4O_2$, Sigma-Aldrich) diluted in 10 mL of ultrapure water is added, and the mixture is allowed to polymerize under stirring for 24 h in an inert atmosphere. The suspension after polymerization is initially filtered using tissue paper, and the large unreacted styrene aggregates are removed. Later, the PS NPs suspension is diluted with ethanol in 1:1 ratio and centrifuged at 10000 rpm for 15 minutes. The supernatant liquid containing the fabrication impurities is removed, and the sedimented NPs are re-dispersed in ultrapure water via sonication. The cleaning procedure is repeated at least twice to obtain PS NPs suspension in water for the fabrication of CCs. Different-sized PS NPs can be achieved by varying the quantity of styrene

monomer, ammonium persulfate, and acrylic acid. The cleaning procedure, especially centrifugation parameters, must be adjusted based on the particle size.



Figure 3.1: Experimental setup for the preparation of PS NPs by surfactant-free emulsion polymerization. This picture was taken by Dr. Reza Mohammadi at prof. Dr. N. Vogel's lab at the Institute of Particle Technology, Erlangen, Germany.

3.2 Fabrication of PS CCs

For BLS measurements, we fabricated 3D PS CC multilayers on glass slides. The glass slides are pre-cleaned by sonication in ethanol and de-ionized water and dried using compressed air. A few microlitres of PS NPs suspension in ultrapure water is drop casted on the glass slide, and the sample is dried in a vacuum bell jar at RT (298 K) for a few hours. A sample image is given in Figure 3.2a. For SEM measurements, we synthesize PS NPs monolayer on an air-water interface³⁰. A low polydispersity of particles is required to fabricate a perfectly close-packed monolayer. The PS NPs suspension in water is mixed with ethanol in 1:1 ratio, which helps in the ordered assembly of particles at the interface due to the Marangoni effect¹⁶⁵.

At first, ultrapure water is taken in a clean glass beaker. The mixture of PS NPs in water and ethanol is taken in a syringe with a needle attached. The syringe tube is connected to a syringe pump, and the end of the needle is allowed to touch the center of the water interface, as shown in Figure 3.2b. After setting the flow speed in the syringe pump, the dispersion mixture is added drop

by drop to the air-water interface. PS NPs get self-assembled at the interface, and finally, a close-packed layer of particles is formed. Care must be taken to avoid the buckling of films due to the excessive addition of particles. A perfectly made monolayer shows structural color ^{3,30}, as visible in Figure 3.2b. The monolayer shown in that figure is prepared using 610 nm particles. The formed monolayer is manually deposited by inserting a pre-cleaned silicon wafer at certain angles in the water and vertically lifting the monolayer from the bottom. The deposited monolayer is initially kept at room condition and then vacuum dried for the SEM measurements.

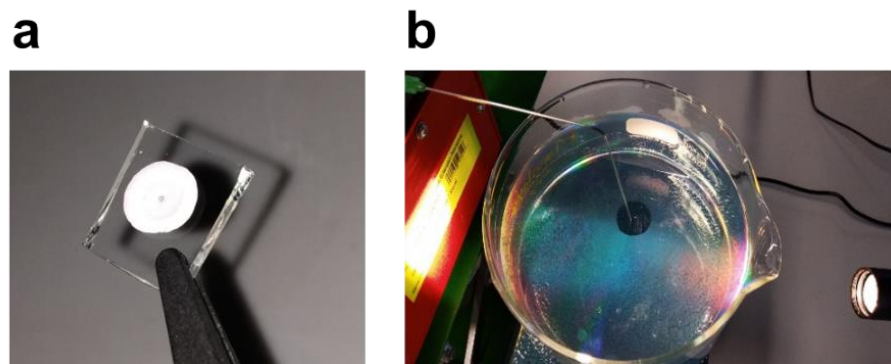


Figure 3.2: (a) PS CCs fabricated by drop casting PS NPs suspension on the glass slide. (b) PS CC monolayer formed on the air-water interface.

3.3 Characterization by in-situ high-pressure BLS and SEM

We use six sets of PS NPs with sizes ranging from 143 nm to 830 nm for the preparation of colloidal crystals. The SEM images of the as-prepared samples are shown in Figure 3.3. Notably, the as-prepared PS CCs have inhomogeneous physical contact bridges formed from fabrication impurities.

Schematic of the in-situ high-pressure BLS experimental setup for measuring PS CCs is given in Figures 3.4a ¹ and b. The original images of the BLS setup taken from the laboratory in the Molecular Biophysics division, Faculty of Physics, UAM, Poznan, are shown in Figures 3.5a-g. The 3D PS CC samples deposited on a clean glass slide (1 cm x 1 cm size) are fixed in a cylindrical sample holder (Figure 3.5d, e) and placed inside the high-pressure chamber (Figure 3.5c). Initially, reference measurements of the as-prepared sample are taken for all PS CCs at ambient room conditions (1 bar air, RT, 296 K). Further, Ar/He/N₂ gas is supplied to the high-pressure chamber through a metal pipe (Figure 3.4a) at the specific pressure condition set by a gas compressor (Figure 3.5b), and BLS measurements are repeated.

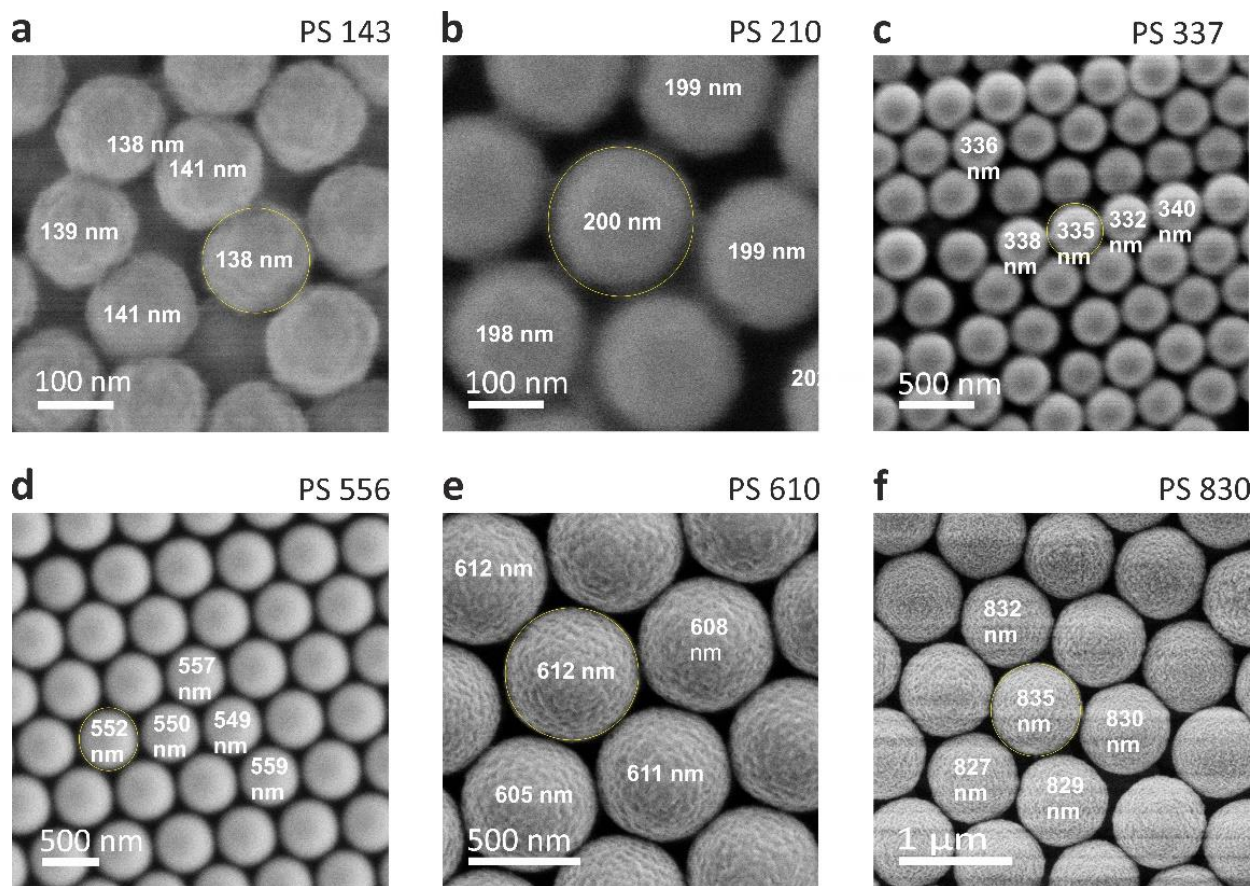


Figure 3.3: SEM images of the pristine PS CCs with particle diameters (a) $d = 143$ nm (b) $d = 210$ nm (c) $d = 337$ nm (d) $d = 556$ nm (e) $d = 610$ nm (f) $d = 830$ nm. The scale bars are shown in the figures. This image is reproduced from ref ¹⁹.

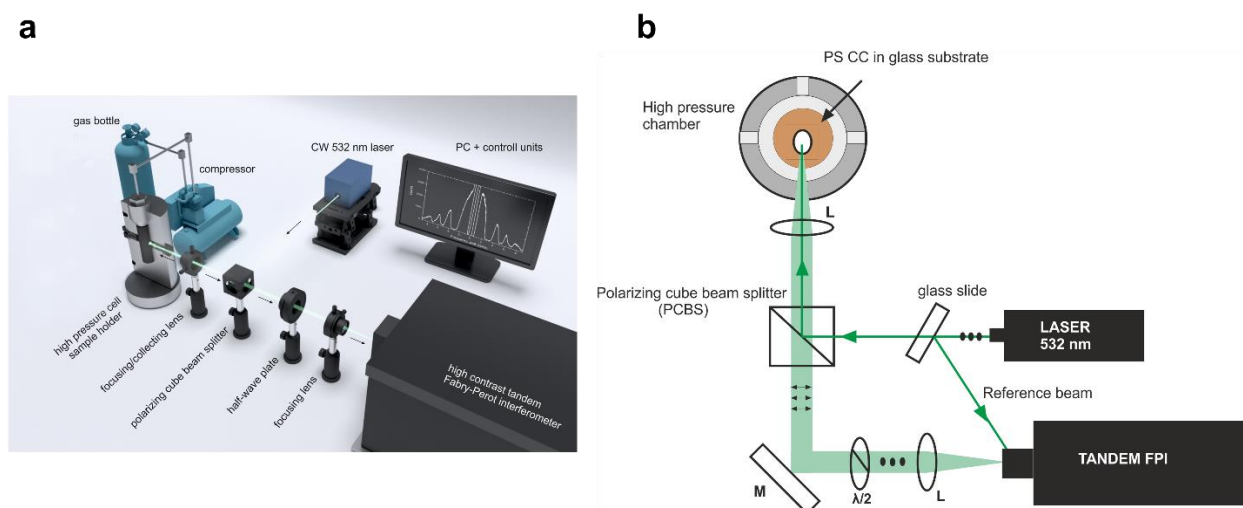


Figure 3.4: (a, b) Schematic of the in-situ BLS experimental setup for measuring PS CCs exposed to high-pressure gasses. The image in (a) is reproduced from ref. ¹.

We measure PS CCs exposed to gas pressure in the backscattering geometry, providing the maximum intensity of scattered light ^{22,110}. A CW laser of $\lambda = 532$ nm (green) is used as the probing light source, shown in Figure 3.4. Using a thin glass slide, a part of the incident light is directed to the diffuser of the tandem FPI. The light from the laser is s-polarized with respect to the propagating medium, which is completely reflected toward the sample by a polarizing cube beam splitter (PCBS) (Thorlabs, PSB103). PCBS reflects s-polarized and transmits p-polarized light; for PSB103, the reflection efficiency is $> 95\%$, and transmission efficiency is $>90\%$. We use an achromatic lens of 125 mm focal length to focus the laser beam on the sample through the chamber window. The laser beam hits the PS CC sample perpendicularly to the sample substrate. Due to the multiple scattering from dry colloidal samples ¹⁶⁶, the light scattered from the acoustic phonons of PS CC is depolarized, and the wave vector is ill-defined ¹¹¹. However, the surrounding gas molecules do not depolarize the light, and therefore, in this case, the light inelastically scattered on the pressure waves in the gas molecules is s-polarized. The scattered light (thick green line) from the chamber is collected using the same achromatic lens and transmitted through the PCBS. Notably, the cross-polarization (s-p) arrangement suppresses the BLS signal originating from the inelastic light scattering on the pressure waves in gas ¹⁶⁷. On the other hand, at high pressure the BLS signal from the chamber containing the PS CC sample is overwhelmed by the gas signal which makes it difficult to analyze the data. The scattered beam is reflected towards the tandem FPI using a mirror. We use a half-wave plate to rotate the polarization of backscattered light by 90° so that the transmitted light becomes s-polarized and FPI can detect the signal. Finally, we use an achromatic lens having a 150 mm focal length to focus the backscattered beam onto the pinhole of FPI.

In this section, we discuss the BLS spectra of the as-prepared PS CC samples measured at ambient room conditions (1 bar air, RT). The experimental results from He/Ar/N₂ high-pressure studies of PS CCs are discussed in the following chapters.

Figure 3.6a shows an exemplary BLS spectrum normalized by the thermal phonon population factor ⁴⁴ of PS CCs made of PS NPs with $d = 610$ nm (PS610). The spectrum consists of two asymmetric peaks assigned to the dipolar (1,1) and quadrupolar (1,2) spheroidal Lamb modes ^{111,112}. The low-frequency (1,1) mode, which refers to the translational vibration of the CC, is represented by Asym2sig function ¹⁶⁶ to yield its spectral position at f_{11} . Notably, this peak appears

only in the presence of mechanical interactions (contacts) between neighboring NPs. In other words, f_{11} reduces to zero for a single particle.

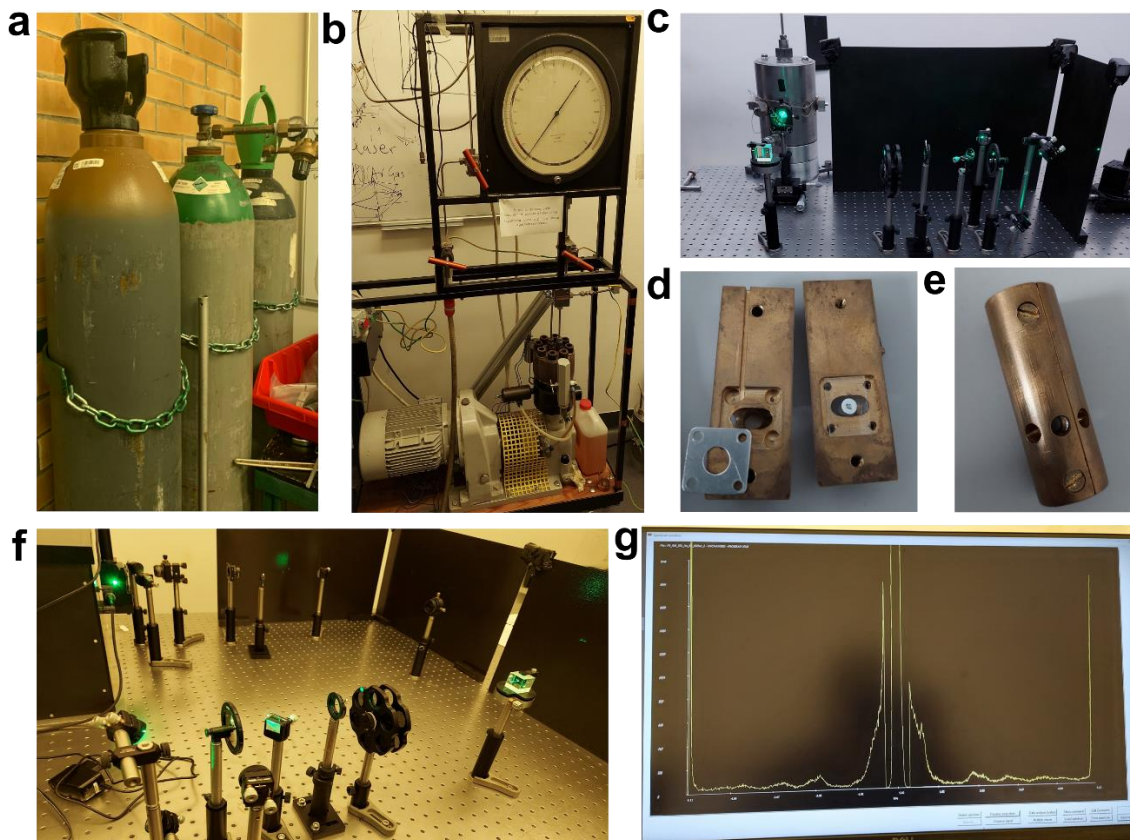


Figure 3.5: (a) He, Ar, and N₂ gas bottles used for high-pressure measurements (b) gas compressor with the pressure indicator. (c) high-pressure chamber (d, e) cylindrical sample holder for PS CC samples (f) aligned optical elements on the table, part of the high-pressure BLS setup. (g) a sample spectrum of the as-prepared PS610 CC shown on the computer screen. The images (a – g) are taken from the laboratory in the Molecular Biophysics division, Faculty of Physics, UAM, Poznan, Poland.

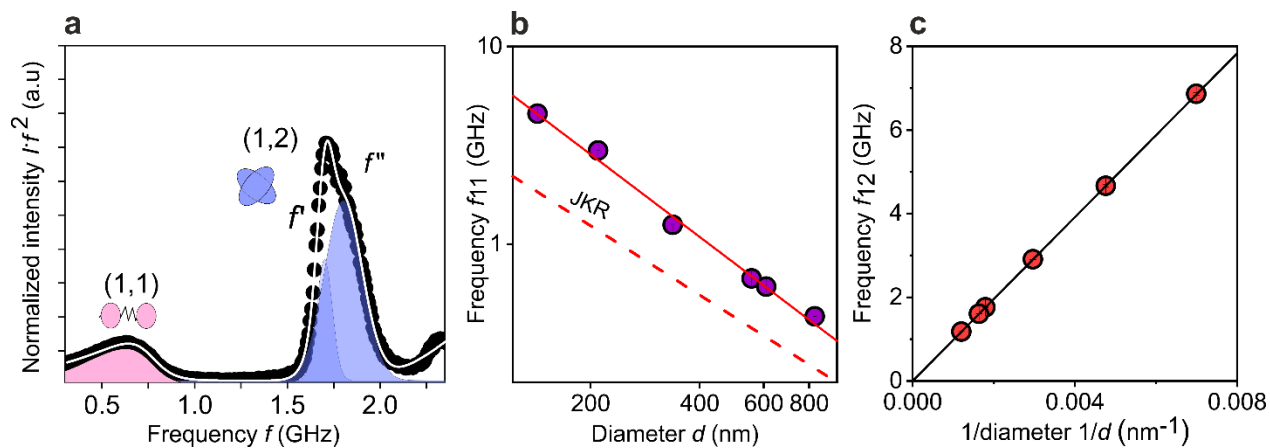


Figure 3.6: (a) Normalized BLS spectrum (solid black circles, anti-Stokes side) of pristine (1 bar air, RT, 296 K) PS CCs made of 610 nm (PS610) diameter NPs showing the peaks corresponding to dipolar (1,1) and quadrupolar (1,2) modes of vibration. The peak corresponding to the (1,1) mode is fitted with Asym2sig function and (1,2) with two Gaussian curves. (b) The frequency of (1,1) mode as a function of diameter. The solid red line shows the exponential function fit, and the dashed red line represents the theoretical trend based on the JKR model. (c) The frequency of the (1,2) mode of PS610 CC is represented as a function of the inverse of the diameter measured from SEM. The solid black line corresponds to the expected values calculated based on Equation 3.8.

Using the phonon density of states (DOS) of an *fcc* crystal, f_{11} can be related to the effective stiffness constant K_{eff} of the interparticle contacts¹⁶⁶ given by:

$$2\pi f_{11} = 2 \left(\frac{2K_{\text{eff}}}{M} \right)^{\frac{1}{2}}, \quad (3.1)$$

, where M is the mass of the NP, $M = \frac{\pi}{6} d^3 \rho$ and the effective stiffness constant (K_{eff}) can be expressed as:

$$K_{\text{eff}} = \frac{9}{5} \left(\frac{3\pi W_{\text{PS-PS}} R_{\text{eff}}^2 E_{\text{eff}}^2}{4} \right)^{\frac{1}{3}}, \quad (3.2)$$

where $W_{\text{PS-PS}}$ is the work of adhesion, the effective radius R_{eff} is calculated from the expression:

$$\frac{1}{R_{\text{eff}}} = \frac{1}{R_1} + \frac{1}{R_2} \quad (3.3)$$

and for monodispersed NPs, $R_1 = R_2 = R$; $R_{\text{eff}} = \frac{R}{2}$.

The effective elastic modulus E_{eff} is given by:

$$E_{\text{eff}} = \frac{4}{3} \left(\frac{1 - \nu_1^2}{E_1} + \frac{1 - \nu_2^2}{E_2} \right)^{-1} \quad (3.4)$$

Using the bulk properties of PS listed in Table 3.1, for two identical PS NPs, E_{eff} can be simplified to:

$$E_{\text{eff}} = \frac{2}{3} \frac{E}{(1 - \nu^2)} = 3.05 \text{ GPa} \quad (3.5)$$

From Johnson-Kendall-Roberts (JKR) model ^{166,168,169}, under zero load, the contact radius (a_0^{JKR}) between two identical NPs is given by:

$$a_0^{\text{JKR}} = \left(\frac{3\pi d^2 W}{8E_{\text{eff}}} \right)^{\frac{1}{3}} \quad (3.6)$$

And using Eqns. 3.1 - 3.6, we can relate f_{11} to a_0^{JKR} by:

$$a_0^{\text{JKR}} = \frac{5\pi^2 M f_{11}^2}{9E_{\text{eff}}} \quad (3.7)$$

Table 3.1: Material properties of polystyrene (PS) used in calculations ^{1,170-172}.

v_t	v_l	E	ν	ρ	l	m	a	b	c	$W_{\text{PS-PS}}$	C_{eff}
$\text{m}\cdot\text{s}^{-1}$	$\text{m}\cdot\text{s}^{-1}$	GPa		$\text{kg}\cdot\text{m}^{-3}$	GPa	GPa	GPa	GPa	GPa	$\text{J}\cdot\text{m}^{-2}$	GPa
1210	2350	4.1	0.32	1050	2.889	1.381	-18.9	-13.3	-10	0.0636	5.79

Table 3.2: Expected Contact radius a_0^{JKR} calculated from Eq. 3.6 using Table 3.1.

Particle diameter d (nm)	a_0^{JKR} (nm)
143	8
210	10
337	14
556	20
610	21
830	26

Additionally, f_{11} can be used to determine the effective elastic constant of PS CCs. In an *fcc* crystal, the longitudinal phonon velocity along the [100] direction ¹⁶⁶ is given by:

$$v_{[100]} = (\pi d f_{11}) / \sqrt{2} \quad (3.8)$$

C_{eff} is given by:

$$C_{\text{eff}} = \rho_{\text{eff}} v_{[100]}^2 \quad (3.9)$$

$$C_{\text{eff}} = \frac{1}{2} \rho_{\text{eff}} \pi^2 d^2 f_{11}^2 \quad (3.10)$$

For an *fcc* CC, the packing efficiency is 74% and the void fraction is 26%. The effective mass density is estimated by considering the mass density of polystyrene (ρ_{PS}) and the mass density of air (ρ_{air}) in the void. Thus,

$$\rho_{\text{eff}} = 0.74 \cdot \rho_{\text{PS}} + 0.26 \cdot \rho_{\text{air}} = 777 \text{ kg/m}^3 \quad (3.11)$$

with $\rho_{\text{PS}} = 1050 \text{ kg}\cdot\text{m}^{-3}$ and $\rho_{\text{air}} = 1.2 \text{ kg}\cdot\text{m}^{-3}$ at 1 bar and 293 K.

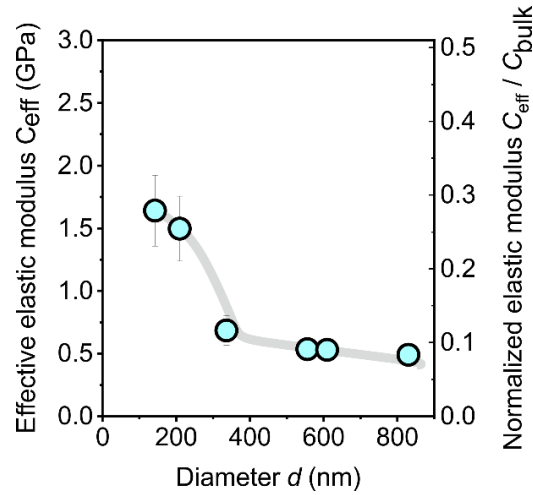


Figure 3.7: Effective elastic modulus (C_{eff}) and the normalized elastic modulus ($C_{\text{eff}}/C_{\text{bulk}}$) of pristine PS CCs represented as a function of particle diameter (d).

Figure 3.6 b represents the experimental f_{11} (solid purple circles) values obtained as a function of NP diameter. Based on JKR model¹⁷⁰, for weak interparticle bonding, the scaling relation should be $f_{11} \propto d^{-7/6}$. However, the measured f_{11} deviates from the calculated JKR trend (red dashed line); the obtained exponential fit (red solid line) is 19% higher than the theoretical prediction rescaling to $f_{11} \propto d^{-1.39}$. This observation implies the significant role of intrinsic fabrication impurities in developing solid contact bridges^{23,173} in addition to van der Waals interactions in pristine PS CCs, as evident from the SEM images in Figure 3.3. Figure 3.7 shows the effective elastic modulus (C_{eff}) according to Eq. 3.10 for pristine PS CC samples as a function of the NP diameter. With the increasing NP d , C_{eff} drops from ~ 1.64 to 0.49 GPa; the C_{eff} for the measured

pristine PS CCs are given in Table 3.3. The right y-axis in Figure 3.7 represents the normalized elastic modulus ($C_{\text{eff}}/C_{\text{bulk}}$) for the pristine CCs, where $C_{\text{bulk}} = C_{11}$ of bulk PS = 5.79 GPa. The normalized elastic modulus ≤ 1 implies that the obtained C_{eff} of the pristine samples are much lower than the C_{bulk} .

The frequency of the quadrupolar (1,2) mode f_{12} depends on the elastic properties of the material and the interactions of surrounding particles in CCs. In general, the contacts lower the spherical symmetry of the NP, which results in the blueshift and spectral split of this mode⁴⁴. Therefore, the peak corresponding to (1,2) mode can be represented by two Gaussian line shapes centered at f' and f'' as indicated in Figure 3.6a. As previously reported, the value representing $f_{12} = 2f' - f''$, approximately gives the frequency of the (1,2) mode for a single particle, free from surrounding interactions⁴⁴. From the Lamb theory of spherical particles, the frequency of (1,2) mode can be related to the particle diameter as:

$$f_{12} = Av_t/d, \quad (3.8)$$

where $A \approx 0.81$ for polystyrene¹¹².

Table 3.3: Effective elastic modulus (C_{eff}) of pristine samples calculated from Eq. 3.10.

Particle diameter d (nm)	C_{eff} (GPa)
143 ± 4	1.641 ± 0.001
210 ± 7	1.497 ± 0.006
337 ± 1	0.683 ± 0.001
556 ± 7	0.534 ± 0.003
610 ± 1	0.530 ± 0.002
830 ± 3	0.490 ± 0.002

Table 3.4: Comparison of particles' diameters obtained from BLS and SEM for pristine samples.

Sample	d from SEM (nm)	d from BLS (nm)
PS143	140 ± 2	143 ± 4
PS210	200 ± 2	210 ± 7
PS337	336 ± 3	337 ± 1
PS556	553 ± 4	556 ± 7
PS610	610 ± 3	610 ± 1
PS830	831 ± 3	830 ± 3

In Figure 3.4c, the experimental f_{12} values (solid red circles) are plotted as a function of the inverse of the diameter ($1/d$) obtained from SEM. As given in Figure, the experimental data points show a good agreement with the theoretical trend (solid black line) calculated using Eq. 3.8 and elastic properties of bulk PS given in Table 3.1. The d values obtained from the experimental f_{12} values are given in Table 3.4. It shows a good agreement with the SEM d values (analyzed using imageJ software), signifies the reliable determination of NP d using BLS. In this thesis, the d from BLS is used, and the samples are named accordingly. Moreover, the contact radii measured from the SEM images of pristine using ImageJ software is shown in Table 3.5.

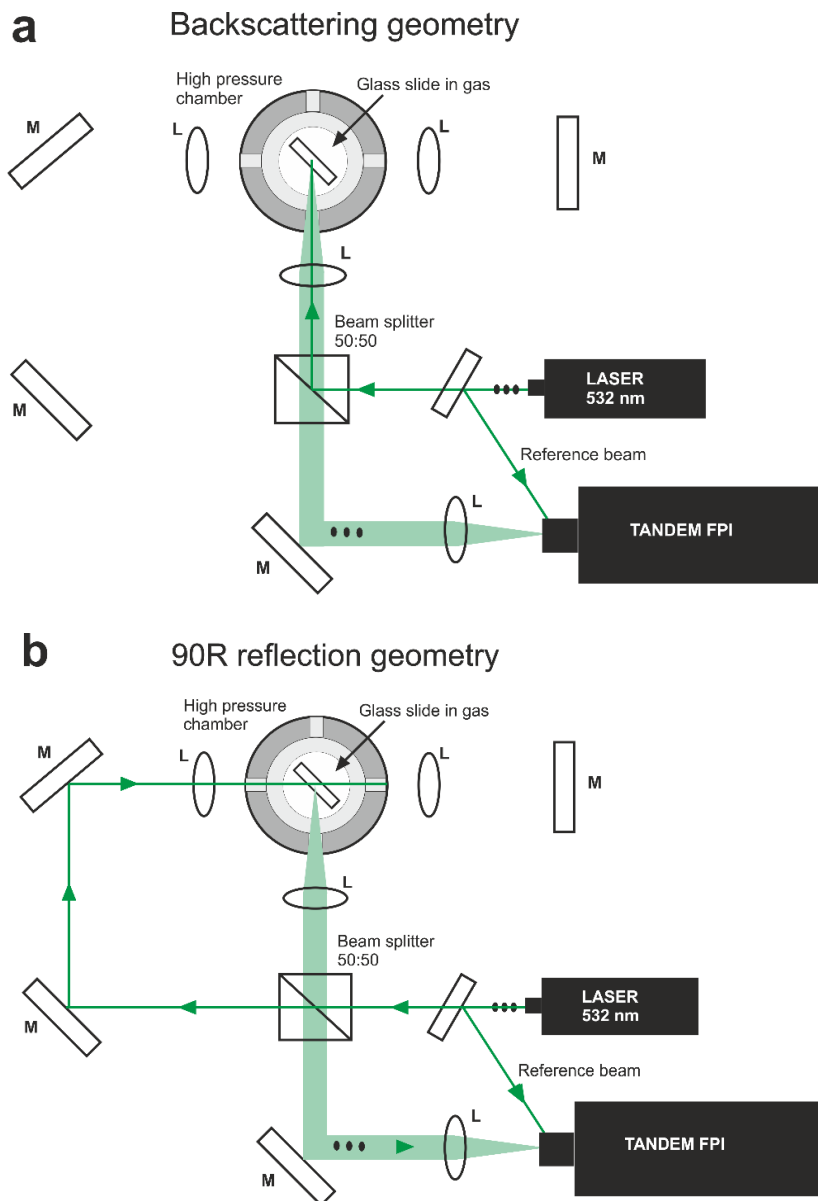
Table 3.5: Contact radius (a_0) of pristine samples measured from SEM images.

Particle diameter d (nm)	a_0 from SEM (nm)
143 ± 4	31 ± 3
210 ± 7	33 ± 4
337 ± 1	46 ± 5
556 ± 7	46 ± 6
610 ± 1	59 ± 8
830 ± 3	81 ± 6

Chapter 4

Elastic properties of supercritical fluids

Brillouin light scattering (BLS) can be used to measure the acoustic properties of gasses at a specific pressure. Here, we discuss the determination of the refractive index (n), longitudinal sound velocity (v_l) and acoustic impedance (Z) of He, N₂ and Ar gasses at various pressures ranging from 1 bar to 1000 bar at room temperature (RT, 296K).



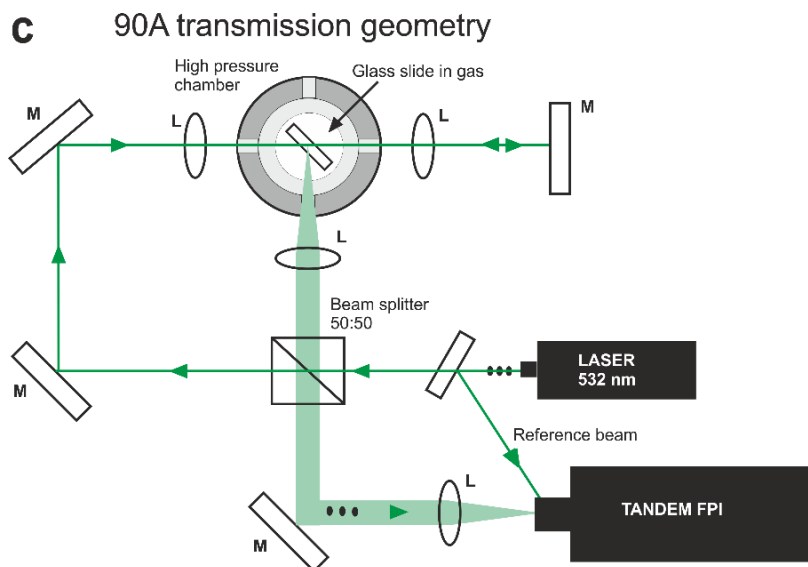


Figure 4.1: BLS triple geometry setup for the determination of n of gasses at different pressures in (a) backscattering, (b) 90R reflection, and (c) 90A transmission geometries. The sample is a thin glass slide oriented at 45° to the incident laser beam ($\lambda = 532$ nm) surrounded by the gas (He, N₂, or Ar) at various pressures. The thin green line with the arrowheads denotes the direction of the incident laser beam, whereas the thick green line denotes the scattered beam from the glass sample directed to the tandem FPI. The black dots represent the s-polarization of the laser light, which is preserved after the scattering process.

At first, we determine n of the gas (n_{gas}) (He, N₂, or Ar) at different p conditions using the triple geometry (backscattering, 90R reflection, and 90A transmission) setup. Although the experiment is done simultaneously in three geometries, for clarity, the light paths for the geometries used are separately represented in Figures 4.1a-c. We use a high-pressure system consisting of a cylindrical sample chamber attached to glass windows for the incident laser beam, gas compressor, and gas bottles^{1,19}. For the measurement of n_{gas} , a thin glass slide is kept inside the sample chamber at an angle of 45° to the incident green laser beam¹⁷⁴ (Spectra-Physics Excelsior 300, $\lambda = 532$ nm). A part of the green laser is directed to the reference pinhole of the tandem Fabry-Perot interferometer (JRS Scientific Instruments) using a thin glass slide. We use a non-polarizing cube beam splitter (Thorlabs; BS013; R:T = 50:50) in the path of incident light, which splits the beam to perform the triple geometry measurements. Three achromatic lenses of 125 mm focal length focus the laser light on the glass sample through the chamber windows from different directions. The scattered light transmitted through the beam splitter is focused on the pinhole of the FPI using a 200 nm focal length achromatic lens.

Initially, we perform the reference measurement at ambient room conditions (1 bar air, RT) in 90A (transmission), 90R (reflection), and in backscattering (BS) geometries simultaneously. Further, the gas at a given p is supplied to the chamber via an external metal pipe, and BLS measurements are taken at different p conditions starting from 50 bar to 1000 bar at a constant step of 50 bars. Before every measurement, 5 minutes time interval is taken to stabilize the temperature change. An example of the spectrum obtained for the glass sample at ambient room conditions in three different geometries simultaneously is given in Figure 4.2a. The peaks at 15.48 GHz, 29.73 GHz, and 33.51 GHz correspond to the longitudinal acoustic frequency of the glass sample measured in 90A, 90R, and BS geometries¹⁷⁵, respectively. The peak at 24 GHz originates from the longitudinal acoustic wave of the chamber window glass, measured in BS geometry, as represented in Figure 4.2b. The spectral peaks are fitted by the Lorentzian function, and the frequencies (f) are determined.

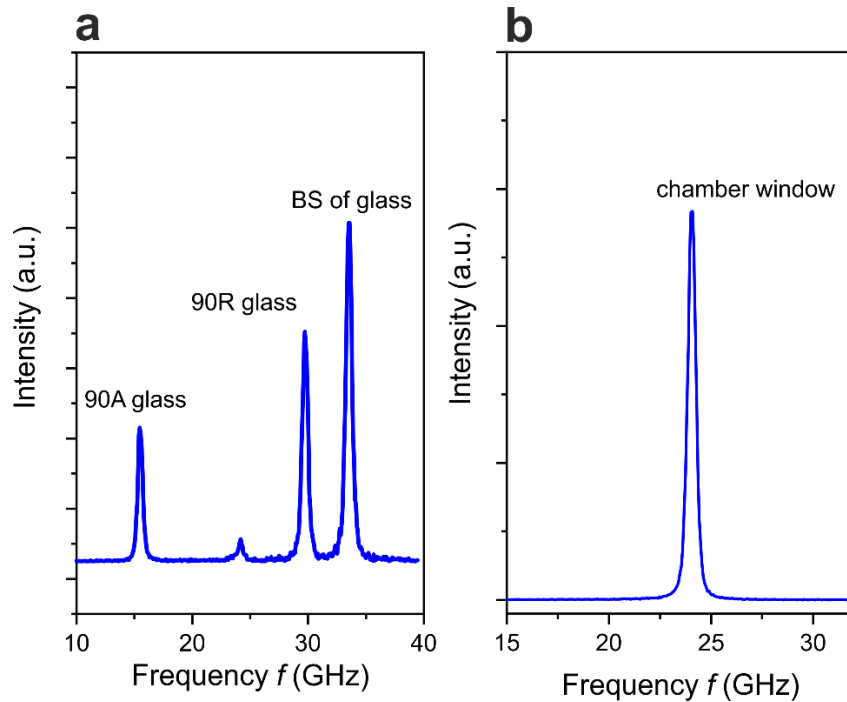


Figure 4.2: (a) BLS spectrum representing the peaks corresponding to longitudinal acoustic waves propagating in the glass sample measured in 90A, 90R, and BS geometries at ambient room conditions (1 bar air, RT, 296 K). (b) BLS spectrum obtained from the chamber window glass measured in BS geometry represents the longitudinal wave peak centered at 24 GHz.

The magnitude of wave vectors (\mathbf{q}) corresponding to the measured geometries¹⁷⁶ are given as:

$$\mathbf{q}_{90A} = \frac{2\pi\sqrt{2}}{\lambda} n_{\text{gas}} \quad (4.1)$$

$$\mathbf{q}_{\text{BS}} = \frac{4\pi n_{\text{g}}}{\lambda} \quad (4.2)$$

$$q_{90R} = \frac{2\pi}{\lambda} \sqrt{4n_{\text{g}}^2 - 2n_{\text{gas}}^2}, \quad (4.3)$$

where n_{g} is the refractive index of the glass slide. Notably, q_{90A} is dependent only on the surrounding gaseous medium and the wavelength of the probing light. Since $\omega = v_1 q$ and $\omega = 2\pi f$, the frequency of the longitudinal acoustic phonons of glass in 90A transmission geometry (f_{90A}) can be related to the sound velocity through the glass ($v_{1,\text{g}}$) as:

$$v_{1,\text{g}} = \frac{2\pi f_{90A}}{q_{90A}}. \quad (4.4)$$

For the reference measurement, at 1 bar air, $n_{\text{gas}} = n_{\text{air}} = 1$ and,

$$v_{1,\text{g}} = \frac{f_{90A}\lambda}{\sqrt{2}} \approx 5.82 \cdot 10^3 \text{m}\cdot\text{s}^{-1}. \quad (4.5)$$

We assume that $v_{1,\text{g}}$ remains constant with the applied pressure on the glass. Now, the frequency of the glass sample in BS geometry f_{BS} is related to $v_{1,\text{g}}$ as:

$$f_{\text{BS}} = \frac{2v_{1,\text{g}}n_{\text{g}}}{\lambda}, \quad (4.6)$$

and we can obtain n_{g} at different gas pressures. Comparing the magnitude of wave vectors in 90A and BS geometries:

$$\frac{q_{90A}}{q_{\text{BS}}} = \frac{f_{90A}}{f_{\text{BS}}} = \frac{n_{\text{gas}}}{\sqrt{2}n_{\text{g}}}, \quad (4.7)$$

we can obtain n_{gas} for different p conditions. Similarly, the values of n_{gas} at different p can be verified by comparing \mathbf{q}_{90A} and \mathbf{q}_{90R} as:

$$\frac{q_{90A}}{q_{90R}} = \sqrt{\frac{n_{\text{gas}}^2}{2n_g^2 - n_{\text{gas}}^2}} \quad (4.8)$$

To obtain sound velocities of gasses $v_{l,\text{gas}}$ at different p conditions, we performed BLS measurements in 90A and BS geometry considering Ar, He, or N_2 gas as the sample. The experimental setup is similar to that in Figure 4.1, the glass slide is removed, and the gas is supplied to the chamber at different p conditions.

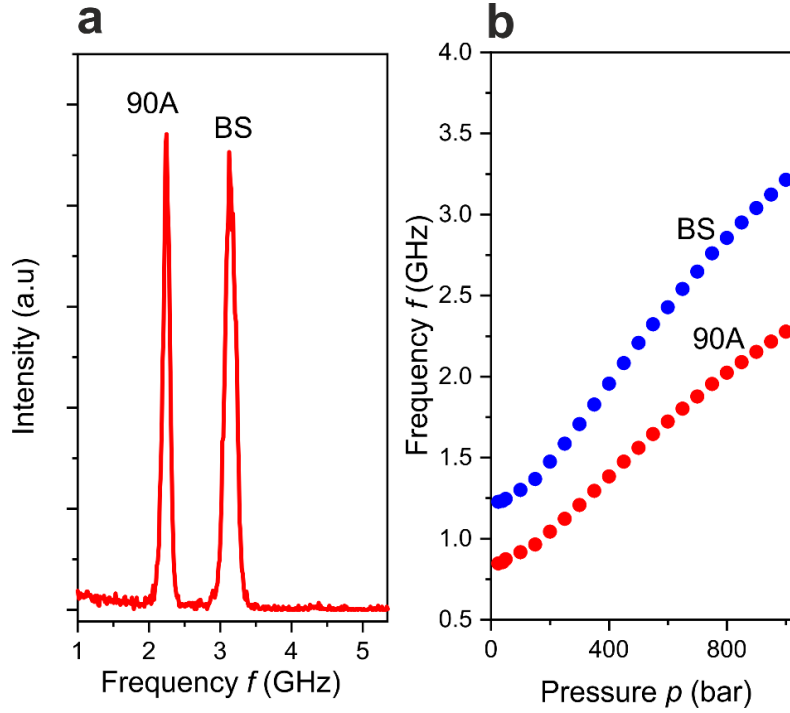


Figure 4.3: (a) BLS spectrum of Ar gas measured at $p = 1000$ bar at RT showing two peaks corresponding to longitudinal acoustic waves centered at 2.25 GHz for 90A and 3.12 GHz for BS geometry. (b) The Brillouin shift at different p of Ar at RT measured in 90A (solid red circle) and BS (solid blue circles) geometry.

An exemplary BLS spectrum measured at 1000 bar of Ar is given in Figure 4.3a. The peaks corresponding to longitudinal acoustic waves of the gas are centered at 2.25 GHz and 3.12 GHz measured in 90A and BS geometry, respectively. The gas peaks were fitted by the Lorentzian function to obtain $f_{90A,\text{gas}}$ and $f_{BS,\text{gas}}$ at various pressures, as shown in Figure 4.3b. Using Eq. 4.9, we obtained $v_{l,\text{gas}}$ at different p conditions:

$$v_{l,\text{gas}} = \frac{f_{BS,\text{gas}}\lambda}{2n_{\text{gas}}} \quad (4.9)$$

The values of $v_{1,\text{gas}}$ can be verified by using f measured from 90A geometry as:

$$v_{1,\text{gas}} = \frac{f_{90\text{A,gas}}\lambda}{\sqrt{2}n_{\text{gas}}} \quad (4.10)$$

Figure 4.4a represents the $v_{1,\text{gas}}$ for He, Ar and N₂ gases from 50 bar to 1000 bar at RT. Now, acoustic impedance Z of the gasses can be calculated from the relation,

$$Z = \rho v_{1,\text{gas}} \quad (4.11)$$

Figure 4.4b shows the Z obtained for different p conditions. The mass density ρ of gasses at the corresponding p values is taken from the standard reference database¹⁷⁷⁻¹⁷⁹. The n , $v_{1,\text{gas}}$ and Z of He, N₂ and Ar gasses at different p conditions at RT are given in Tables 4.1 - 4.3, respectively.

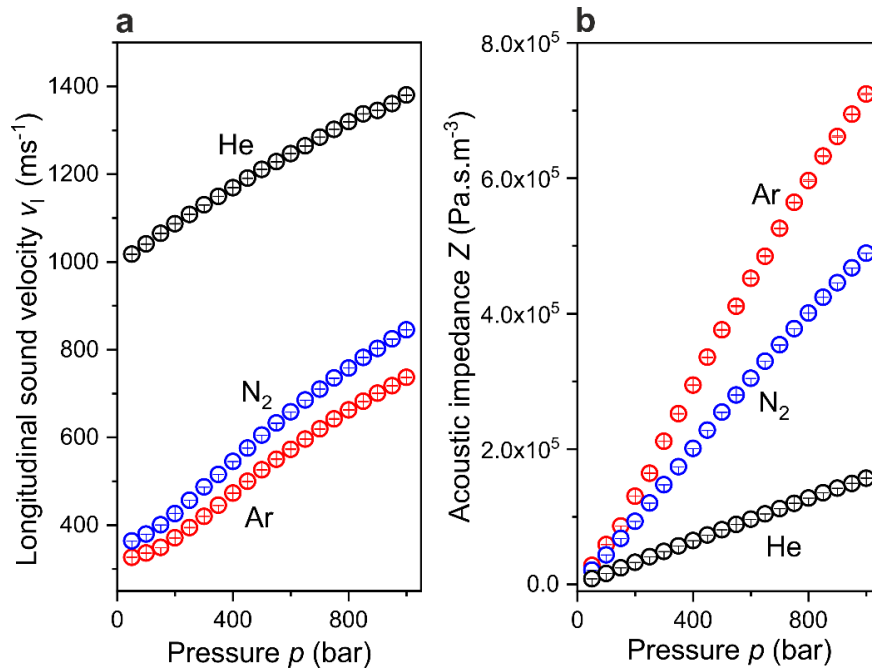


Figure 4.4: (a) Longitudinal sound velocity (v_1) and (b) acoustic impedance (Z) obtained by BLS measurements of He, N₂ and Ar gasses at different pressures.

Table 4.1: n , v_1 and Z values of He gas at various pressures.

Pressure p (bar)	Refractive Index n	Sound velocity v_1 ($\text{m}\cdot\text{s}^{-1}$)	Acoustic impedance Z ($\text{kg}\cdot\text{m}^{-2}\cdot\text{s}^{-1}$)
50	1.0016 ± 0.0005	1017.3 ± 1.2	8173 ± 9
100	1.0029 ± 0.0004	1040.8 ± 0.5	16335 ± 8
150	1.0045 ± 0.0004	1065.0 ± 0.5	24527 ± 12
200	1.0062 ± 0.0005	1086.8 ± 0.6	32666 ± 18
250	1.0074 ± 0.0004	1108.3 ± 0.6	40751 ± 20
300	1.0084 ± 0.0004	1129.7 ± 0.6	48831 ± 25
350	1.0100 ± 0.0005	1149.4 ± 0.6	56867 ± 30
400	1.0111 ± 0.0004	1169.1 ± 0.6	64820 ± 30
450	1.0114 ± 0.0005	1190.9 ± 0.7	72850 ± 40
500	1.0126 ± 0.0005	1210.8 ± 0.7	80880 ± 40
550	1.0144 ± 0.0004	1228.6 ± 0.6	88750 ± 50
600	1.0147 ± 0.0004	1246.8 ± 0.6	96420 ± 50
650	1.0166 ± 0.0005	1264.3 ± 0.7	104320 ± 50
700	1.01671 ± 0.00036	1284.2 ± 0.6	112060 ± 50
750	1.0177 ± 0.0004	1302.2 ± 0.7	119910 ± 60
800	1.0187 ± 0.0004	1319.6 ± 0.7	127580 ± 60
850	1.0191 ± 0.0004	1337.6 ± 0.7	135230 ± 70
900	1.0205 ± 0.0004	1345.0 ± 0.8	141970 ± 80
950	1.0211 ± 0.0004	1360.6 ± 0.7	149260 ± 80
1000	1.0212 ± 0.0004	1380.3 ± 0.8	157040 ± 90

Table 4.2: n , v_1 and Z values of N_2 gas at various pressures.

Pressure p (bar)	Refractive Index n	Sound velocity v_1 ($m \cdot s^{-1}$)	Acoustic impedance Z ($kg \cdot m^{-2} \cdot s^{-1}$)
50	1.0145 ± 0.0005	363.66 ± 0.35	21037 ± 20
100	1.0281 ± 0.0005	379.21 ± 0.29	43575 ± 33
150	1.0413 ± 0.0005	400.52 ± 0.32	67700 ± 50
200	1.05344 ± 0.00038	426.37 ± 0.28	93240 ± 60
250	1.06438 ± 0.00036	456.56 ± 0.29	120160 ± 80
300	1.07411 ± 0.00033	486.65 ± 0.27	147260 ± 80
350	1.08338 ± 0.00032	515.26 ± 0.27	173870 ± 90
400	1.09040 ± 0.00033	544.99 ± 0.29	200720 ± 100
450	1.09731 ± 0.00031	575.54 ± 0.29	227780 ± 110
500	1.10311 ± 0.00029	605.05 ± 0.26	254360 ± 110
550	1.10952 ± 0.00032	632.41 ± 0.28	279920 ± 120
600	1.11371 ± 0.00027	657.92 ± 0.28	304510 ± 130
650	1.11832 ± 0.00027	685.10 ± 0.26	329750 ± 130
700	1.12284 ± 0.00026	710.04 ± 0.28	353840 ± 140
750	1.12683 ± 0.00025	734.96 ± 0.27	377820 ± 140
800	1.13014 ± 0.00028	758.15 ± 0.32	400860 ± 170
850	1.13261 ± 0.00027	782.33 ± 0.30	424330 ± 160
900	1.13612 ± 0.00026	802.70 ± 0.33	445680 ± 180
950	1.13926 ± 0.00028	824.08 ± 0.36	467510 ± 200
1000	1.14205 ± 0.00027	845.25 ± 0.28	489150 ± 160

Table 4.3: n , v_1 and Z values of Ar gas at various pressures.

Pressure p (bar)	Refractive Index n	Sound velocity v_1 ($\text{m}\cdot\text{s}^{-1}$)	Acoustic impedance Z ($\text{kg}\cdot\text{m}^{-2}\cdot\text{s}^{-1}$)
50	1.0141 ± 0.0006	326.5 ± 0.4	27980 ± 38
100	1.0281 ± 0.0006	336.2 ± 0.5	58910 ± 90
150	1.0428 ± 0.0005	348.8 ± 0.5	86320 ± 110
200	1.0581 ± 0.0004	370.7 ± 0.6	130460 ± 230
250	1.0698 ± 0.0004	394.2 ± 0.7	164210 ± 300
300	1.08163 ± 0.00031	419.9 ± 0.5	211500 ± 270
350	1.09263 ± 0.00031	444.8 ± 0.6	252270 ± 340
400	1.10121 ± 0.00030	472.7 ± 0.7	294400 ± 400
450	1.10885 ± 0.00025	499.4 ± 0.7	335600 ± 500
500	1.11659 ± 0.00026	525.7 ± 0.8	376100 ± 500
550	1.12301 ± 0.00022	550.2 ± 0.8	410900 ± 600
600	1.12705 ± 0.00024	573.1 ± 0.8	452300 ± 600
650	1.13399 ± 0.00024	595.8 ± 0.7	484800 ± 600
700	1.13801 ± 0.00026	618.9 ± 0.8	525800 ± 700
750	1.14308 ± 0.00021	642.2 ± 0.9	564300 ± 700
800	1.14713 ± 0.00025	662.3 ± 0.9	596500 ± 800
850	1.15064 ± 0.00026	682.2 ± 0.8	632700 ± 700
900	1.15444 ± 0.00023	700.3 ± 0.9	661500 ± 900
950	1.15753 ± 0.00023	717.7 ± 0.8	694500 ± 700
1000	1.16031 ± 0.00026	736.7 ± 0.8	724300 ± 800

Chapter 5

PS CCs in high-pressure Helium gas

5.1 Brillouin light scattering experiment

In this section, we discuss the pressure-dependent BLS experiments performed for PS CCs (as described in section 3.3), d in the range of 143 nm to 830 nm, using He gas at RT. The experiment is performed by varying the gas pressure from 1 bar to 1000 bar at a constant step of 50 bars in 13 minutes, sufficient to record good-quality BLS spectra. Before the each measurement, a few minute interval is taken to equilibrate the temperature after pressurizing the system.

5.2 Pressure-dependent vibrational frequencies

In order to understand the dependence of hydrostatic pressure on the vibrational frequencies of PS NPs, we calculate p - dependent f_{11} and f_{12} based on the nonlinear theory of elasticity. For a nonlinear elastic material, the change in the bulk modulus $B(p)$ and shear modulus $G(p)$ ¹⁸⁰ with p is given by:

$$B(p) = \lambda' + \frac{2}{3}\mu' - \frac{18a + 2c}{9\lambda' + 6\mu'}p \quad (5.1)$$

$$G(p) = \mu' - \frac{6b - c + 6\lambda' + 6\mu'}{6l + 4\mu'}p \quad (5.2)$$

The Young modulus $E(p)$ and Poisson ratio $\nu(p)$ can be related to Eq. (5.1) and (5.2) as:

$$E(p) = \frac{9B(p)G(p)}{3B(p) + G(p)} \quad (5.3)$$

$$\nu(p) = \frac{E(p)}{2G(p)} - 1 \quad (5.4)$$

The calculated values for $B(p)$, $G(p)$, $E(p)$ and $\nu(p)$ are given in Table 5.1 and the graphical representation of the elastic constants with p is given in Figure 5.1.

i. Calculation of the dipolar mode frequency as a function of pressure $f_{11}(p)$

To calculate $f_{11}(p)$, the effective elastic modulus $E_{\text{eff}}(p)$ is given by:

$$E_{\text{eff}}(p) = \frac{2}{3} \frac{E(p)}{(1-\nu(p)^2)}. \quad (5.5)$$

The effective spring constant $K_{\text{eff}}(p)$ can be rewritten as:

$$K_{\text{eff}}(p) = \frac{9}{5} \left(\frac{3\pi W_{\text{PS-PS}} R_{\text{eff}}^2 E_{\text{eff}}^2(p)}{4} \right)^{\frac{1}{3}}. \quad (5.6)$$

Now,

$$2\pi f_{11}(p) = 2 \left(\frac{2K_{\text{eff}}(p)}{M} \right)^{\frac{1}{2}} \quad (5.7)$$

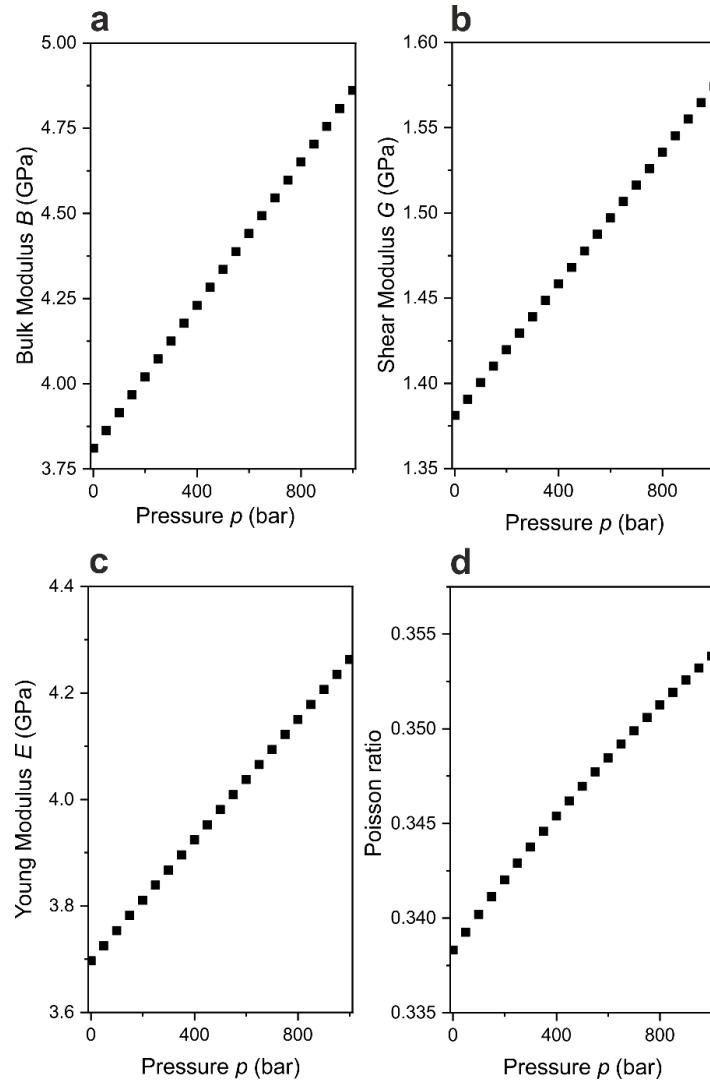


Figure 5.1: (a) Bulk, (b) shear, (c) Young moduli, and (d) Poisson's ratio as a function of the hydrostatic pressure calculated using Eq. 5.1-5.4.

Table 5.1: Pressure-dependent elastic constants used in the calculation of $f_{11}(p)$ and $f_{12}(p)$.

Pressure p [bar]	Bulk modulus $B(p)$ [GPa]	Shear modulus $G(p)$ [GPa]	Young modulus $E(p)$ [GPa]	Poisson ratio $\nu(p)$ [GPa]
1	3.81	1.38	3.70	0.338
50	3.86	1.39	3.72	0.339
100	3.91	1.40	3.75	0.340
150	3.97	1.41	3.78	0.341
200	4.02	1.42	3.81	0.342
250	4.07	1.43	3.84	0.343
300	4.12	1.44	3.87	0.344
350	4.18	1.45	3.90	0.345
400	4.23	1.46	3.92	0.345
450	4.28	1.47	3.95	0.346
500	4.34	1.48	3.98	0.347
550	4.39	1.49	4.01	0.348
600	4.44	1.50	4.04	0.348
650	4.49	1.51	4.07	0.349
700	4.55	1.52	4.09	0.350
750	4.60	1.53	4.12	0.351
800	4.65	1.54	4.15	0.351
850	4.70	1.55	4.18	0.352
900	4.76	1.55	4.21	0.352
950	4.81	1.56	4.23	0.353
1000	4.86	1.57	4.26	0.354

ii. Calculation of the quadrupolar mode frequency as a function of pressure $f_{12}(p)$

The shear modulus $G(p)$ can be used to calculate transverse sound velocity $v_t(p)$ as:

$$G(p) = \rho v_t^2(p) \quad (5.8)$$

and the frequency of the (1,2) mode $f_{12}(p)$ is given by,

$$f_{12}(p) = \frac{A v_t(p)}{d}, \quad (5.9)$$

where $A = 0.81$ for polystyrene¹¹².

5.3. Acoustic impedance contrast between PS and gas

The nature of the BLS spectra and the vibrational frequencies of PS CCs exposed to supercritical gasses are influenced by the acoustic impedance contrast between PS and the gas at the given pressure. In this section, we consider the relative acoustic contrast between PS and He/N₂/Ar gas,

$\frac{Z_{PS}}{Z_{gas}}$. First, let us calculate the acoustic impedance Z of PS using the equations below,

$$B(p) = \rho(p) \cdot \frac{\Delta P}{\Delta \rho}, \quad (5.10)$$

where $B(p)$ is taken from Table 5.1:

$$Z(p) = \sqrt{B(p) \cdot \rho(p)}, \quad (5.11)$$

where $\rho(1 \text{ bar}) = 1050 \text{ kg} \cdot \text{m}^{-3}$. The Density $\rho(p)$ and acoustic impedance $Z(p)$ of PS is given in Table 5.2.

Now, using Z_{gas} from Table 4.1-4.3 and Z_{PS} from Table 5.2, we can calculate the ratio of acoustic impedances between PS and gas at various pressures. The graphical representation of $\frac{Z_{PS}}{Z_{He}}$, $\frac{Z_{PS}}{Z_{N_2}}$, and

$\frac{Z_{PS}}{Z_{Ar}}$ is shown in Figure 5.2a-c, and the values are given in Table 5.2. $\frac{Z_{PS}}{Z_{He}}$ drops from $\cong 1.2 \cdot 10^4$ at 1

bar to 14.5 at 1000 bar. For N₂ gas, $\frac{Z_{PS}}{Z_{N_2}} \cong 4.9 \cdot 10^3$ at 1 bar, drops down to 4.7 at 1000 bar. In the

case of Ar gas, $\frac{Z_{PS}}{Z_{Ar}} \cong 3.7 \cdot 10^3$ at 1 bar, drops down to 3.2 at 1000 bar.

Table 5.2: Density, acoustic impedance of PS and $\frac{Z_{PS}}{Z_{gas}}$ at different pressures.

Pressure p bar	Density of PS ρ $\text{kg}\cdot\text{m}^{-3}$	Acoustic impedance of PS Z $(\text{kg}\cdot\text{m}^{-2}\cdot\text{s}^{-1})$	$\frac{Z_{PS}}{Z_{He}}$	$\frac{Z_{PS}}{Z_{N2}}$	$\frac{Z_{PS}}{Z_{Ar}}$
1	1050	$200\cdot 10^4$	$1.2\cdot 10^4$	$4.9\cdot 10^3$	$3.7\cdot 10^3$
50	1051	$202\cdot 10^4$	247.0	95.8	73.2
100	1053	$203\cdot 10^4$	124.5	46.6	35.1
150	1054	$204\cdot 10^4$	83.5	30.2	22.5
200	1055	$206\cdot 10^4$	63.2	22.1	16.1
250	1056	$207\cdot 10^4$	50.9	17.3	12.4
300	1058	$209\cdot 10^4$	42.8	14.2	10.0
350	1059	$210\cdot 10^4$	37.0	12.1	8.4
400	1060	$212\cdot 10^4$	32.7	10.5	7.3
450	1061	$213\cdot 10^4$	29.3	9.4	6.4
500	1062	$215\cdot 10^4$	26.6	8.4	5.8
550	1063	$216\cdot 10^4$	24.4	7.7	5.3
600	1064	$217\cdot 10^4$	22.6	7.1	4.9
650	1065	$219\cdot 10^4$	21.0	6.6	4.5
700	1066	$220\cdot 10^4$	19.7	6.2	4.2
750	1067	$222\cdot 10^4$	18.5	5.9	3.9
800	1068	$223\cdot 10^4$	17.5	5.6	3.7
850	1069	$224\cdot 10^4$	16.6	5.3	3.5
900	1070	$226\cdot 10^4$	15.9	5.1	3.4
950	1071	$227\cdot 10^4$	15.2	4.9	3.3
1000	1072	$228\cdot 10^4$	14.5	4.7	3.2

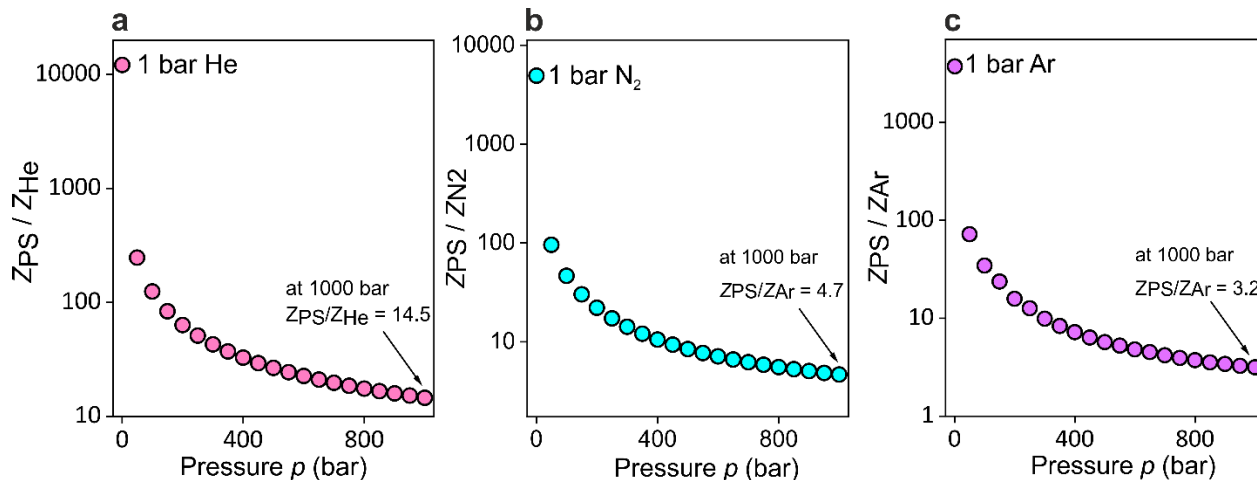


Figure 5.2: Acoustic impedance contrast expressed as a ratio of $\frac{Z_{PS}}{Z_{gas}}$ for (a) He, (b) N₂, and (c) Ar gas.

5.4 BLS experimental results

Figure 5.3 shows the BLS spectra (anti-Stokes side) of PS CCs of $d = 143$ nm, PS143, and $d = 610$ nm, PS610 measured prior (Figures 5.3a and d), during (Figures 5.3b and e) and after (Figures 5.3c and f) exposure to supercritical He, respectively. At first, we discuss the He pressure and NP size dependence on the spectral position and line shape of the low-frequency interaction-induced mode (1,1). For PS143, f_{11} increases from 4.59 GHz for the as-prepared sample at 1 bar air (Figure 5.3a) to 5.18 GHz (Figure 5.3b) at 1000 bar He, producing about 12% frequency blue shift. Upon depressurization, f_{11} returns to 4.60 GHz (Figure 5.3 c), indicating reversible behavior. Conversely, for PS610 CCs, f_{11} slightly decreases from 0.63 GHz for the as-prepared sample (Figure 5.3d) to 0.59 GHz at 1000 bar He (Figure 5.3e), indicating about 6% frequency redshift. However, f_{11} comes back to 0.63 GHz after the pressure release, exhibiting the reversible trend as in the case of PS143. The significantly opposite trend of f_{11} change at 1000 bar He for PS143 and PS610 CCs implies a size-specific effect on the vibrational frequencies of PS CCs by He pressurization, which is discussed in the next section in detail.

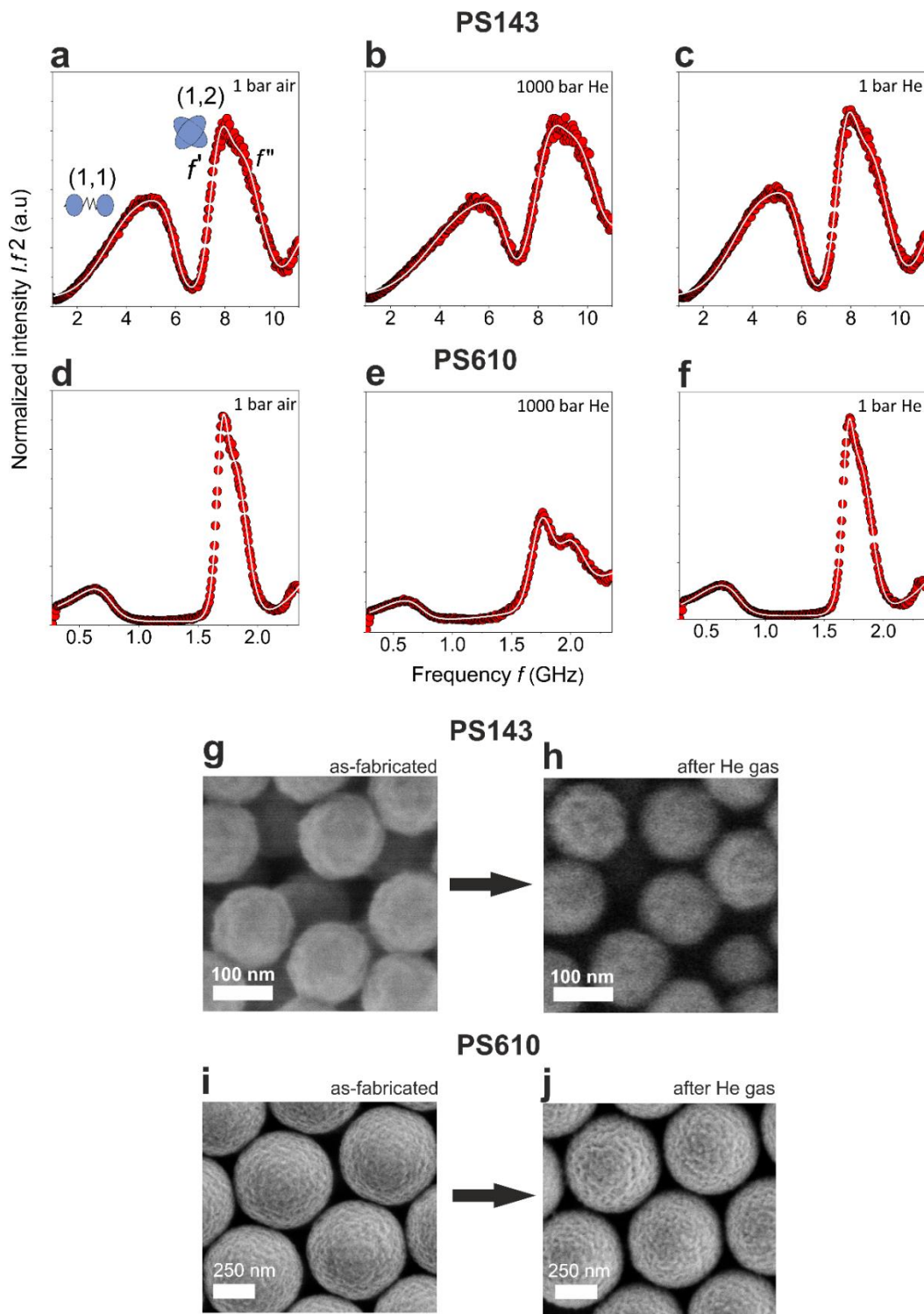


Figure 5.3: Exemplary BLS spectra (anti-Stokes side) of PS CCs of diameter (a-c) $d = 143$ nm, PS143 and (d-f) $d = 610$ nm, PS610 obtained from He gas pressure-dependent measurements at RT. (a, d) As-prepared sample at 1 bar air (b, e) at 1000 bar He (c, f) post-treatment at 1 bar He. SEM images of (g, h) PS143 and (i, j) PS610 CCs, (g, i) before and (h, j) after He gas pressure treatment at 800 bar.

Now, considering the peak associated with the (1,2) mode for PS143 CC, the reduced f_{12} increases from 6.88 GHz for the as-prepared sample (Figure 5.3a) to 7.30 GHz at 1000 bar He (Figure 5.3b). Similar to the case of f_{11} , f_{12} returns to the initial spectral position of 6.89 GHz after depressurization (Figure 5.3c). For PS610, at 1 bar air reduced f_{12} is at 1.60 GHz. After pressurization, at 1000 bar of He, the corresponding peak exhibits blueshift and increased split ($f' = 1.85$ GHz and $f'' = 2.20$ GHz), which points to the increase of particle contacts by hydrostatic compression. However, the reduced f_{12} remains unchanged (about 1.60 GHz), which may mislead to the idea that PS NP elasticity is pressure-independent. Considering only the stiffening due to hydrostatic compression, f_{12} calculated (section 5.2 A ii) should reveal a 5% blueshift at 1000 bar. Therefore, we have to consider all the gas pressure-induced effects to evaluate the change of frequencies. Similar to PS143, the (1,2) mode returns to the initial spectral position after releasing the pressure to 1 bar (Figure 5.3d and f). The reversible nature of the BLS spectra of PS CCs after He gas pressure treatment implies zero increase of particle contacts by He pressurization, which is validated by the similarity of the SEM images in Figures 5.3 g and h for PS143 and i and j for PS610.

The negligible soldering of PS NPs in the CCs by He gas can be explained by the solubility of He in PS, which is expressed in terms of Henry's law constant, $H = \frac{C}{p}$, where C stands for the gas concentration and p describes the equilibrium pressure at the specific (p, T) conditions. From the available literature, the solubility of He in molten PS¹⁸¹ at 461 K ($>T_g$) is $1.27 \cdot 10^{-8} \text{ mol} \cdot \text{kg}^{-1} \cdot \text{Pa}^{-1}$. Since in this work we use polystyrene in the glassy state, and therefore this data can only give a hint about the solubility of He gas in PS. From this work, we can conclude that He gas can be used as a model system to study the effect of elastic deformation by hydrostatic compression, excluding the influence of plasticization. At first glance, we may think that the vibrational frequencies f_{11} and f_{12} should increase with the He pressure due to hydrostatic compression (section 5.2 and the calculated trend in Figures 5.4 and 5.5). However, this concept fails when compared to the experimental results of all PS NPs displayed in Figures 5.4 and 5.5. Here, the frequencies of (1,1) and (1,2) modes at various p are normalized with the corresponding values at 1 bar and represented ($f(p)/f(1 \text{ bar})$) as a function of He p . The dashed lines in Figures 5.4 and 5.5 correspond to the expected trend of f_{11} and f_{12} assuming solely the effect of PS (nonlinear) stiffening due to hydrostatic compression (calculated in Section 2). The solid purple circles in Figure 5.4 represent the normalized frequency of the (1,1) mode in the forward direction of pressure change, whereas

the open circles correspond to the backward direction. The zero hysteresis for both modes confirm the assumption of poor solubility of He in PS and, thereby, reversibility of PS CCs after He treatment. However, the behavior of f_{11} and f_{12} with He p shows a size-dependent trend, as also described in Figure 5.3.

For PS143, the normalized f_{11} blueshifts while increasing p over the predicted (dashed line in Figure 5.4) trend due to the increase of particle contacts in addition to the stiffening of PS by hydrostatic compression. The same trend is being repeated for PS210. However, as the particle size increases, the normalized frequency of the (1,1) mode drops after about 200 bar. For example, in the case of PS556 (Figure 5.4d), the normalized $f_{11}(p)$ monotonically decreases with p after 200 bar, showing about 3% frequency redshift at 1000 bar and for PS610 CCs (Figure 5.4e), $f_{11}(p)$ reduces to about 6% of its initial value. This unusual behavior for the large-sized PS CCs (Figures 5.4c-f) may lead to the conclusion that there is some gas-induced phenomenon working against the increase of particle contacts and nonlinear stiffening caused by hydrostatic compression. Surprisingly, the reduced $f_{11}(p)$ for PS830 CC shows an irreversible trend before and after pressurization, i.e., $f_{11}(p)$ is permanently redshifted after depressurization, which may be due to the removal of inherent contact bridges formed by fabrication impurities.

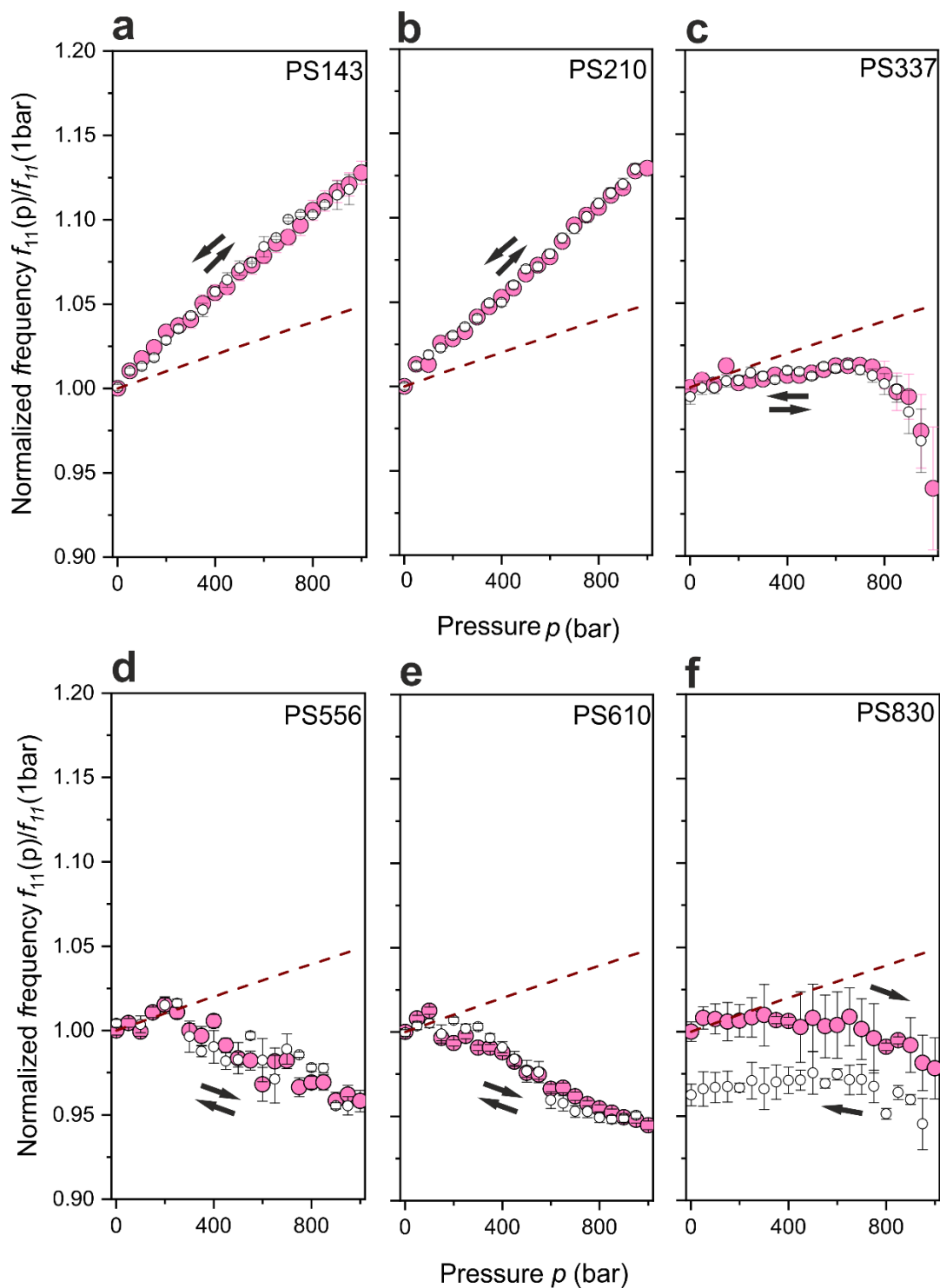


Figure 5.4: Normalized frequency of the dipolar (1,1) mode represented as a function of He pressure in the forward (solid pink circles) and backward (hollow white circles) direction of pressure change measured for (a) PS143 (b) PS210 (c) PS337 (d) PS556 (e) PS610 and (f) PS830 CC at RT. The red dashed lines represent the calculated f_{11} trend considering only the nonlinear stiffening of bulk polystyrene due to hydrostatic compression.

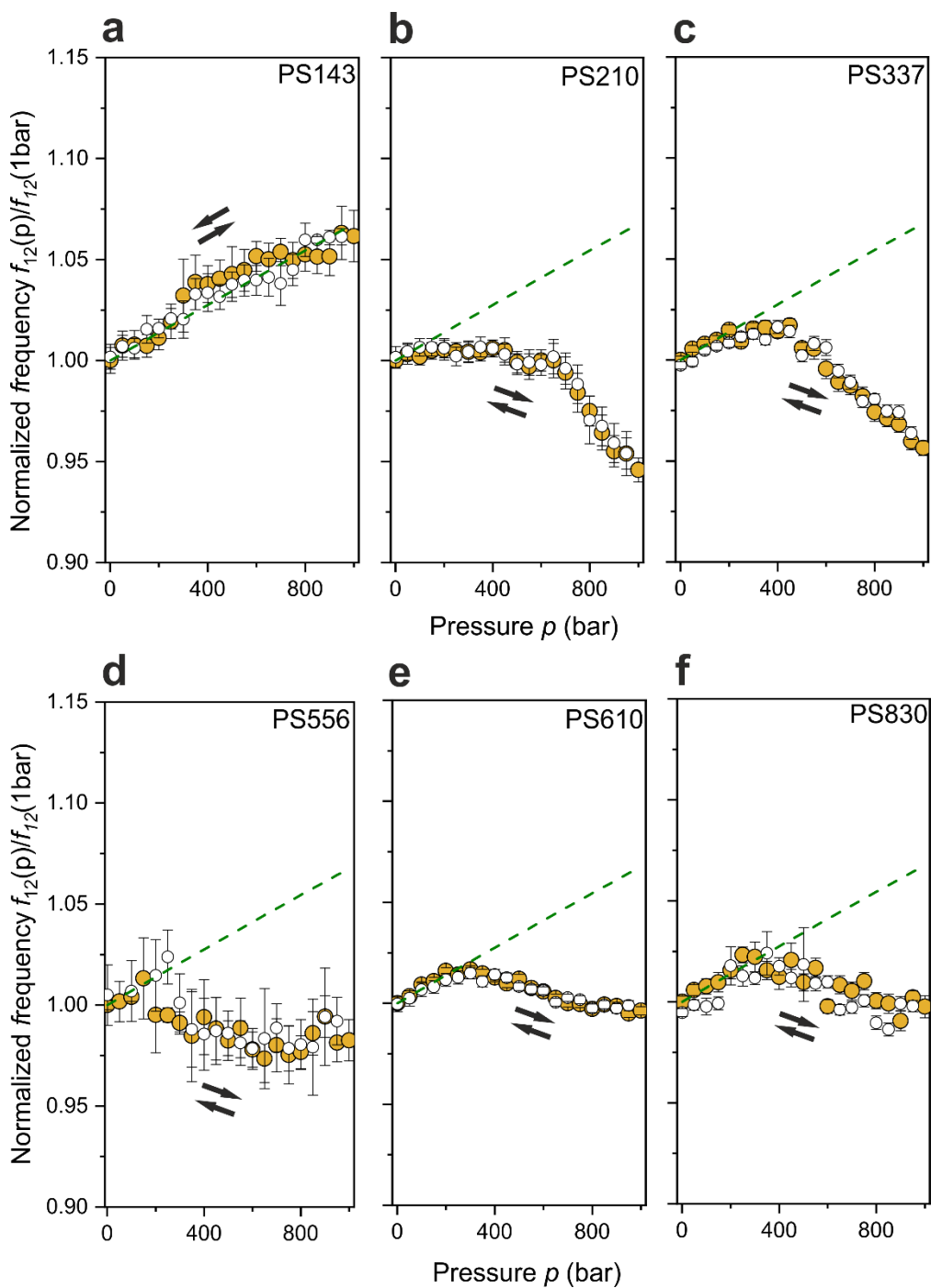


Figure 5.5: Normalized (and reduced) frequency of the quadrupolar (1,2) mode represented as a function of He pressure in the forward (solid yellow circles) and backward (hollow white circles) direction of pressure change measured for (a) PS143 (b) PS210 (c) PS337 (d) PS556 (e) PS610 and (f) PS830 CC at RT. The green dashed lines represent the calculated reduced f_{12} trend considering only the nonlinear stiffening of bulk polystyrene due to hydrostatic compression.

Now, let us consider the behavior of f_{12} upon He pressure treatment of CCs (Figure 5.5) to explain the drop of frequencies above 200 bar evident for PS210, PS337, PS556, PS610, and PS830 CCs. It is known that the acoustic energy localization of the quadrupolar mode depends on the elastic impedance contrast Z between NP and the surrounding environment^{110,149}. The observed frequency redshift of the dipolar (1,1) mode (Figure 5.4) also depends on the relative acoustic impedance $\frac{Z_{PS}}{Z_{He}}$ (Section 5.2) that controls the leakage of the acoustic energy at the fluid-solid interface and thereby determine the frequency shift of $f_{11}(p)$ and $f_{12}(p)$. The acoustic energy leakage increases with improving acoustic impedance matching between fluid and solid¹⁸², resulting in a redshift of the frequencies. The relative $\frac{Z_{PS}}{Z_{He}}$ drops from about $1.2 \cdot 10^4$ at 1 bar to $\frac{Z_{PS}}{Z_{He}} \cong 51$ at 250 bar (Figure 5.3a) implying strong increase of the acoustic energy leakage. The leakage becomes even more prominent at 1000 bar, with $\frac{Z_{PS}}{Z_{He}} \cong 14.5$, leading to a further decrease of f_{11} and f_{12} . Therefore, the redshift of frequencies is anticipated due to the leakage of acoustic energy from the particles to the voids of the PS CCs filled by the supercritical He. However, for PS143, the reduced f_{12} follows the theoretical trend (stiffening), suggesting acoustic leakage is negligibly small in the smaller NPs.

From the JKR model, the contact area radius follows $a_0 \propto d^{2/3}$ dependence (Section 3.3) and the contact radii for PS143 and PS610 CCs would be 8 nm and 21 nm (Table 3.2), respectively. Consequently, for the *fcc* lattice with 12 neighbors, the free surface of NPs would be reduced by 1% and 0.35% for PS143 and PS610 CCs. However, recalling the deviation of f_{11} from the JKR model prediction (Figure 4.4b), the presence of physical contacts created by intrinsic fabrication impurities¹⁷³ may further reduce the available free surface. Furthermore, the contact radii measured from SEM images for the as-prepared PS143 and PS610 samples are 31 nm and 59 nm, respectively, which may further reduce the free surface by 56% and 11%. Clearly, the reduction of the free surface is pronounced for smaller NPs. Moreover, a further increase of contacts during compression also reduces the free surface for PS143 CC. Therefore, we can assume that for PS143 CC, the acoustic energy leakage is absent, as shown in Figure 5.6. Conversely, for PS610, the relative reduction of the free surface by impurities is smaller than PS143 CC, and even after compression by hydrostatic pressure, the available free surface area is significantly larger for acoustic energy leakage. With the increase of pressure, the acoustic impedance contrast between PS and He lowers, which results in a significant drop of f_{11} and f_{12} . In general, the size-dependent

behavior of f_{11} occurs as a consequence of the three effects mentioned above - an increase of particle contacts due to hydrostatic compression, nonlinear stiffening of PS (dashed lines in Figures 5.4 and 5.5), and acoustic energy leakage depending on the NPs free surface area. In summary, He gas as a non-plasticizing medium produces negligible soldering of PS NPs in the CCs and is an excellent model medium to investigate the reversible gas-pressure-induced effects.

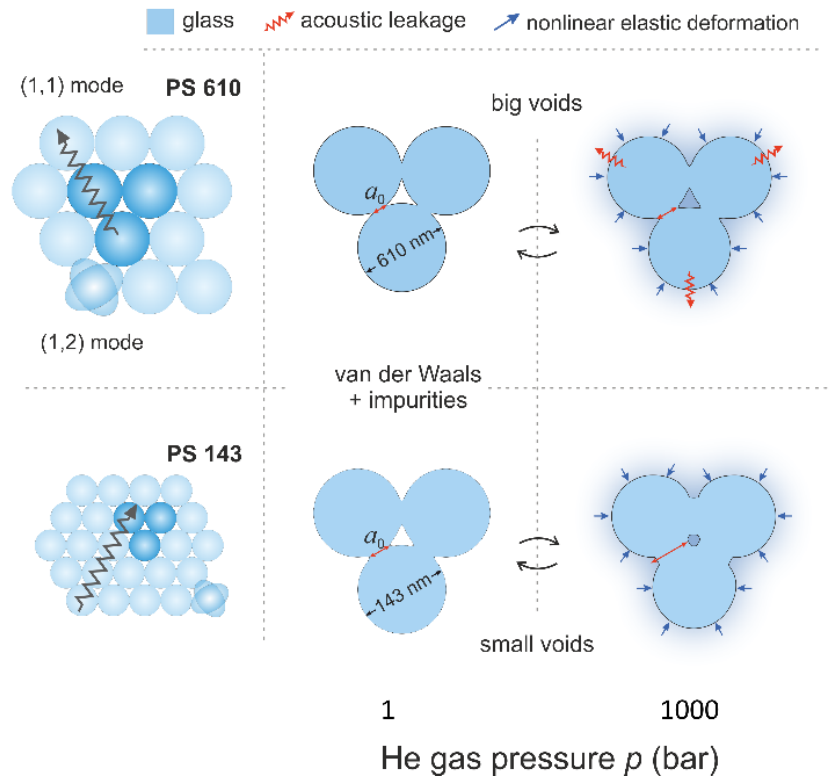


Figure 5.6: Scheme showing the response of PS143 and PS610 CCs at ambient conditions and when exposed to He pressure at 1000 bar ¹⁹.

Chapter 6

PS CCs in high-pressure Ar gas

Ar gas, in its supercritical state, is a good solvent for polystyrene¹⁸¹ ($H = 0.261 \cdot 10^{-5} \text{ mol g}^{-1} \text{ bar}^{-1}$ at 298K)¹⁸³, and hence it can plasticize PS NPs. The plasticization, along with the hydrostatic compression given by gas pressure, enhances the NP interparticle contacts, enabling permanent soldering of PS NPs¹. The application and optimization of this physical process require a thorough knowledge of several geometrical and thermodynamic parameters, including the optimum (p, T) conditions, NP size, solubility of the specific gas and time. In this section, we will quantitatively describe the optimum particle diameter for the nanoscale soldering of PS CCs by Ar gas pressure.

When mentioning different particle diameters, one of the important parameters to consider is the surface-to-volume (S/V) ratio of spherical NPs. For a single particle of radius R , the surface area to volume ratio can be given by:

$$\frac{S}{V} = \frac{4\pi R^2}{\frac{4}{3}\pi R^3} = \frac{3}{R} \quad (6.1)$$

A particle in an *fcc* crystal has 12 nearest neighbors. Assuming that it has an initial contact radius of a_0 with each neighboring particle and recalling the JKR model, we obtain:

$$a_0^{\text{JKR}} = \left(\frac{3\pi d^2 W}{8E_{\text{eff}}} \right)^{\frac{1}{3}} \quad (6.2)$$

The free surface-to-volume ratio can be given as:

$$\frac{S_f}{V} = \frac{4\pi R^2 - (12 \cdot 4\pi a_0^2)}{\frac{4}{3}\pi R^3} \quad (6.3)$$

Based on Eqs. 6.2 and 6.3, we can illustrate the free surface area to volume ratio for the particle diameter ranging from 100 nm to 900 nm, as shown in Figure 6.1a. As the particle size reduces to 100 nm, the free surface-to-volume ratio is considerably increased. Therefore, we can expect that the gas diffusion inside smaller particles will produce a much thicker plasticized shell than larger particles, as illustrated in scheme 6.1b, c. Following this concept, a qualitative expectation is that the soldering is most pronounced for the smallest NP.

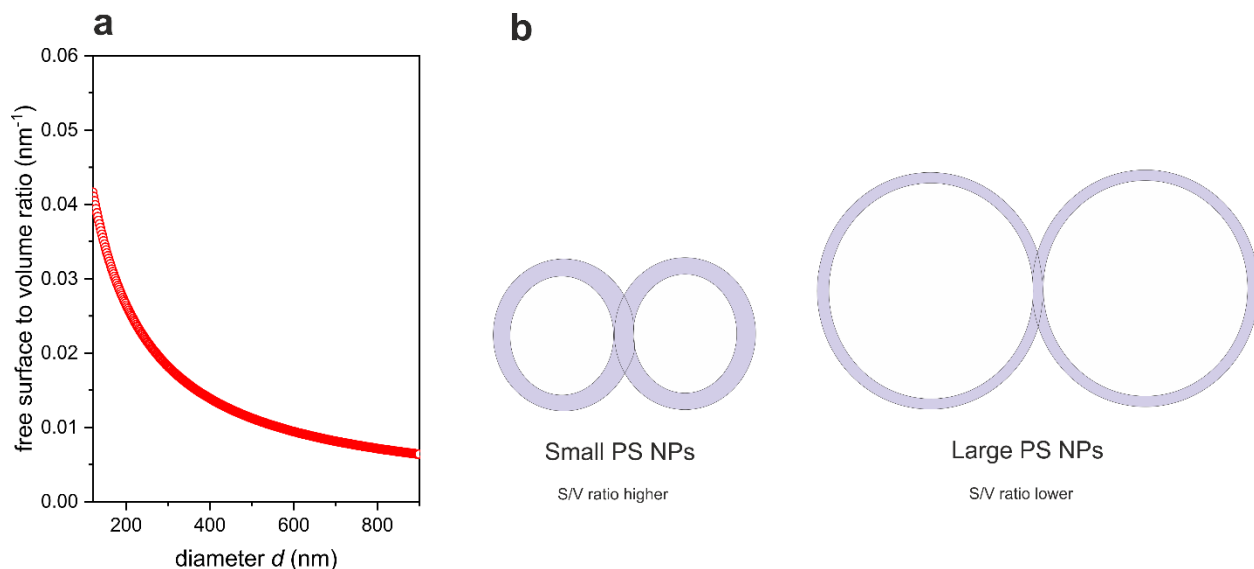


Figure 6.1: (a) Free surface area to volume ratio illustrated as a function of particle diameter calculated based on Eq. 6.2 and 6.3. (b) qualitative illustration of plasticized shells in smaller and bigger particle dimers.

6.1 BLS Experimental results

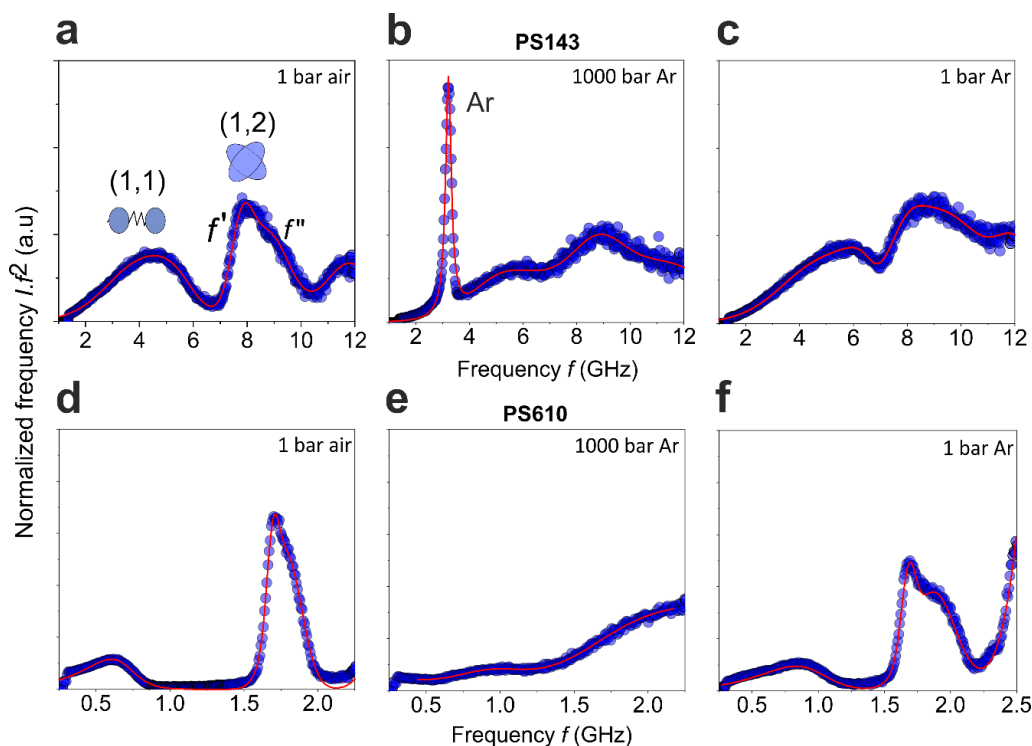


Figure 6.2: Normalized BLS spectra (anti-Stokes side) of PS CCs of diameter (a-c) $d = 143$ nm, PS143 and (d-f) $d = 610$ nm, PS610 obtained from Ar gas pressure-dependent measurements at RT. (a, d) as-prepared sample at 1 bar air (b, e) at 1000 bar Ar (c, f) post-treatment at 1 bar Ar.

As shown in Figure 6.2, we will consider the (1,1) and (1,2) modes of two different-sized CCs; PS143 and PS610, when exposed to Ar gas pressure. Notably, the peaks corresponding to the (1,1) and (1,2) modes are significantly blueshifted for both samples with respect to the spectra of pristine CCs. For the smaller-sized PS143, f_{11} increases from 4.57 GHz for the as-prepared sample at 1 bar air (Figure 6.2a) to 6.13 GHz (Figure 6.2 b) at 1000 bar Ar, producing 34% frequency blueshift. The intense sharp peak in Figure 6.2b overlapping with the peak corresponding to (1,1) mode represents the pressure wave propagating in the Ar, which was not sufficiently suppressed by the cross-polarized light geometry. Upon depressurization, f_{11} redshifts to 5.49 GHz (Figure 6.2c). This, when compared with the as-prepared sample, indicates an irreversible process with 20% blueshift. This behavior of f_{11} can be attributed to the increase of particle contacts caused by plastic deformation of the interface due to the combination of two effects: plasticization and hydrostatic compression. Similarly, for PS610 CCs, f_{11} increases from 0.61 GHz for the as-prepared sample at 1 bar air (Figure 6.2d) to 0.97 GHz at 1000 bar Ar (Figure 6.2e), indicating 59% frequency blueshift. After depressurization (Figure 6.2f), f_{11} shifts to 0.82 GHz, showing 34% permanent blueshift.

Now, considering the peak associated with the (1,2) mode, for PS143 CC, the reduced f_{12} increases from 6.85 GHz ($f' = 7.92$ GHz and $f'' = 8.98$ GHz) at 1 bar air (Figure 6.2a) to 7.55 GHz ($f' = 8.58$ and $f'' = 9.61$ GHz) at 1000 bar of Ar (Figure 6.2b), indicating 10% blueshift by pressurization. However, f_{12} shifts to 6.94 GHz ($f' = 7.98$ GHz and $f'' = 9.02$ GHz) after depressurization. The significant spectral split and blueshift of f' and f'' after Ar treatment indicate the permanent increase of particle contacts. For PS610 as-prepared sample, the reduced f_{12} is about 1.60 GHz ($f' = 1.69$ GHz and $f'' = 1.79$ GHz), as given in Figure 6.2d. However, the BLS spectrum at 1000 bar Ar is poorly resolved, as shown in Figure 6.2e. The apparent broadening of (1,2) mode can be explained as the mode delocalization occurring due to the acoustic/elastic energy leakage from the NPs to the surrounding medium. As explained in the previous section, the acoustic impedance contrast, $Z_{PS}/Z_{Ar} \cong 3$ at 1000 bar Ar, which is much more pronounced when compared to He atmosphere ($Z_{PS}/Z_{He} \cong 14.5$) at the same pressure. Additionally, as we found in the case of He treatment, the acoustic energy leakage becomes prominent while increasing the NP size, and therefore, the spectrum of PS610 (Figure 6.2e) is less resolved when compared to PS143 (Figure 6.2b) at 1000 bar Ar. After the pressure release, at 1 bar, peak resolution is much improved due to the lack of energy leakage, as shown in Figure 6.2f. Now, the reduced f_{12} is about 1.49

GHz, where $f' = 1.68$ GHz and $f'' = 1.88$ GHz. Again, the significant mode split and blueshift indicate the permanent increase of particle contacts after Ar pressure treatment. As it is evident that Ar gas pressure treatment results in an irreversible change in the BLS spectra of PS143 and PS610 CC, next we can discuss the pressure dependence of f_{11} in detail for all the PS CCs.

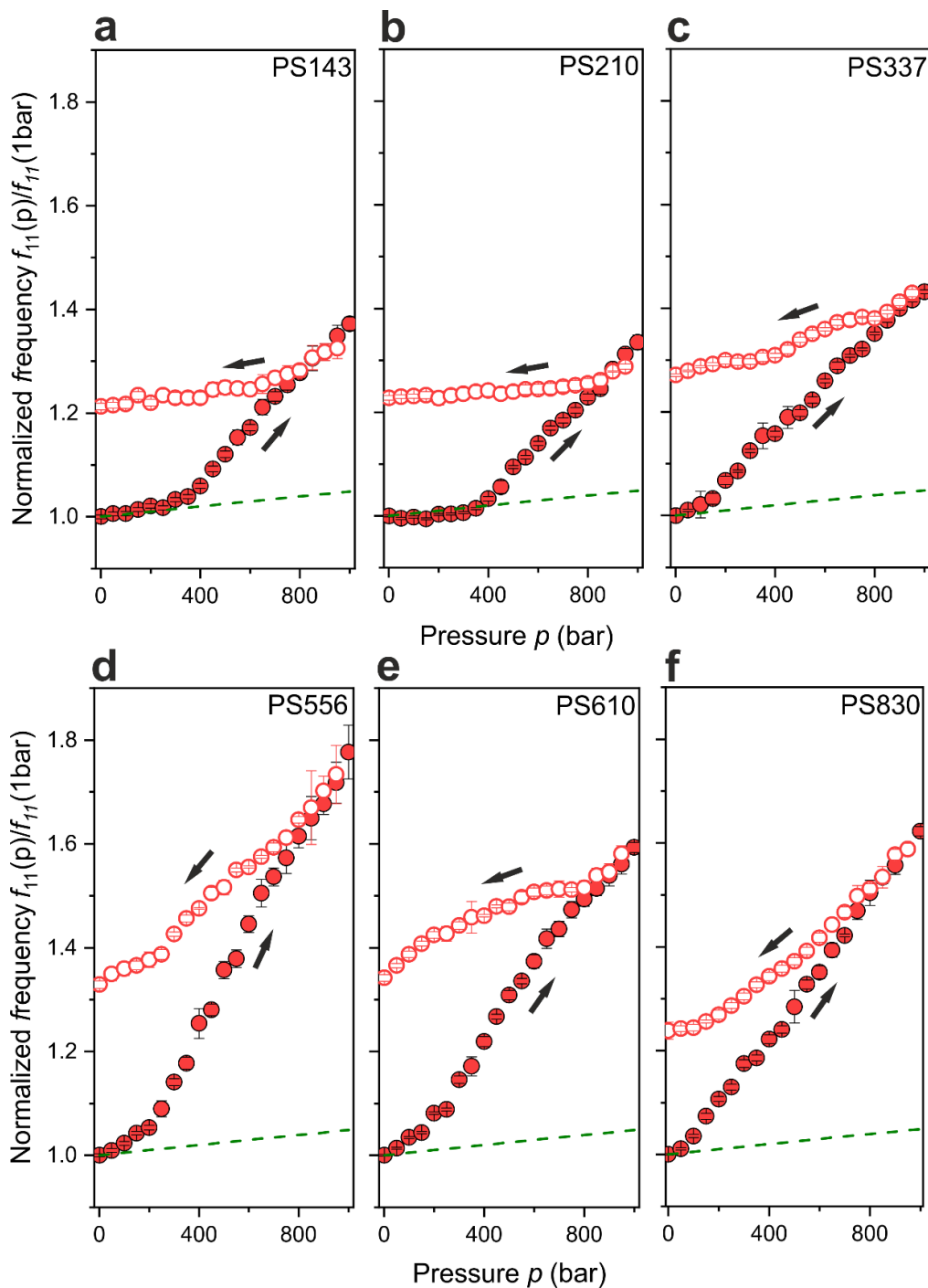


Figure 6.3: Normalized frequency of the dipolar (1,1) mode represented as a function of Ar pressure in the forward (solid red circles) and backward (hollow red circles) direction of pressure change measured for (a)

PS143 (b) PS210 (c) PS337 (d) PS556 (e) PS610 and (f) PS830 CC at RT. The green dashed lines represent the calculated f_{11} trend considering only the nonlinear stiffening of bulk polystyrene due to hydrostatic compression.

Figure 6.3 represents the behavior of f_{11} normalized by the corresponding frequency at 1 bar $f_{11}(p)/f_{11}(1 \text{ bar})$ for all PS CCs as a function of Ar gas pressure. The solid red circles denote the normalized f_{11} in the forward direction of pressure change, whereas the hollow red circles represent the f_{11} in the backward direction. The green dashed lines display the expected trend of f_{11} considering the effect of hydrostatic compression (nonlinear stiffening of PS, change of the contact area is not included), calculated based on the nonlinear theory of elasticity. As evident from Figure 6.3, all PS CCs after Ar treatment exhibit evident hysteresis in contrast to the results obtained from He pressure studies (Figure 5.4). For PS143 and PS210 CCs (Figures 6.3a and b), the normalized f_{11} follows the predicted trend up to about 300 bar, illustrating that a moderate blueshift (4%) of f_{11} occurs due to the nonlinear elastic stiffening of PS NPs by hydrostatic compression. However, for PS337, PS556, PS610 and PS830 CCs (Figures 6.3c-f), with the increase of pressure, the normalized f_{11} shows an abrupt blueshift above the predicted trend. This indicates the enhancement of interparticle contacts from the lower applied pressure (about 100 bar) due to the plastic deformation of PS NPs by plasticization and the nonlinear stiffening by hydrostatic compression, which overcomes the acoustic energy leakage. For further increase of pressure from 300 bar to 800 bar, the normalized f_{11} is monotonically increasing for all PS CCs, indicating further plasticization and soldering. As mentioned in the previous section of He gas treatment (Figure 5.4), for PS143 and PS210, we assume that the acoustic energy leakage is negligibly small. However, for all other PS CCs, the behavior of f_{11} represent the combined effect of all four phenomena – the increase of particle contacts by plasticization, increase of particle contact by hydrostatic compression, nonlinear stiffening, and acoustic energy leakage. The subsequent increase of pressure above 800 bar, results in the continuous increase of f_{11} for all PS CCs. Surprisingly, in the backward direction, from 1000 bar to 800 bar, all the PS CCs have zero hystereses, depicting a reversible change of f_{11} as observed after the He gas treatment. It suggests that the PS stiffening due to the hydrostatic compression takes over plasticization, as the diffusion of Ar in PS above 800 bar is kinetically arrested^{1,184}. The subsequent reduction of pressure below 800 bar shows a distinct response for the smaller (PS143 and PS210) and bigger (PS337, PS556, PS610 and PS830) sized PS CCs. The former samples (Figures 6.3a and b) exhibit a monotonous reduction of $f_{1,1}$ down to 1 bar. The corresponding trend resembles hydrostatic softening,

excluding acoustic leakage. However, plasticization and, hence, soldering are still ongoing. Parallel hydrostatic softening. For the latter samples (Figure 6.3c-f), the drop of $f_{1,1}$ shows a systematic weakening of soldering, considering the interplay between plastic deformation, nonlinear stiffening, and acoustic leakage.

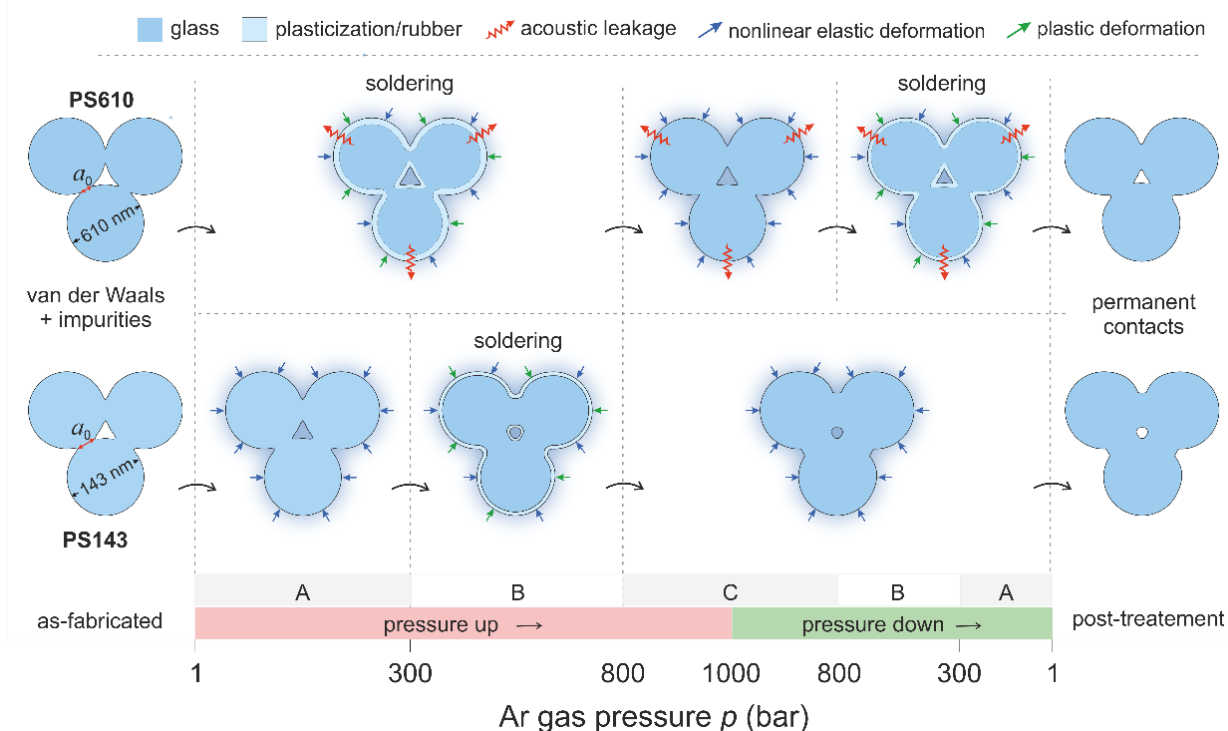


Figure 6.4: Scheme showing the response of PS143 and PS610 CC to Ar gas pressure in different pressure regimes; 1 bar to ~ 300 bar in region A, 300 bar to ~ 800 bar in region B and 800 bar to 1000 bar in region C, in the forward and backward direction of pressure change based on the experimental results shown in Figure 6.2. Reproduced from ref. ¹⁹.

To summarize the discussion of the pressure dependence of $f_{1,1}$, we can use the scheme in Figure 6.4 describing the interfacial effects in PS143 and PS610 CCs in response to the applied Ar pressure. The as-fabricated CCs in the glassy state have weak contacts formed by van der Waals interactions and contacts made out of fabrication impurities. For PS143 (lower panel in Figure 6.4), in region A (from 1 bar to ~ 300 bar), an increase of particle contacts occurs due to nonlinear elastic deformation. When the pressure increases in region B (from ~ 300 bar to ~ 800 bar), plasticization gets pronounced, improving the particle contacts and thus reducing the interparticle voids. However, plasticization is absent above 800 bar in region C, as the gas diffusion is suppressed. Nevertheless, the further increase in particle contacts results from the nonlinear elastic

deformation due to hydrostatic compression while increasing the pressure. Decreasing the pressure to 1 bar (regions B and A) reverts the nonlinear elastic deformation, but plasticization continues. Notably, the post-treated PS143 shows much reduced void volume compared to the as-fabricated sample. For PS610 (upper panel in Figure 6.4), plastic deformation and nonlinear elastic deformation start even from the lower pressures (~ 100 bar), thus increasing the particle contacts. Clearly, PS610 has a much higher free volume compared to PS143, and therefore, acoustic leakage comes into play as the pressure increases. Therefore the normalized f_{11} shows the resultant nature of all four phenomena. As mentioned before, above 800 bar in region C, the plastic deformation is absent. However, the conflicting trend of elastic deformation and acoustic energy leakage determines f_{11} . On decreasing the pressure below 800 bar, soldering weakens systematically as hydrostatic compression drops, but plastic deformation and acoustic leakage exist. The post-treated PS610, has a much lower void, or in other words, much-improved particle contacts than the as-fabricated structure. Figure 6.5 displays the SEM images of all the PS CCs before and after the Ar pressure treatment at 800 bar.

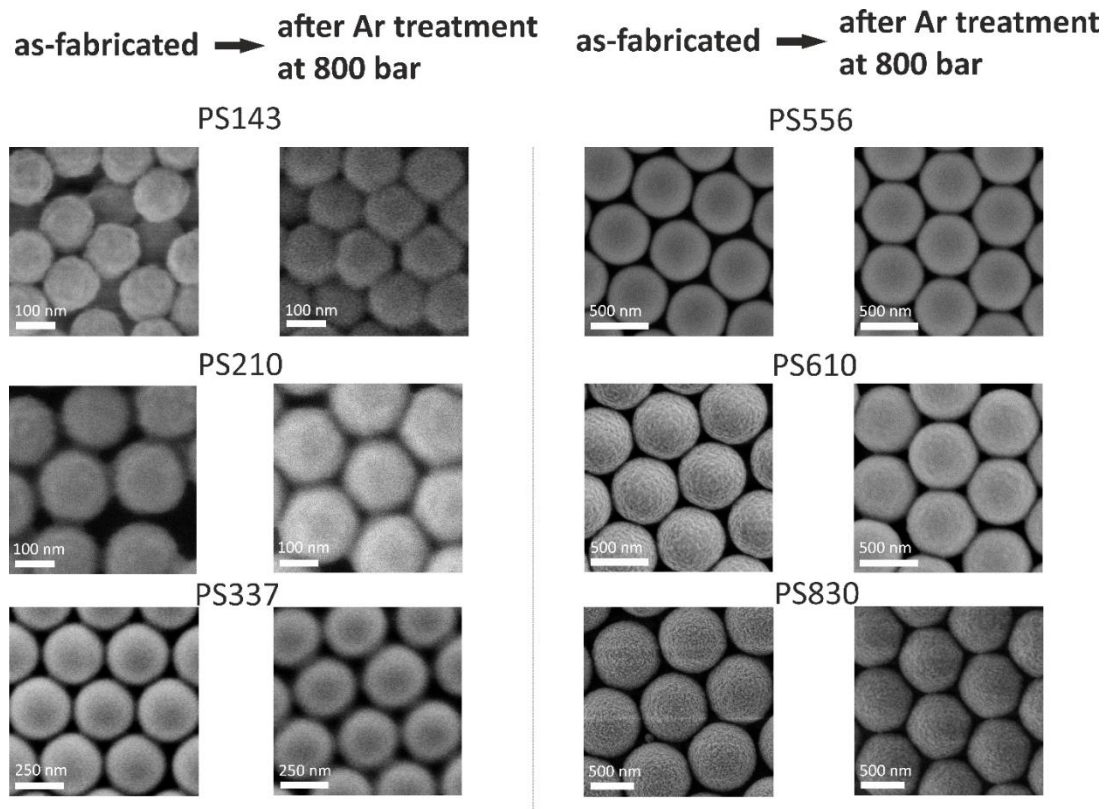


Figure 6.5: SEM images of PS monolayer deposited on Si wafer substrate before and after the Ar pressure treatment at 800 bar. Reproduced from ref. ¹⁹.

Chapter 7

PS CCs in high-pressure N₂ gas

In this section, we discuss the gas-specificity and size dependence of nano-scale soldering of PS CCs exposed to nitrogen gas pressure. As supercritical nitrogen is also a good solvent for polystyrene ($H = 0.087 \cdot 10^{-5} \text{ mol g}^{-1} \text{ bar}^{-1}$ at 298 K ($< T_g$))^{1,183}, it can plasticize the PS NPs and induce the mechanical reinforcement of particles.

7.1 BLS experimental results

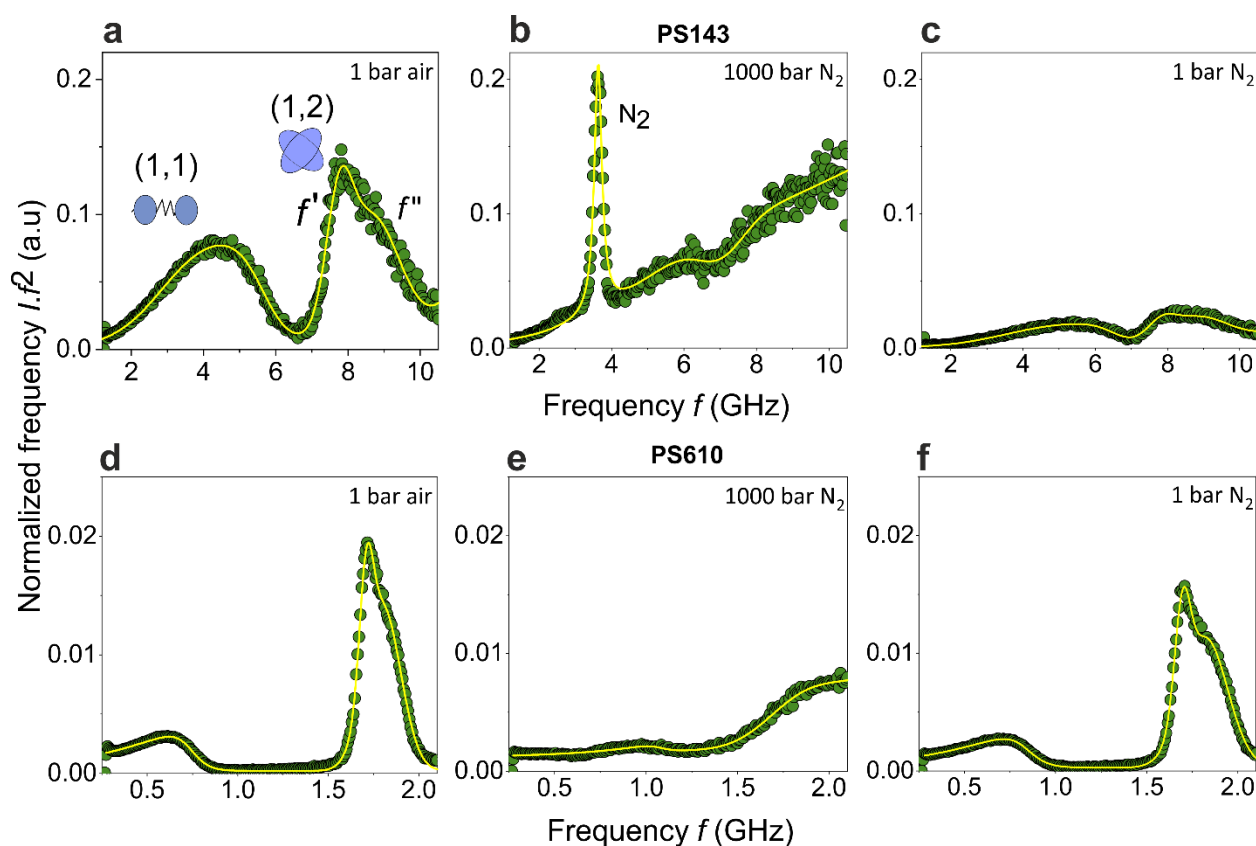


Figure 7.1: Normalized BLS spectra (anti-Stokes side) of PS CCs of diameter (a-c) $d = 143$ nm, PS143 and (d-f) $d = 610$ nm, PS610 obtained from N₂ gas pressure-dependent measurements at RT. (a, d) as-prepared sample at 1 bar air (b, e) at 1000 bar N₂ (c, f) post-treatment at 1 bar N₂.

At first, we consider the (1,1) and (1,2) modes of two different-sized CCs; PS143 and PS610, when exposed to N₂ gas pressure at RT. For PS143, f_{11} increases from 4.58 GHz for the as-prepared sample at 1 bar air (Figure 7.1a) to 6.17 GHz (Figure 7.1b) at 1000 bar of N₂, producing 35%

frequency blueshift. However, it returns to 4.99 GHz (Figure 7.1c) after the pressure release to 1 bar, producing 9% frequency blue shift. Similar to Ar case, the peak corresponding to the pressure wave in supercritical N₂ at 1000 bar (Figure 7.1b) is intense and overlaps with the (1,1) mode peak of PS143 CC. For PS610 CCs, f_{11} increases from 0.60 GHz for the as-prepared sample at 1 bar air (Figure 7.1d) to 0.98 GHz at 1000 bar N₂ (Figure 7.1e), indicating 63% frequency blueshift. After depressurization (Figure 7.1f), f_{11} redshifts to 0.73 GHz, showing 22% permanent blueshift concerning the as-prepared sample.

Now, considering the peak associated with the (1,2) mode; for PS143 CC, the reduced f_{12} is at 6.83 GHz ($f' = 7.79$ GHz and $f'' = 8.75$ GHz) at 1 bar air (Figure 7.1a). The spectrum is less resolved at 1000 bar N₂ (Figure 7.1b) due to the presence of an intense nitrogen pressure wave peak and the acoustic impedance matching between PS and N₂ at 1000 bar ($Z_{PS}/Z_{N_2} \cong 4.67$). After depressurization (Figure 7.1c), the reduced f_{12} is obtained at 6.82 GHz ($f' = 7.92$ GHz and $f'' = 9.03$ GHz). Since the reduced f_{12} gives the frequency of the quadrupolar mode of an interaction-free particle, the value remains the same before and after pressurization. However, the significant spectral split and blueshift, indicated by f' and f'' , confirm the enhancement of particle contacts. For PS610 as-prepared sample, the reduced f_{12} is about 1.62 GHz ($f' = 1.70$ GHz and $f'' = 1.80$ GHz), as given in Figure 7.1d. Similar to PS143 CC, the BLS spectrum at 1000 bar N₂ is poorly resolved, as shown in Figure 7.1e. The apparent broadening of the (1,2) mode peak can be explained as the mode delocalization occurring due to the acoustic energy leakage from the NPs to the surrounding medium. As mentioned in the He study, acoustic energy leakage becomes prominent with the NP size, and therefore the spectrum of PS610 (Figure 7.1e) is less resolved when compared to PS143 (Figure 7.1b) at 1000 bar N₂. After the pressure release, at 1 bar, the peak resolution is much improved due to the lack of acoustic energy leakage, as shown in Figure 7.1f. The reduced f_{12} is about 1.57 GHz, where $f' = 1.69$ GHz and $f'' = 1.82$ GHz. Clearly, N₂ gas pressure treatment also results in an irreversible change in the BLS spectra of PS143 and PS610 CC, and in the next section, we discuss the pressure dependence of f_{11} in detail for all the PS CCs exposed to N₂ gas pressure.

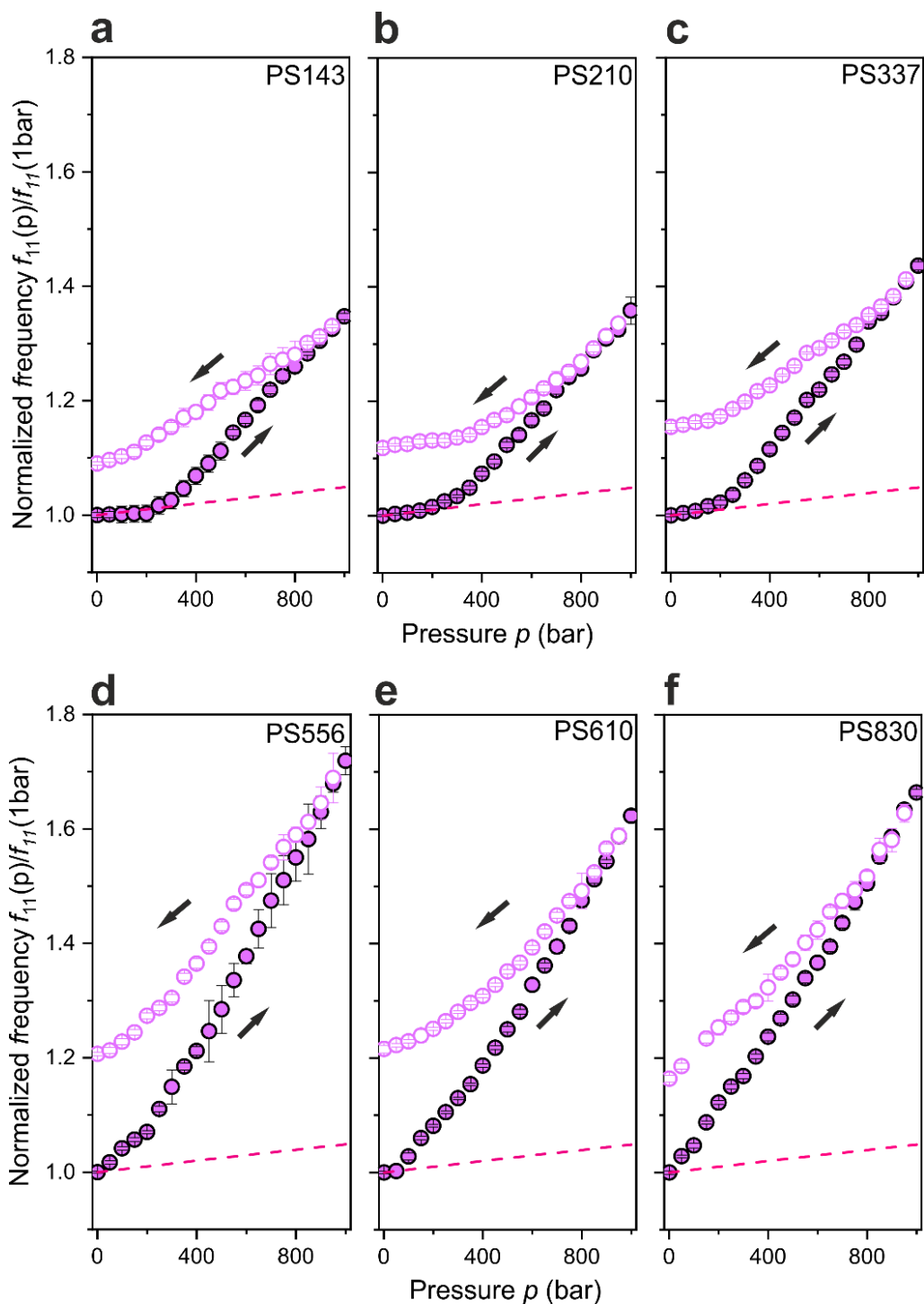


Figure 7.2: Normalized frequency of the dipolar (1,1) mode represented as a function of N_2 pressure in the forward (solid purple circles) and backward (hollow purple circles) direction of pressure change measured for (a) PS143 (b) PS210 (c) PS337 (d) PS556 (e) PS610 and (f) PS830 CCs at RT. The pink dashed lines represent the calculated f_{11} trend considering only the nonlinear stiffening of bulk polystyrene due to hydrostatic compression.

As shown in the previous sections, we can represent f_{11} normalized by the corresponding frequency at 1 bar $f_{11}(p)/f_{11}(1 \text{ bar})$ for all PS CCs as a function of N_2 gas pressure. In Figure 7.2, the solid purple circles denote the normalized f_{11} in the forward direction of pressure change, whereas the purple hollow circles represent the f_{11} in the backward direction. The pink dashed lines in each figure show the calculated trend of normalized f_{11} considering the effect of hydrostatic compression solely (no change of the contact area) based on the nonlinear theory of elasticity. As evident from Figure 7.2, all the PS CCs exhibit hysteresis, which shows the permanent change of PS CCs after N_2 treatment. For PS143, PS210 and PS337 CCs, the normalized f_{11} follows the calculated trend up to about 250 bar (Figure 7.2a-c). For PS 556, PS610 and PS830 CCs, the normalized f_{11} blueshifts abruptly from about 50 bar (Figure 7.2d-f) over the predicted trend. This indicates the increase of particle contacts due to the plasticization of PS CCs by gas diffusion, which, in addition to the nonlinear stiffening of PS, overcomes the acoustic energy leakage effect. Further increase of pressure above 300 bar monotonically blueshift the normalized f_{11} of all PS CCs, indicating the increased plasticization and soldering of PS NPs. As stated in the Ar gas study, the behavior of normalized f_{11} illustrates the competition between all four effects: the increase of contact by plasticization, an increase of contacts by hydrostatic compression, nonlinear stiffening, and acoustic energy leakage. Similar to the PS CCs exposed to Ar gas pressure, on decreasing the pressure from 1000 bar to 700 bar, the normalized f_{11} follows a reversible path. Here, the N_2 gas diffusion in PS is kinetically arrested^{1,184} in this regime, and therefore, hydrostatic elastic compression takes over the plasticization. On decreasing the pressure below 700 bar, the normalized f_{11} monotonically reduces up to about 250 bar for PS143, PS210, and PS337 CCs. In this regime, plasticization is still ongoing. However, the pressure-induced stiffening is reduced. For bigger particles such as PS556, PS610 and PS830 CCs, the normalized f_{11} shows a systematic weakening up to about 1 bar, indicating the combined effect of reduced plasticization, nonlinear stiffening, and acoustic energy leakage.

7.2 Size-dependence of nano-scale soldering of PS CCs with different supercritical gases

As our primary objective is to identify the size dependence of nanoscale soldering of PS CCs with different supercritical gases, we can illustrate the ratio of effective elastic modulus before and after the gas pressure treatments. As evident from Figure 7.3, He gas pressure treatment produces negligible soldering for the PS CCs, and therefore the C_{eff} value (Eqn. 3.10, section 3.3) remains the same as the as-prepared sample. However, after Ar and N_2 gas treatments, there is a non-

monotonic size-dependent trend, which is against the qualitative expectation of stronger soldering for smaller NPs. It is clear that from PS830 to PS610 CCs, soldering effectively improves as the NPs diameter reduces and the surface-to-volume ratio of an individual NP increases. However, the relative change of the modulus is the highest for the medium-sized particles ($d = 610$ nm), after which the ratio of effective elastic modulus considerably reduces while decreasing d . For the smallest-sized NPs (PS143), the role of initial contact bridges formed out of the fabrication impurities reduces the free surface and hence suppresses the gas diffusion and plasticization. Recall that the acoustic energy leakage is absent in PS143 because of the reduced interparticle voids, thereby free surface, occurring due to the contacts formed by fabrication impurities. For bigger particles such as PS610, the contact bridges formed out of fabrication impurities have a minor effect compared to smaller NPs. Even though the free surface is reduced with the impurity contacts, a comparatively higher free space for plasticization still exists. Notice that both Ar and N₂ gas pressure treatments have a similar size-dependent trend. However, as supercritical Ar is a better plasticizer than supercritical N₂, the ratio of effective elastic modulus is lower for PS CCs exposed to N₂ gas pressure.

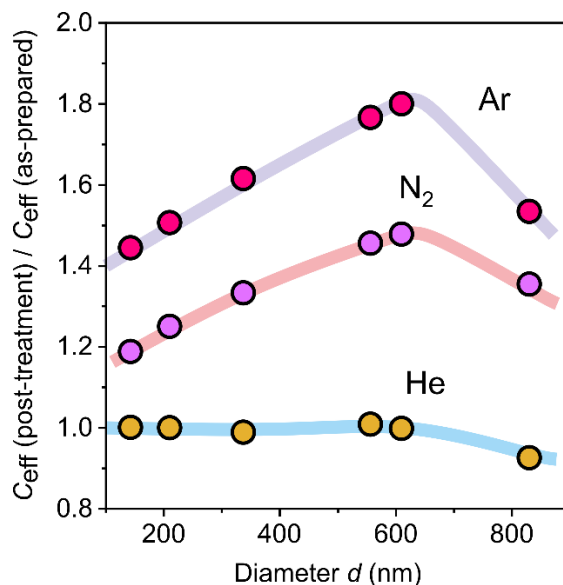


Figure 7.3: Relative change of the effective elastic modulus after He, N₂, and Ar pressure treatments of PS CCs as a function of particle diameter (d). The shaded lines represent the guide to the eye.

Conclusion and outlook

This thesis highlights the experimental investigation of the mechanical reinforcement of polystyrene colloidal crystals by exposure to supercritical fluids at room temperature. By employing Brillouin light scattering as a non-contact and nondestructive optical technique, we measured in situ the acoustic vibrations of CCs under the pressure changes. From this study, we are able to quantify the effect of nanoparticle size and gas specificity that favors the efficient soldering of CCs.

In Chapter 3, I discussed the synthesis of PS NPs by surfactant-free emulsion polymerization and the fabrication of PS CC samples for BLS and SEM studies. We investigated 6 PS CC samples with NP size ranging from 143 nm to 810 nm. For BLS measurements, 3D PS CC samples were prepared by drop casting, whereas for SEM studies, 2D monolayer samples were prepared on the air-water interface. The initial characterization of the pristine samples by BLS and SEM gave information about the particle diameter and the effective elastic modulus. The BLS measurement of pristine samples can accurately measure the particle diameter, which is in good agreement with the SEM data.

In Chapter 4, I discussed the acoustic properties of He, N₂, and Ar gasses measured at various pressures using BLS. The refractive index (n), longitudinal sound velocity (v_1) and acoustic impedance (Z) values of the gasses were determined for pressures ranging from 1 bar to 1000 bar. The above results were applied in the further analysis of CCs exposed to supercritical fluids.

In Chapter 5, I discussed the pressure-dependent BLS experiments performed when PS CCs are exposed to He gas pressure. At first, I represented the theoretical pressure dependence of vibrational frequencies based on the nonlinear theory of elasticity. The ratio of acoustic impedances between PS and the gas is illustrated for pressures from 1 bar to 1000 bar. The BLS and SEM results lead to the conclusion that He gas does not produce soldering in PS CCs. He gas is poorly soluble in polystyrene, and hence, the effect of plasticization can be excluded. Although He treatment is reversible and soldering-free, we can establish a model system to evaluate the effect of hydrostatic pressure on CCs. The vibration spectra of CCs exposed to He pressure originate from the competing effects of nonlinear elastic deformation, increase of particle contacts by compression, and acoustic energy leakage from the NPs to gas. We observed a size-dependent behavior in the crystal's spectral response to He pressure. Notably, the larger free surface of larger

nanoparticles makes the acoustic leakage more effective. Additionally, the acoustic impedance contrast increases with pressure, making the acoustic leakage more obvious at higher pressures.

Since Ar and N₂ gases are good solvents for PS, the exposure of PS CCs to these gases results in the plasticization of PS NPs. PS CCs exposed to supercritical Ar (Chapter 6) and N₂ (Chapter 7) can produce efficient soldering to all the NPs studied. On illustrating the size-dependence of nano-scale soldering of PS CCs, we can conclude that soldering turned out to be efficient for mid-sized NPs (diameter ~ 610 nm). The effective elastic modulus of the CCs exposed to supercritical Ar improved by over 90% compared to the pristine sample. The monotonic size-dependent behavior can be related to the fabrication impurities that contribute to impurity-based solid contacts, in addition to the van der Waals adhesive forces. The creation of solid bridges in three-dimensional colloidal crystals¹⁷³ and the quality of monolayers constructed of polystyrene spheres²³ have both been observed to be impacted by impurities. However, these native interparticle bonds are insufficiently strong to resolve the problem of colloidal crystal brittleness. They also lessen the free surface that is open to plasticization or other surface-mediated treatments. Since this effect is more pronounced for smaller particles, soldering becomes less effective as nanoparticle size decreases.

This research opens up new avenues for the controllable mechanical engineering of two- and three-dimensional architectures based on polymer colloidal crystals. These architectures can be engineered using variables that can be changed, such as nanoparticle geometry and composition, thermodynamic variables (pressure, temperature), solubility, and time. Additionally, we hope that this study may inspire theoretical and experimental work that creates large-scale robust colloidal crystals using various polymers and gases, such as supercritical CO₂¹⁸⁵ or Xe¹⁸⁶, for novel applications in coatings, photonics, and phononics^{79,94}.

References:

- (1) Babacic, V.; Varghese, J.; Coy, E.; Kang, E.; Pochylski, M.; Gapinski, J.; Fytas, G.; Graczykowski, B. Mechanical Reinforcement of Polymer Colloidal Crystals by Supercritical Fluids. *J. Colloid Interface Sci.* **2020**, *579*, 786–793. <https://doi.org/10.1016/j.jcis.2020.06.104>.
- (2) Hailin Cong; Yu, B.; Tang, J.; Li, Z.; Liu, X. Current Status and Future Developments in Preparation and Application of Colloidal Crystals. *Chem. Soc. Rev.* **2013**, *42* (19), 7774. <https://doi.org/10.1039/c3cs60078e>.
- (3) Vogel, N.; Retsch, M.; Fustin, C.-A.; del Campo, A.; Jonas, U. Advances in Colloidal Assembly: The Design of Structure and Hierarchy in Two and Three Dimensions. *Chem. Rev.* **2015**, *115* (13), 6265–6311. <https://doi.org/10.1021/cr400081d>.
- (4) Van Dommelen, R.; Fanzio, P.; Sasso, L. Surface Self-Assembly of Colloidal Crystals for Micro- and Nano-Patterning. *Adv. Colloid Interface Sci.* **2018**, *251*, 97–114. <https://doi.org/10.1016/j.cis.2017.10.007>.
- (5) Still, T.; Cheng, W.; Retsch, M.; Jonas, U.; Fytas, G. Colloidal Systems: A Promising Material Class for Tailoring Sound Propagation at High Frequencies. *J. Phys. Condens. Matter* **2008**, *20* (40), 404203. <https://doi.org/10.1088/0953-8984/20/40/404203>.
- (6) Davis, K. E.; Russel, W. B.; Glantschnig, W. J. Disorder-to-Order Transition in Settling Suspensions of Colloidal Silica: X-Ray Measurements. *Science* **1989**, *245* (4917), 507–510. <https://doi.org/10.1126/science.245.4917.507>.
- (7) Trau, M.; Saville, D. A.; Aksay, I. A. Field-Induced Layering of Colloidal Crystals. *Science* **1996**, *272* (5262), 706–709. <https://doi.org/10.1126/science.272.5262.706>.
- (8) Jiang, P.; Bertone, J. F.; Hwang, K. S.; Colvin, V. L. Single-Crystal Colloidal Multilayers of Controlled Thickness. *Chem. Mater.* **1999**, *11* (8), 2132–2140. <https://doi.org/10.1021/cm990080+>.
- (9) Deimling, M.; Kousik, S. R.; Abitaev, K.; Frey, W.; Sottmann, T.; Koynov, K.; Laschat, S.; Atanasova, P. Hierarchical Silica Inverse Opals as a Catalyst Support for Asymmetric Molecular Heterogeneous Catalysis with Chiral Rh-diene Complexes. *ChemCatChem* **2021**, *13* (9), 2242–2252. <https://doi.org/10.1002/cctc.202001997>.
- (10) Yoshimura, H. Two-Dimensional Crystals of Apoferritin. *Adv. Biophys.* **1997**, *34*, 93–107. [https://doi.org/10.1016/S0065-227X\(97\)89634-7](https://doi.org/10.1016/S0065-227X(97)89634-7).
- (11) Cong, H.; Cao, W. Array Patterns of Binary Colloidal Crystals. *J. Phys. Chem. B* **2005**, *109* (5), 1695–1698. <https://doi.org/10.1021/jp048269i>.
- (12) Imhof, A.; Pine, D. J. Ordered Macroporous Materials by Emulsion Templating. *Nature* **1997**, *389* (6654), 948–951. <https://doi.org/10.1038/40105>.
- (13) Liang, X.; Dong, R.; Ho, J. C. Self-Assembly of Colloidal Spheres toward Fabrication of Hierarchical and Periodic Nanostructures for Technological Applications. *Adv. Mater. Technol.* **2019**, *4* (3), 1800541. <https://doi.org/10.1002/admt.201800541>.
- (14) Still, T.; Sainidou, R.; Retsch, M.; Jonas, U.; Spahn, P.; Hellmann, G. P.; Fytas, G. The “Music” of Core–Shell Spheres and Hollow Capsules: Influence of the Architecture on the Mechanical Properties at the Nanoscale. *Nano Lett.* **2008**, *8* (10), 3194–3199. <https://doi.org/10.1021/nl801500n>.
- (15) Tao, A. R.; Huang, J.; Yang, P. Langmuir–Blodgett of Nanocrystals and Nanowires. *Acc. Chem. Res.* **2008**, *41* (12), 1662–1673. <https://doi.org/10.1021/ar8000525>.
- (16) Cong, H.; Cao, W. Colloidal Crystallization Induced by Capillary Force. *Langmuir* **2003**, *19* (20), 8177–8181. <https://doi.org/10.1021/la0344480>.
- (17) Yamamoto, E.; Mori, S.; Shimojima, A.; Wada, H.; Kuroda, K. Fabrication of Colloidal Crystals Composed of Pore-Expanded Mesoporous Silica Nanoparticles Prepared by a Controlled Growth Method. *Nanoscale* **2017**, *9* (7), 2464–2470. <https://doi.org/10.1039/C6NR07416B>.

- (18) Morphew, D.; Shaw, J.; Avins, C.; Chakrabarti, D. Programming Hierarchical Self-Assembly of Patchy Particles into Colloidal Crystals *via* Colloidal Molecules. *ACS Nano* **2018**, *12* (3), 2355–2364. <https://doi.org/10.1021/acsnano.7b07633>.
- (19) Varghese, J.; Mohammadi, R.; Pochylski, M.; Babacic, V.; Gapinski, J.; Vogel, N.; Butt, H.-J.; Fytas, G.; Graczykowski, B. Size-Dependent Nanoscale Soldering of Polystyrene Colloidal Crystals by Supercritical Fluids. *J. Colloid Interface Sci.* **2023**, *633*, 314–322. <https://doi.org/10.1016/j.jcis.2022.11.090>.
- (20) Dimitrov, A. S.; Nagayama, K. Continuous Convective Assembling of Fine Particles into Two-Dimensional Arrays on Solid Surfaces. *Langmuir* **1996**, *12* (5), 1303–1311. <https://doi.org/10.1021/la9502251>.
- (21) Li, Q.; Retsch, M.; Wang, J.; Knoll, W.; Jonas, U. Porous Networks Through Colloidal Templates. In *Templates in Chemistry III*; Broekmann, P., Dötz, K.-H., Schalley, C. A., Eds.; Topics in Current Chemistry; Springer Berlin Heidelberg: Berlin, Heidelberg, 2008; Vol. 287, pp 135–180. https://doi.org/10.1007/128_2008_3.
- (22) Still, T. *High Frequency Acoustics in Colloid-Based Meso- and Nanostructures by Spontaneous Brillouin Light Scattering*; Springer Theses; Springer Berlin Heidelberg: Berlin, Heidelberg, 2010. <https://doi.org/10.1007/978-3-642-13483-8>.
- (23) Rey, M.; Yu, T.; Guenther, R.; Bley, K.; Vogel, N. A Dirty Story: Improving Colloidal Monolayer Formation by Understanding the Effect of Impurities at the Air/Water Interface. *Langmuir* **2019**, *35* (1), 95–103. <https://doi.org/10.1021/acs.langmuir.8b02605>.
- (24) Lotito, V.; Zambelli, T. Approaches to Self-Assembly of Colloidal Monolayers: A Guide for Nanotechnologists. *Adv. Colloid Interface Sci.* **2017**, *246*, 217–274. <https://doi.org/10.1016/j.cis.2017.04.003>.
- (25) Vogel, N.; Weiss, C. K.; Landfester, K. From Soft to Hard: The Generation of Functional and Complex Colloidal Monolayers for Nanolithography. *Soft Matter* **2012**, *8* (15), 4044–4061. <https://doi.org/10.1039/C1SM06650A>.
- (26) Haynes, C. L.; Van Duyne, R. P. Nanosphere Lithography: A Versatile Nanofabrication Tool for Studies of Size-Dependent Nanoparticle Optics. *J. Phys. Chem. B* **2001**, *105* (24), 5599–5611. <https://doi.org/10.1021/jp010657m>.
- (27) Mihi, A.; Ocaña, M.; Míguez, H. Oriented Colloidal-Crystal Thin Films by Spin-Coating Microspheres Dispersed in Volatile Media. *Adv. Mater.* **2006**, *18* (17), 2244–2249. <https://doi.org/10.1002/adma.200600555>.
- (28) Park, S. H.; Qin, D.; Xia, Y. Crystallization of Mesoscale Particles over Large Areas. *Adv. Mater.* **1998**, *10*, 1028–1032.
- (29) Chen, K. M.; Jiang, X.; Kimerling, L. C.; Hammond, P. T. Selective Self-Organization of Colloids on Patterned Polyelectrolyte Templates. *Langmuir* **2000**, *16* (20), 7825–7834. <https://doi.org/10.1021/la000277c>.
- (30) Vogel, N.; Goerres, S.; Landfester, K.; Weiss, C. K. A Convenient Method to Produce Close- and Non-Close-Packed Monolayers Using Direct Assembly at the Air-Water Interface and Subsequent Plasma-Induced Size Reduction. *Macromol. Chem. Phys.* **2011**, *212* (16), 1719–1734. <https://doi.org/10.1002/macp.201100187>.
- (31) Ye, X.; Huang, J.; Zeng, Y.; Sun, L.-X.; Geng, F.; Liu, H.-J.; Wang, F.-R.; Jiang, X.-D.; Wu, W.-D.; Zheng, W.-G. Monolayer Colloidal Crystals by Modified Air-Water Interface Self-Assembly Approach. *Nanomaterials* **2017**, *7* (10), 291. <https://doi.org/10.3390/nano7100291>.
- (32) Kaneko, A. Surface Micro-/Nanostructuring Using Self-Assembly of Fine Particles. In *Microbial Toxins*; Gopalakrishnakone, P., Stiles, B., Alape-Girón, A., Dubreuil, J. D., Mandal, M., Eds.; Toxinology; Springer Netherlands: Dordrecht, 2018; pp 1–28. https://doi.org/10.1007/978-981-10-6588-0_24-2.

- (33) Pieranski, P. Two-Dimensional Interfacial Colloidal Crystals. *Phys. Rev. Lett.* **1980**, *45* (7), 569–572. <https://doi.org/10.1103/PhysRevLett.45.569>.
- (34) Rozynek, Z.; Han, M.; Dutka, F.; Garstecki, P.; Józefczak, A.; Luijten, E. Formation of Printable Granular and Colloidal Chains through Capillary Effects and Dielectrophoresis. *Nat. Commun.* **2017**, *8* (1), 15255. <https://doi.org/10.1038/ncomms15255>.
- (35) Tommaseo, G.; Petekidis, G.; Steffen, W.; Fytas, G.; Schofield, A. B.; Stefanou, N. Hypersonic Acoustic Excitations in Binary Colloidal Crystals: Big versus Small Hard Sphere Control. *J. Chem. Phys.* **2007**, *126* (1), 014707. <https://doi.org/10.1063/1.2429067>.
- (36) Wang, J.; Li, Q.; Knoll, W.; Jonas, U. Preparation of Multilayered Trimodal Colloid Crystals and Binary Inverse Opals. *J. Am. Chem. Soc.* **2006**, *128* (49), 15606–15607. <https://doi.org/10.1021/ja067221a>.
- (37) Schöttle, M.; Lauster, T.; Roemling, L. J.; Vogel, N.; Retsch, M. A Continuous Gradient Colloidal Glass. *Adv. Mater.* **2023**, *35* (7), 2208745. <https://doi.org/10.1002/adma.202208745>.
- (38) Wang, J.; Kang, E.; Sultan, U.; Merle, B.; Inayat, A.; Graczykowski, B.; Fytas, G.; Vogel, N. Influence of Surfactant-Mediated Interparticle Contacts on the Mechanical Stability of Supraparticles. *J. Phys. Chem. C* **2021**, *125* (42), 23445–23456. <https://doi.org/10.1021/acs.jpcc.1c06839>.
- (39) Wang, J.; Schwenger, J.; Ströbel, A.; Feldner, P.; Herre, P.; Romeis, S.; Peukert, W.; Merle, B.; Vogel, N. Mechanics of Colloidal Supraparticles under Compression. *Sci. Adv.* **2021**, *7* (42), eabj0954. <https://doi.org/10.1126/sciadv.abj0954>.
- (40) Jiang, S.; Van Dyk, A.; Maurice, A.; Bohling, J.; Fasano, D.; Brownell, S. Design Colloidal Particle Morphology and Self-Assembly for Coating Applications. *Chem. Soc. Rev.* **2017**, *46* (12), 3792–3807. <https://doi.org/10.1039/C6CS00807K>.
- (41) Zhang, J.; Sun, Z.; Yang, B. Self-Assembly of Photonic Crystals from Polymer Colloids. *Curr. Opin. Colloid Interface Sci.* **2009**, *14* (2), 103–114. <https://doi.org/10.1016/j.cocis.2008.09.001>.
- (42) Sun, Z. Q.; Chen, X.; Zhang, J. H.; Chen, Z. M.; Zhang, K.; Yan, X.; Wang, Y. F.; Yu, W. Z.; Yang, B. Nonspherical Colloidal Crystals Fabricated by the Thermal Pressing of Colloidal Crystal Chips. *Langmuir* **2005**, *21* (20), 8987–8991. <https://doi.org/10.1021/la051185w>.
- (43) Varghese, J.; Gapiński, J.; Pochylski, M. Brillouin Spectroscopy. In *Design, Fabrication, and Characterization of Multifunctional Nanomaterials*; Elsevier, 2022; pp 45–72. <https://doi.org/10.1016/B978-0-12-820558-7.00010-8>.
- (44) Kim, H.; Cang, Y.; Kang, E.; Graczykowski, B.; Secchi, M.; Montagna, M.; Priestley, R. D.; Furst, E. M.; Fytas, G. Direct Observation of Polymer Surface Mobility via Nanoparticle Vibrations. *Nat. Commun.* **2018**, *9* (1). <https://doi.org/10.1038/s41467-018-04854-w>.
- (45) Zhang, J.; Yang, B. Patterning Colloidal Crystals and Nanostructure Arrays by Soft Lithography. *Adv. Funct. Mater.* **2010**, *20* (20), 3411–3424. <https://doi.org/10.1002/adfm.201000795>.
- (46) Wang, L.; Xu, Y.; Chu, Z.; Tang, W.; Qiu, Y.; Zhao, X.; Jiang, W.; Ye, J.; Chen, C. Rapid Coating of Ultraviolet Shielding Colloidal Crystals. *Crystals* **2020**, *10* (6), 502. <https://doi.org/10.3390/cryst10060502>.
- (47) Katagiri, K.; Tanaka, Y.; Uemura, K.; Inumaru, K.; Seki, T.; Takeoka, Y. Structural Color Coating Films Composed of an Amorphous Array of Colloidal Particles via Electrophoretic Deposition. *NPG Asia Mater.* **2017**, *9* (3), e355–e355. <https://doi.org/10.1038/am.2017.13>.
- (48) Semmler, J.; Bley, K.; Klupp Taylor, R. N.; Stingl, M.; Vogel, N. Particulate Coatings with Optimized Haze Properties. *Adv. Funct. Mater.* **2019**, *29* (4), 1806025. <https://doi.org/10.1002/adfm.201806025>.
- (49) Zeng, Y.; Harrison, D. J. Self-Assembled Colloidal Arrays as Three-Dimensional Nanofluidic Sieves for Separation of Biomolecules on Microchips. *Anal. Chem.* **2007**, *79* (6), 2289–2295. <https://doi.org/10.1021/ac061931h>.

- (50) Zhang, J.; Li, Y.; Zhang, X.; Yang, B. Colloidal Self-Assembly Meets Nanofabrication: From Two-Dimensional Colloidal Crystals to Nanostructure Arrays. *Adv. Mater.* **2010**, *22* (38), 4249–4269. <https://doi.org/10.1002/adma.201000755>.
- (51) Jiang, P.; McFarland, M. J. Wafer-Scale Periodic Nanohole Arrays Templated from Two-Dimensional Nonclose-Packed Colloidal Crystals. *J. Am. Chem. Soc.* **2005**, *127* (11), 3710–3711. <https://doi.org/10.1021/ja042789+>.
- (52) Anker, J. N.; Hall, W. P.; Lyandres, O.; Shah, N. C.; Zhao, J.; Van Duyne, R. P. Biosensing with Plasmonic Nanosensors. *Nat. Mater.* **2008**, *7* (6), 442–453. <https://doi.org/10.1038/nmat2162>.
- (53) Mahajan, S.; Richardson, J.; Brown, T.; Bartlett, P. N. SERS-Melting: A New Method for Discriminating Mutations in DNA Sequences. *J. Am. Chem. Soc.* **2008**, *130* (46), 15589–15601. <https://doi.org/10.1021/ja805517q>.
- (54) Sharma, B.; Frontiera, R. R.; Henry, A.-I.; Ringe, E.; Van Duyne, R. P. SERS: Materials, Applications, and the Future. *Mater. Today* **2012**, *15* (1–2), 16–25. [https://doi.org/10.1016/S1369-7021\(12\)70017-2](https://doi.org/10.1016/S1369-7021(12)70017-2).
- (55) Ozbay, E. Plasmonics: Merging Photonics and Electronics at Nanoscale Dimensions. *Science* **2006**, *311* (5758), 189–193. <https://doi.org/10.1126/science.1114849>.
- (56) Weibel, D. B.; DiLuzio, W. R.; Whitesides, G. M. Microfabrication Meets Microbiology. *Nat. Rev. Microbiol.* **2007**, *5* (3), 209–218. <https://doi.org/10.1038/nrmicro1616>.
- (57) Cong, H.; Yu, B. Fabrication of Superparamagnetic Macroporous Fe₃O₄ and Its Derivates Using Colloidal Crystals as Templates. *J. Colloid Interface Sci.* **2011**, *353* (1), 131–136. <https://doi.org/10.1016/j.jcis.2010.09.040>.
- (58) Cong, H.; Cao, W. Preparation of Ordered Porous NaCl and KCl Crystals. *Solid State Sci.* **2006**, *8* (9), 1056–1060. <https://doi.org/10.1016/j.solidstatesciences.2005.12.012>.
- (59) Zhao, X. S.; Su, F.; Yan, Q.; Guo, W.; Bao, X. Y.; Lv, L.; Zhou, Z. Templating Methods for Preparation of Porous Structures. *J Mater Chem* **2006**, *16* (7), 637–648. <https://doi.org/10.1039/B513060C>.
- (60) Zhou, Z.; Yan, Q.; Su, F.; Zhao, X. S. Replicating Novel Carbon Nanostructures with 3D Macroporous Silica Template. *J. Mater. Chem.* **2005**, *15* (26), 2569. <https://doi.org/10.1039/b503691g>.
- (61) Yu, J.-S.; Kang, S.; Yoon, S. B.; Chai, G. Fabrication of Ordered Uniform Porous Carbon Networks and Their Application to a Catalyst Supporter. *J. Am. Chem. Soc.* **2002**, *124* (32), 9382–9383. <https://doi.org/10.1021/ja0203972>.
- (62) Zhang, X.; Yan, W.; Yang, H.; Liu, B.; Li, H. Gaseous Infiltration Method for Preparation of Three-Dimensionally Ordered Macroporous Polyethylene. *Polymer* **2008**, *49* (25), 5446–5451. <https://doi.org/10.1016/j.polymer.2008.09.064>.
- (63) Nishikawa, K.; Dokko, K.; Kinoshita, K.; Woo, S.-W.; Kanamura, K. Three-Dimensionally Ordered Macroporous Ni–Sn Anode for Lithium Batteries. *J. Power Sources* **2009**, *189* (1), 726–729. <https://doi.org/10.1016/j.jpowsour.2008.08.041>.
- (64) González-Urbina, L.; Baert, K.; Kolaric, B.; Pérez-Moreno, J.; Clays, K. Linear and Nonlinear Optical Properties of Colloidal Photonic Crystals. *Chem. Rev.* **2012**, *112* (4), 2268–2285. <https://doi.org/10.1021/cr200063f>.
- (65) Mihi, A.; Calvo, M. E.; Anta, J. A.; Míguez, H. Spectral Response of Opal-Based Dye-Sensitized Solar Cells. *J. Phys. Chem. C* **2008**, *112* (1), 13–17. <https://doi.org/10.1021/jp7105633>.
- (66) Xia, Y.; Gates, B.; Yin, Y.; Lu, Y. Monodispersed Colloidal Spheres: Old Materials with New Applications. *Adv. Mater.* **2000**, *12* (10), 693–713. [https://doi.org/10.1002/\(SICI\)1521-4095\(200005\)12:10<693::AID-ADMA693>3.0.CO;2-J](https://doi.org/10.1002/(SICI)1521-4095(200005)12:10<693::AID-ADMA693>3.0.CO;2-J).
- (67) Schroden, R. C.; Al-Daous, M.; Blanford, C. F.; Stein, A. Optical Properties of Inverse Opal Photonic Crystals. *Chem. Mater.* **2002**, *14* (8), 3305–3315. <https://doi.org/10.1021/cm020100z>.

- (68) Galisteo-López, J. F.; Ibisate, M.; Sapienza, R.; Froufe-Pérez, L. S.; Blanco, Á.; López, C. Self-Assembled Photonic Structures. *Adv. Mater.* **2011**, *23* (1), 30–69. <https://doi.org/10.1002/adma.201000356>.
- (69) von Freymann, G.; Kitaev, V.; Lotsch, B. V.; Ozin, G. A. Bottom-up Assembly of Photonic Crystals. *Chem Soc Rev* **2013**, *42* (7), 2528–2554. <https://doi.org/10.1039/C2CS35309A>.
- (70) Hoi, S.-K.; Chen, X.; Kumar, V. S.; Homhuan, S.; Sow, C.-H.; Bettiol, A. A. A Microfluidic Chip with Integrated Colloidal Crystal for Online Optical Analysis. *Adv. Funct. Mater.* **2011**, *21* (15), 2847–2853. <https://doi.org/10.1002/adfm.201002632>.
- (71) Li, H.; Wang, J.; Yang, L.; Song, Y. Superoleophilic and Superhydrophobic Inverse Opals for Oil Sensors. *Adv. Funct. Mater.* **2008**, *18* (20), 3258–3264. <https://doi.org/10.1002/adfm.200800507>.
- (72) Cong, H.; Yu, B.; Zhao, X. S. Imitation of Variable Structural Color in Paracheirodon Innesi Using Colloidal Crystal Films. *Opt Express* **2011**, *19* (13), 12799–12808. <https://doi.org/10.1364/OE.19.012799>.
- (73) Cong, H.; Cao, W. Thin Film Interference of Colloidal Thin Films. *Langmuir* **2004**, *20* (19), 8049–8053. <https://doi.org/10.1021/la049118+>.
- (74) Sun, C.-H.; Jiang, P.; Jiang, B. Broadband Moth-Eye Antireflection Coatings on Silicon. *Appl. Phys. Lett.* **2008**, *92* (6), 061112. <https://doi.org/10.1063/1.2870080>.
- (75) Park, B. D.; Leem, J. W.; Yu, J. S. Bioinspired Si Subwavelength Gratings by Closely-Packed Silica Nanospheres as Etch Masks for Efficient Antireflective Surface. *Appl. Phys. B* **2011**, *105* (2), 335–342. <https://doi.org/10.1007/s00340-011-4541-0>.
- (76) Cheng, W.; Wang, J.; Jonas, U.; Fytas, G.; Stefanou, N. Observation and Tuning of Hypersonic Bandgaps in Colloidal Crystals. *Nat. Mater.* **2006**, *5* (10), 830–836. <https://doi.org/10.1038/nmat1727>.
- (77) *Photonic Crystals: Molding the Flow of Light*, 2nd ed.; Joannopoulos, J. D., Ed.; Princeton University Press: Princeton, 2008.
- (78) Schneider, D.; Beltramo, P. J.; Mattarelli, M.; Pfleiderer, P.; Vermant, J.; Crespy, D.; Montagna, M.; Furst, E. M.; Fytas, G. Elongated Polystyrene Spheres as Resonant Building Blocks in Anisotropic Colloidal Crystals. *Soft Matter* **2013**, *9* (38), 9129. <https://doi.org/10.1039/c3sm50959a>.
- (79) Vasileiadis, T.; Varghese, J.; Babacic, V.; Gomis-Bresco, J.; Navarro Urrios, D.; Graczykowski, B. Progress and Perspectives on Phononic Crystals. *J. Appl. Phys.* **2021**, *129* (16), 160901. <https://doi.org/10.1063/5.0042337>.
- (80) Hou, J.; Li, M.; Song, Y. Patterned Colloidal Photonic Crystals. *Angew. Chem. Int. Ed.* **2018**, *57* (10), 2544–2553. <https://doi.org/10.1002/anie.201704752>.
- (81) Cai, Z.; Li, Z.; Ravaine, S.; He, M.; Song, Y.; Yin, Y.; Zheng, H.; Teng, J.; Zhang, A. From Colloidal Particles to Photonic Crystals: Advances in Self-Assembly and Their Emerging Applications. *Chem. Soc. Rev.* **2021**, *50* (10), 5898–5951. <https://doi.org/10.1039/D0CS00706D>.
- (82) Liu, J.; Ma, Y.; Zhu, D.; Xia, T.; Qi, Y.; Yao, Y.; Guo, X.; Ji, R.; Chen, W. Polystyrene Nanoplastics-Enhanced Contaminant Transport: Role of Irreversible Adsorption in Glassy Polymeric Domain. *Environ. Sci. Technol.* **2018**, *52* (5), 2677–2685. <https://doi.org/10.1021/acs.est.7b05211>.
- (83) Chae, Y.; An, Y.-J. Effects of Micro- and Nanoplastics on Aquatic Ecosystems: Current Research Trends and Perspectives. *Mar. Pollut. Bull.* **2017**, *124* (2), 624–632. <https://doi.org/10.1016/j.marpolbul.2017.01.070>.
- (84) Besseling, E.; Wang, B.; Lürling, M.; Koelmans, A. A. Nanoplastic Affects Growth of *S. Obliquus* and Reproduction of *D. Magna*. *Environ. Sci. Technol.* **2014**, *48* (20), 12336–12343. <https://doi.org/10.1021/es503001d>.
- (85) You, B.; Wen, N.; Shi, L.; Wu, L.; Zi, J. Facile Fabrication of a Three-Dimensional Colloidal Crystal Film with Large-Area and Robust Mechanical Properties. *J. Mater. Chem.* **2009**, *19* (22), 3594. <https://doi.org/10.1039/b906293a>.

- (86) Wang, P.; Sun, B.; Yao, T.; Chen, M.; Fan, X.; Han, H.; Li, L.; Wang, C. A Novel Dissolution and Resolidification Method for Preparing Robust Superhydrophobic Polystyrene/Silica Composite. *Chem. Eng. J.* **2017**, *326*, 1066–1073. <https://doi.org/10.1016/j.cej.2017.06.058>.
- (87) Zhang, Y.; Hao, X.; Zhou, J.; Zhang, Y.; Wang, J.; Song, Y.; Jiang, L. Tough and Hydrophilic Photonic Crystals Obtained from Direct UV Irradiation. *Macromol. Rapid Commun.* **2010**, *31* (24), 2115–2120. <https://doi.org/10.1002/marc.201000495>.
- (88) Wegewitz, L.; Prowald, A.; Meuthen, J.; Dahle, S.; Höfft, O.; Endres, F.; Maus-Friedrichs, W. Plasma Chemical and Chemical Functionalization of Polystyrene Colloidal Crystals. *Phys Chem Chem Phys* **2014**, *16* (34), 18261–18267. <https://doi.org/10.1039/C4CP01932F>.
- (89) Sekido, T.; Wooh, S.; Fuchs, R.; Kappl, M.; Nakamura, Y.; Butt, H.-J.; Fujii, S. Controlling the Structure of Supraballs by pH-Responsive Particle Assembly. *Langmuir* **2017**, *33* (8), 1995–2002. <https://doi.org/10.1021/acs.langmuir.6b04648>.
- (90) Li, H.; Wu, P.; Zhao, G.; Guo, J.; Wang, C. Fabrication of Industrial-Level Polymer Photonic Crystal Films at Ambient Temperature Based on Uniform Core/Shell Colloidal Particles. *J. Colloid Interface Sci.* **2021**, *584*, 145–153. <https://doi.org/10.1016/j.jcis.2020.09.084>.
- (91) Grady, Z. A.; Arthur, A. Z.; Wohl, C. J. Topological Control of Polystyrene-Silica Core-Shell Microspheres. *Colloids Surf. Physicochem. Eng. Asp.* **2019**, *560*, 136–140. <https://doi.org/10.1016/j.colsurfa.2018.10.019>.
- (92) Liu, T.; Pihan, S.; Roth, M.; Retsch, M.; Jonas, U.; Gutmann, J. S.; Koynov, K.; Butt, H.-J.; Berger, R. Frequency Response of Polymer Films Made from a Precursor Colloidal Monolayer on a Nanomechanical Cantilever. *Macromolecules* **2012**, *45* (2), 862–871. <https://doi.org/10.1021/ma202396h>.
- (93) Cang, Y.; Liu, B.; Das, S.; Xu, X.; Xie, J.; Deng, X.; Fytas, G. Surface Contacts Strongly Influence the Elasticity and Thermal Conductivity of Silica Nanoparticle Fibers. *Phys. Chem. Chem. Phys.* **2021**, *23* (6), 3707–3715. <https://doi.org/10.1039/D0CP05377E>.
- (94) Ghanem, M. A.; Khanolkar, A.; Zhao, H.; Boechler, N. Nanocontact Tailoring via Microlensing Enables Giant Postfabrication Mesoscopic Tuning in a Self-Assembled Ultrasonic Metamaterial. *Adv. Funct. Mater.* **2020**, *30* (10), 1909217. <https://doi.org/10.1002/adfm.201909217>.
- (95) Zhang, Y.; Hao, X.; Zhou, J.; Zhang, Y.; Wang, J.; Song, Y.; Jiang, L. Tough and Hydrophilic Photonic Crystals Obtained from Direct UV Irradiation. *Macromol. Rapid Commun.* **2010**, *31* (24), 2115–2120. <https://doi.org/10.1002/marc.201000495>.
- (96) Ayouch, A.; Dieudonné, X.; Vaudel, G.; Piombini, H.; Vallé, K.; Gusev, V.; Belleville, P.; Ruello, P. Elasticity of an Assembly of Disordered Nanoparticles Interacting via Either van Der Waals-Bonded or Covalent-Bonded Coating Layers. *ACS Nano* **2012**, *6* (12), 10614–10621. <https://doi.org/10.1021/nn303631d>.
- (97) Tohver, V.; Smay, J. E.; Braem, A.; Braun, P. V.; Lewis, J. A. Nanoparticle Halos: A New Colloid Stabilization Mechanism. *Proc. Natl. Acad. Sci.* **2001**, *98* (16), 8950–8954. <https://doi.org/10.1073/pnas.151063098>.
- (98) Landau, L. D.; Lifšic, E. M.; Landau, L. D. *Theory of Elasticity*, 3. engl. ed., rev.enlarged, reprint.; Course of theoretical physics; Elsevier: Amsterdam, 2008.
- (99) Auld, B. A. *Acoustic Fields and Waves in Solids. Vol. 1: ...*; Wiley: New York, NY, 1973.
- (100) Cowin, S. C.; Mehrabadi, M. M. Anisotropic Symmetries of Linear Elasticity. *Appl. Mech. Rev.* **1995**, *48* (5), 247–285. <https://doi.org/10.1115/1.3005102>.
- (101) Graczykowski, B.; Gomis-Bresco, J.; Alzina, F.; S Reparaz, J.; Shchepetov, A.; Prunnila, M.; Ahopelto, J.; M Sotomayor Torres, C. Acoustic Phonon Propagation in Ultra-Thin Si Membranes under Biaxial Stress Field. *New J. Phys.* **2014**, *16* (7), 073024. <https://doi.org/10.1088/1367-2630/16/7/073024>.

- (102) Zou, W.-N.; Tang, C.-X.; Lee, W.-H. Identification of Symmetry Type of Linear Elastic Stiffness Tensor in an Arbitrarily Orientated Coordinate System. *Int. J. Solids Struct.* **2013**, *50* (14–15), 2457–2467. <https://doi.org/10.1016/j.ijsolstr.2013.03.037>.
- (103) Kuok, M. H.; Lim, H. S.; Ng, S. C.; Liu, N. N.; Wang, Z. K. Brillouin Study of the Quantization of Acoustic Modes in Nanospheres. *Phys. Rev. Lett.* **2003**, *90* (25), 255502. <https://doi.org/10.1103/PhysRevLett.90.255502>.
- (104) Cheng, W.; Wang, J. J.; Jonas, U.; Steffen, W.; Fytas, G.; Penciu, R. S.; Economou, E. N. The Spectrum of Vibration Modes in Soft Opals. *J. Chem. Phys.* **2005**, *123* (12), 121104. <https://doi.org/10.1063/1.2046607>.
- (105) Penciu, R. S.; Fytas, G.; Economou, E. N.; Steffen, W.; Yannopoulos, S. N. Acoustic Excitations in Suspensions of Soft Colloids. *Phys. Rev. Lett.* **2000**, *85* (21), 4622–4625. <https://doi.org/10.1103/PhysRevLett.85.4622>.
- (106) Mazurenko, D. A.; Shan, X.; Stiefelhagen, J. C. P.; Graf, C. M.; van Blaaderen, A.; Dijkhuis, J. I. Coherent Vibrations of Submicron Spherical Gold Shells in a Photonic Crystal. *Phys. Rev. B* **2007**, *75* (16), 161102. <https://doi.org/10.1103/PhysRevB.75.161102>.
- (107) Hodak, J. H.; Henglein, A.; Hartland, G. V. Size Dependent Properties of Au Particles: Coherent Excitation and Dephasing of Acoustic Vibrational Modes. *J. Chem. Phys.* **1999**, *111* (18), 8613–8621. <https://doi.org/10.1063/1.480202>.
- (108) Duval, E.; Boukenter, A.; Champagnon, B. Vibration Eigenmodes and Size of Microcrystallites in Glass: Observation by Very-Low-Frequency Raman Scattering. *Phys. Rev. Lett.* **1986**, *56* (19), 2052–2055. <https://doi.org/10.1103/PhysRevLett.56.2052>.
- (109) Ceccato, R.; Maschio, R. D.; Gialanella, S.; Mariotto, G.; Montagna, M.; Rossi, F.; Ferrari, M.; Lipinska-Kalita, K. E.; Ohki, Y. Nucleation of Ga₂O₃ Nanocrystals in the K₂O–Ga₂O₃–SiO₂ Glass System. *J. Appl. Phys.* **2001**, *90* (5), 2522–2527. <https://doi.org/10.1063/1.1365426>.
- (110) Still, T.; Mattarelli, M.; Kiefer, D.; Fytas, G.; Montagna, M. Eigenvibrations of Submicrometer Colloidal Spheres. *J. Phys. Chem. Lett.* **2010**, *1* (16), 2440–2444. <https://doi.org/10.1021/jz100774b>.
- (111) Montagna, M. Brillouin and Raman Scattering from the Acoustic Vibrations of Spherical Particles with a Size Comparable to the Wavelength of the Light. *Phys. Rev. B* **2008**, *77* (4), 045418. <https://doi.org/10.1103/PhysRevB.77.045418>.
- (112) Lamb, H. On the Vibrations of an Elastic Sphere. *Proc. Lond. Math. Soc.* **1881**, *s1-13* (1), 189–212. <https://doi.org/10.1112/plms/s1-13.1.189>.
- (113) Montagner, J.-P.; Roullet, G. Normal Modes of the Earth. *J. Phys. Conf. Ser.* **2008**, *118*, 012004. <https://doi.org/10.1088/1742-6596/118/1/012004>.
- (114) Mattarelli, M.; Montagna, M. Comment on ‘Selection Rules for Brillouin Light Scattering from Eigenvibrations of a Sphere’ [Chem. Phys. Lett. 461 (2008) 111]. *Chem. Phys. Lett.* **2012**, *524*, 112–115. <https://doi.org/10.1016/j.cplett.2011.12.027>.
- (115) Duval, E. Far-Infrared and Raman Vibrational Transitions of a Solid Sphere: Selection Rules. *Phys. Rev. B* **1992**, *46* (9), 5795–5797. <https://doi.org/10.1103/PhysRevB.46.5795>.
- (116) Li, Y.; Lim, H. S.; Ng, S. C.; Wang, Z. K.; Kuok, M. H. Selection Rules for Brillouin Light Scattering from Eigenvibrations of a Sphere. *Chem. Phys. Lett.* **2008**, *461* (1–3), 111–113. <https://doi.org/10.1016/j.cplett.2008.07.003>.
- (117) Lu, M.-H.; Feng, L.; Chen, Y.-F. Phononic Crystals and Acoustic Metamaterials. *Mater. Today* **2009**, *12* (12), 34–42. [https://doi.org/10.1016/S1369-7021\(09\)70315-3](https://doi.org/10.1016/S1369-7021(09)70315-3).
- (118) Wang, Y.-F.; Wang, Y.-Z.; Wu, B.; Chen, W.; Wang, Y.-S. Tunable and Active Phononic Crystals and Metamaterials. *Appl. Mech. Rev.* **2020**, *72* (4), 040801. <https://doi.org/10.1115/1.4046222>.
- (119) Yablonovitch, E. Inhibited Spontaneous Emission in Solid-State Physics and Electronics. *Phys. Rev. Lett.* **1987**, *58* (20), 2059–2062. <https://doi.org/10.1103/PhysRevLett.58.2059>.

- (120) John, S. Strong Localization of Photons in Certain Disordered Dielectric Superlattices. *Phys. Rev. Lett.* **1987**, *58* (23), 2486–2489. <https://doi.org/10.1103/PhysRevLett.58.2486>.
- (121) Vasseur, J. O.; Deymier, P. A.; Chenni, B.; Djafari-Rouhani, B.; Dobrzynski, L.; Prevost, D. Experimental and Theoretical Evidence for the Existence of Absolute Acoustic Band Gaps in Two-Dimensional Solid Phononic Crystals. *Phys. Rev. Lett.* **2001**, *86* (14), 3012–3015. <https://doi.org/10.1103/PhysRevLett.86.3012>.
- (122) Cang, Y.; Jin, Y.; Djafari-Rouhani, B.; Fytas, G. Fundamentals, Progress and Perspectives on High-Frequency Phononic Crystals. *J. Phys. Appl. Phys.* **2022**, *55* (19), 193002. <https://doi.org/10.1088/1361-6463/ac4941>.
- (123) Priya; Cardozo De Oliveira, E. R.; Lanzillotti-Kimura, N. D. Perspectives on High-Frequency Nanomechanics, Nanoacoustics, and Nanophononics. *Appl. Phys. Lett.* **2023**, *122* (14), 140501. <https://doi.org/10.1063/5.0142925>.
- (124) Gorishnyy, T.; Ullal, C. K.; Maldovan, M.; Fytas, G.; Thomas, E. L. Hypersonic Phononic Crystals. *Phys. Rev. Lett.* **2005**, *94* (11), 115501. <https://doi.org/10.1103/PhysRevLett.94.115501>.
- (125) Maldovan, M.; Thomas, E. L. Simultaneous Localization of Photons and Phonons in Two-Dimensional Periodic Structures. *Appl. Phys. Lett.* **2006**, *88* (25), 251907. <https://doi.org/10.1063/1.2216885>.
- (126) Jang, J.-H.; Ullal, C. K.; Gorishnyy, T.; Tsukruk, V. V.; Thomas, E. L. Mechanically Tunable Three-Dimensional Elastomeric Network/Air Structures via Interference Lithography. *Nano Lett.* **2006**, *6* (4), 740–743. <https://doi.org/10.1021/nl052577q>.
- (127) Wang, J.; Ahl, S.; Li, Q.; Kreiter, M.; Neumann, T.; Burkert, K.; Knoll, W.; Jonas, U. Structural and Optical Characterization of 3D Binary Colloidal Crystal and Inverse Opal Films Prepared by Direct Co-Deposition. *J. Mater. Chem.* **2008**, *18* (9), 981. <https://doi.org/10.1039/b715329e>.
- (128) Psarobas, I. E.; Modinos, A.; Sainidou, R.; Stefanou, N. Acoustic Properties of Colloidal Crystals. *Phys. Rev. B* **2002**, *65* (6), 064307. <https://doi.org/10.1103/PhysRevB.65.064307>.
- (129) Gorishnyy, T.; Jang, J.-H.; Koh, C.; Thomas, E. L. Direct Observation of a Hypersonic Band Gap in Two-Dimensional Single Crystalline Phononic Structures. *Appl. Phys. Lett.* **2007**, *91* (12), 121915. <https://doi.org/10.1063/1.2786605>.
- (130) Jing, X.; Sheng, P.; Zhou, M. Theory of Acoustic Excitations in Colloidal Suspensions. *Phys. Rev. Lett.* **1991**, *66* (9), 1240–1243. <https://doi.org/10.1103/PhysRevLett.66.1240>.
- (131) Liu, J.; Ye, L.; Weitz, D. A.; Sheng, P. Novel Acoustic Excitations in Suspensions of Hard-Sphere Colloids. *Phys. Rev. Lett.* **1990**, *65* (20), 2602–2605. <https://doi.org/10.1103/PhysRevLett.65.2602>.
- (132) Still, T.; Cheng, W.; Retsch, M.; Sainidou, R.; Wang, J.; Jonas, U.; Stefanou, N.; Fytas, G. Simultaneous Occurrence of Structure-Directed and Particle-Resonance-Induced Phononic Gaps in Colloidal Films. *Phys. Rev. Lett.* **2008**, *100* (19), 194301. <https://doi.org/10.1103/PhysRevLett.100.194301>.
- (133) Kang, E.; Graczykowski, B.; Jonas, U.; Christie, D.; Gray, L. A. G.; Cangialosi, D.; Priestley, R. D.; Fytas, G. Shell Architecture Strongly Influences the Glass Transition, Surface Mobility, and Elasticity of Polymer Core-Shell Nanoparticles. *Macromolecules* **2019**, *52* (14), 5399–5406. <https://doi.org/10.1021/acs.macromol.9b00766>.
- (134) Kang, E.; Kim, H.; Gray, L. A. G.; Christie, D.; Jonas, U.; Graczykowski, B.; Furst, E. M.; Priestley, R. D.; Fytas, G. Ultrathin Shell Layers Dramatically Influence Polymer Nanoparticle Surface Mobility. *Macromolecules* **2018**, *51* (21), 8522–8529. <https://doi.org/10.1021/acs.macromol.8b01804>.
- (135) Still, T.; D'Acunzi, M.; Vollmer, D.; Fytas, G. Mesospheres in Nano-Armor: Probing the Shape-Persistence of Molten Polymer Colloids. *J. Colloid Interface Sci.* **2009**, *340* (1), 42–45. <https://doi.org/10.1016/j.jcis.2009.08.022>.

- (136) Zhang, C.; Guo, Y.; Priestley, R. D. Glass Transition Temperature of Polymer Nanoparticles under Soft and Hard Confinement. *Macromolecules* **2011**, *44* (10), 4001–4006. <https://doi.org/10.1021/ma1026862>.
- (137) Feng, S.; Li, Z.; Liu, R.; Mai, B.; Wu, Q.; Liang, G.; Gao, H.; Zhu, F. Glass Transition of Polystyrene Nanospheres under Different Confined Environments in Aqueous Dispersions. *Soft Matter* **2013**, *9* (18), 4614. <https://doi.org/10.1039/c3sm27576k>.
- (138) Keddie, J. L.; Jones, R. A. L.; Cory, R. A. Size-Dependent Depression of the Glass Transition Temperature in Polymer Films. *Europhys. Lett. EPL* **1994**, *27* (1), 59–64. <https://doi.org/10.1209/0295-5075/27/1/011>.
- (139) Priestley, R. D.; Broadbelt, L. J.; Torkelson, J. M.; Fukao, K. Glass Transition and α -Relaxation Dynamics of Thin Films of Labeled Polystyrene. *Phys. Rev. E* **2007**, *75* (6), 061806. <https://doi.org/10.1103/PhysRevE.75.061806>.
- (140) Yang, Z.; Fujii, Y.; Lee, F. K.; Lam, C.-H.; Tsui, O. K. C. Glass Transition Dynamics and Surface Layer Mobility in Unentangled Polystyrene Films. *Science* **2010**, *328* (5986), 1676–1679. <https://doi.org/10.1126/science.1184394>.
- (141) Chen, M.; Jabeen, F.; Rasulev, B.; Ossowski, M.; Boudjouk, P. A Computational Structure-Property Relationship Study of Glass Transition Temperatures for a Diverse Set of Polymers. *J. Polym. Sci. Part B Polym. Phys.* **2018**, *56* (11), 877–885. <https://doi.org/10.1002/polb.24602>.
- (142) Boyer, S. A. E.; Grolier, J.-P. E. Modification of the Glass Transitions of Polymers by High-Pressure Gas Solubility. *Pure Appl. Chem.* **2005**, *77* (3), 593–603. <https://doi.org/10.1351/pac200577030593>.
- (143) Wang, W.-C. V.; Kramer, E. J.; Sachse, W. H. Effects of High-Pressure CO₂ on the Glass Transition Temperature and Mechanical Properties of Polystyrene. *J. Polym. Sci. Polym. Phys. Ed.* **1982**, *20* (8), 1371–1384. <https://doi.org/10.1002/pol.1982.180200804>.
- (144) Ghosh, K.; Krishnamurthy, C. V. Structural Behavior of Supercritical Fluids under Confinement. *Phys Rev E* **2018**, *97* (1), 012131. <https://doi.org/10.1103/PhysRevE.97.012131>.
- (145) Quach, A.; Simha, R. Pressure-Volume-Temperature Properties and Transitions of Amorphous Polymers; Polystyrene and Poly (Orthomethylstyrene). *J. Appl. Phys.* **1971**, *42* (12), 4592–4606.
- (146) Mahmood, S. H.; Xin, C. L.; Gong, P.; Lee, J. H.; Li, G.; Park, C. B. Dimethyl Ether's Plasticizing Effect on Carbon Dioxide Solubility in Polystyrene. *Polymer* **2016**, *97*, 95–103. <https://doi.org/10.1016/j.polymer.2016.05.018>.
- (147) Vieth, W. R.; Tam, P. M.; Michaels, A. S. Dual Sorption Mechanisms in Glassy Polystyrene. *J. Colloid Interface Sci.* **1966**, *22* (4), 360–370. [https://doi.org/10.1016/0021-9797\(66\)90016-6](https://doi.org/10.1016/0021-9797(66)90016-6).
- (148) Immergut, E. H.; Mark, H. F. Principles of Plasticization; ACS Publications, 1965.
- (149) Cheng, W.; Wang, J.; Jonas, U.; Fytas, G.; Stefanou, N. Observation and Tuning of Hypersonic Bandgaps in Colloidal Crystals. *Nat. Mater.* **2006**, *5* (10), 830–836. <https://doi.org/10.1038/nmat1727>.
- (150) Berne, B. J.; Pecora, R. *Dynamic Light Scattering: With Applications to Chemistry, Biology, and Physics*, Dover ed.; Dover Publications: Mineola, N.Y., 1976.
- (151) Brillouin, L. Diffusion de La Lumière et Des Rayons X Par Un Corps Transparent Homogène: Influence de l'agitation Thermique. *Ann. Phys.* **1922**, *9* (17), 88–122. <https://doi.org/10.1051/anphys/192209170088>.
- (152) Meng, Z.; Traverso, A. J.; Ballmann, C. W.; Troyanova-Wood, M. A.; Yakovlev, V. V. Seeing Cells in a New Light: A Renaissance of Brillouin Spectroscopy. *Adv. Opt. Photonics* **2016**, *8* (2), 300. <https://doi.org/10.1364/AOP.8.000300>.
- (153) Palombo, F.; Fioretto, D. Brillouin Light Scattering: Applications in Biomedical Sciences. *Chem. Rev.* **2019**, *119* (13), 7833–7847. <https://doi.org/10.1021/acs.chemrev.9b00019>.
- (154) Gross, E. Change of Wave-Length of Light Due to Elastic Heat Waves at Scattering in Liquids. *Nature* **1930**, *126* (3171), 201–202. <https://doi.org/10.1038/126201a0>.

- (155) *Laser Handbook. Vol. 2: ...*; Arecchi, F. T., Schulz-Dubois, E. O., Eds.; North-Holland Publ. Co: Amsterdam, 1972.
- (156) Singaraju, A. B.; Bahl, D.; Stevens, L. L. Brillouin Light Scattering: Development of a Near Century-Old Technique for Characterizing the Mechanical Properties of Materials. *AAPS PharmSciTech* **2019**, *20* (3), 109. <https://doi.org/10.1208/s12249-019-1311-5>.
- (157) Dil, J. G.; van Hijningen, N. C. J. A.; van Dorst, F.; Aarts, R. M. Tandem Multipass Fabry-Perot Interferometer for Brillouin Scattering. *Appl. Opt.* **1981**, *20* (8), 1374. <https://doi.org/10.1364/AO.20.001374>.
- (158) Ménard, M.; Kirk, A. G. Design of Fabry-Perot Filters in Planar Waveguides with Deep-Etched Features for Spatial Switching. *Opt Express* **2009**, *17* (20), 17614–17629. <https://doi.org/10.1364/OE.17.017614>.
- (159) Mock, R.; Hillebrands, B.; Sandercock, R. Construction and Performance of a Brillouin Scattering Set-up Using a Triple-Pass Tandem Fabry-Perot Interferometer. *J. Phys. [E]* **1987**, *20* (6), 656–659. <https://doi.org/10.1088/0022-3735/20/6/017>.
- (160) Chu, B. *Laser Light Scattering: Basic Principles and Practice*, 2nd ed.; Academic Press: Boston, 1991.
- (161) J. R. Sandercock. Tandem Fabry-Perot Interferometer TFP-1, Operator Manual. JRS Scientific Instruments.
- (162) Sandercock, J. R. Trends in Brillouin Scattering: Studies of Opaque Materials, Supported Films, and Central Modes. In *Light Scattering in Solids III*; Cardona, M., Güntherodt, G., Eds.; Springer Berlin Heidelberg: Berlin, Heidelberg, 1982; Vol. 51, pp 173–206. https://doi.org/10.1007/3540115137_6.
- (163) Goodwin, J. W.; Hearn, J.; Ho, C. C.; Ottewill, R. H. Studies on the Preparation and Characterisation of Monodisperse Polystyrene Lattice: III. Preparation without Added Surface Active Agents. *Colloid Polym. Sci.* **1974**, *252* (6), 464–471. <https://doi.org/10.1007/BF01554752>.
- (164) Shen, S.; Sudol, E. D.; El-Aasser, M. S. Control of Particle Size in Dispersion Polymerization of Methyl Methacrylate. *J. Polym. Sci. Part Polym. Chem.* **1993**, *31* (6), 1393–1402. <https://doi.org/10.1002/pola.1993.080310606>.
- (165) Stein, A.; Wilson, B. E.; Rudisill, S. G. Design and Functionality of Colloidal-Crystal-Templated Materials—Chemical Applications of Inverse Opals. *Chem Soc Rev* **2013**, *42* (7), 2763–2803. <https://doi.org/10.1039/C2CS35317B>.
- (166) Mattarelli, M.; Montagna, M.; Still, T.; Schneider, D.; Fytas, G. Vibration Spectroscopy of Weakly Interacting Mesoscopic Colloids. *Soft Matter* **2012**, *8* (15), 4235. <https://doi.org/10.1039/c2sm07034k>.
- (167) Fytas, G.; Meier, G.; Dorfmueller, T. Rayleigh-Brillouin Spectra of Poly[(Phenylmethyl)Siloxane] under High Pressures. *Macromolecules* **1985**, *18* (5), 993–996. <https://doi.org/10.1021/ma00147a031>.
- (168) Johnson, K. L.; Kendall, K.; Roberts, A. D. Surface Energy and the Contact of Elastic Solids. *Proc. R. Soc. Math. Phys. Eng. Sci.* **1971**, *324* (1558), 301–313. <https://doi.org/10.1098/rspa.1971.0141>.
- (169) Israelachvili, J. N. *Intermolecular and Surface Forces*, 3rd ed.; Academic Press: Burlington, MA, 2011.
- (170) Kim, H.; Cang, Y.; Kang, E.; Graczykowski, B.; Secchi, M.; Montagna, M.; Priestley, R. D.; Furst, E. M.; Fytas, G. Direct Observation of Polymer Surface Mobility via Nanoparticle Vibrations. *Nat. Commun.* **2018**, *9* (1), 2918.
- (171) Graczykowski, B.; Vogel, N.; Bley, K.; Butt, H.-J.; Fytas, G. Multiband Hypersound Filtering in Two-Dimensional Colloidal Crystals: Adhesion, Resonances, and Periodicity. *Nano Lett.* **2020**, *20* (3), 1883–1889.
- (172) Hughes, D. S.; Kelly, J. L. Second-Order Elastic Deformation of Solids. *Phys. Rev.* **1953**, *92* (5), 1145–1149. <https://doi.org/10.1103/PhysRev.92.1145>.

- (173) Abi Ghanem, M.; Khanolkar, A.; Wallen, S. P.; Helwig, M.; Hiraiwa, M.; Maznev, A. A.; Vogel, N.; Boechler, N. Longitudinal Eigenvibration of Multilayer Colloidal Crystals and the Effect of Nanoscale Contact Bridges. *Nanoscale* **2019**, *11* (12), 5655–5665. <https://doi.org/10.1039/C8NR08453J>.
- (174) Pochylski, M. Structural Relaxation in the Wave-Vector Dependence of the Longitudinal Rigidity Modulus. *Biomed. Opt. Express* **2019**, *10* (4), 1957. <https://doi.org/10.1364/BOE.10.001957>.
- (175) Naji, M.; Piazza, F.; Guimbretière, G.; Canizarès, A.; Vaills, Y. Structural Relaxation Dynamics and Annealing Effects of Sodium Silicate Glass. *J. Phys. Chem. B* **2013**, *117* (18), 5757–5764. <https://doi.org/10.1021/jp401112s>.
- (176) Kröger, J. K.; Marx, A.; Peetz, L.; Roberts, R.; Unruh, H.-G. Simultaneous Determination of Elastic and Optical Properties of Polymers by High Performance Brillouin Spectroscopy Using Different Scattering Geometries. *Colloid Polym. Sci.* **1986**, *264* (5), 403–414. <https://doi.org/10.1007/BF01419544>.
- (177) Lemmon, E.; Huber, M.; McLinden, M. NIST Standard Reference Database 23: Reference Fluid Thermodynamic and Transport Properties-REFPROP, Version 9.1, 2013. https://tsapps.nist.gov/publication/get_pdf.cfm?pub_id=912382.
- (178) Gosman, A. L.; McCarty, R. D.; Hust, J. G. *Thermodynamic Properties of Argon from the Triple Point to 300 K at Pressures to 1000 Atmospheres*, 0 ed.; NBS NSRDS 27; National Bureau of Standards: Gaithersburg, MD, 1969; p NBS NSRDS 27. <https://doi.org/10.6028/NBS.NSRDS.27>.
- (179) Younglove, B.; Olien, N. A.; Standards, U. S. N. B. of. *Tables of Industrial Gas Container Contents and Density for Oxygen, Argon, Nitrogen, Helium, and Hydrogen*; NBS technical note; U.S. Department of Commerce, National Bureau of Standards, 1985.
- (180) Hughes, D. S.; Kelly, J. L. Second-Order Elastic Deformation of Solids. *Phys Rev* **1953**, *92* (5), 1145–1149. <https://doi.org/10.1103/PhysRev.92.1145>.
- (181) Durrill, P. L.; Griskey, R. G. Diffusion and Solution of Gases in Thermally Softened or Molten Polymers: Part I. Development of Technique and Determination of Data. *AIChE J.* **1966**, *12* (6), 1147–1151. <https://doi.org/10.1002/aic.690120619>.
- (182) Yan, Z. Influence of Acoustic Leakage at Fluid–Solid Interface on Interferometric Detection of Surface Acoustic Wave. *Optik* **2014**, *125* (10), 2458–2462. <https://doi.org/10.1016/j.ijleo.2013.10.117>.
- (183) Vieth, W. R.; Tam, P. M.; Michaels, A. S. Dual Sorption Mechanisms in Glassy Polystyrene. *J. Colloid Interface Sci.* **1966**, *22* (4), 360–370. [https://doi.org/10.1016/0021-9797\(66\)90016-6](https://doi.org/10.1016/0021-9797(66)90016-6).
- (184) Quach, A.; Simha, R. Pressure-Volume-Temperature Properties and Transitions of Amorphous Polymers; Polystyrene and Poly (Orthomethylstyrene). *J. Appl. Phys.* **1971**, *42* (12), 4592–4606. <https://doi.org/10.1063/1.1659828>.
- (185) Rindfleisch, F.; DiNoia, T. P.; McHugh, M. A. Solubility of Polymers and Copolymers in Supercritical CO₂. *J. Phys. Chem.* **1996**, *100* (38), 15581–15587. <https://doi.org/10.1021/jp9615823>.
- (186) Simpson, J. H.; Wen; Jones, A. A.; Inglefield, P. T.; Bendler, J. T. Diffusion Coefficients of Xenon in Polystyrene Determined by Xenon-129 NMR Spectroscopy. *Macromolecules* **1996**, *29* (6), 2138–2142. <https://doi.org/10.1021/ma951213p>.

Journal Contributions

Jeena Varghese

Poznan, 30.06.2023

Faculty of Physics

Adam Mickiewicz University

Ul. Uniwersytetu Poznanskiego 2, 61-614 Poznan, Poland.

STATEMENT

Hereby, I provide a statement about my contribution to the following article:

Jeena Varghese, Reza Mohammadi, Mikolaj Pochylski, Visnja Babacic, Jacek Gapinski, Nicolas Vogel, Hans-Juergen Butt, George Fytas, Bartlomiej Graczykowski, Size-dependent nanoscale soldering of polystyrene colloidal crystals by supercritical fluids, J. Colloid Interface Sci. 633 (2023) 314–322. <https://doi.org/10.1016/j.jcis.2022.11.090>.

My contribution to this work consisted in:

- Conceptualization
- Preparation of 3D PS CCs and PS monolayer for BLS and SEM measurements.
- BLS measurements of gas, and all PS CCs in different gas environments.
- Data analysis and calculations
- Discussion of results
- Preparation of initial drafts of Figures 1, 2, 3a,3b, 4a, 5 in the manuscript
- Preparation of the initial drafts of the manuscript
- Preparation of supporting information

In percentage my contribution to the manuscript is 60%



Supervisor's signature



Signature

Jeena Varghese

Poznan, 30.06.2023

Faculty of Physics

Adam Mickiewicz University

Ul. Uniwersytetu Poznanskiego 2, 61-614 Poznan, Poland.

STATEMENT

Hereby, I provide a statement about my contribution to the following article:

Visnja Babacic, Jeena Varghese, Emerson Coy, Eunsoo Kang, Mikolaj Pochylski, Jacek Gapinski, George Fytas, Bartlomiej Graczykowski, Mechanical reinforcement of polymer colloidal crystals by supercritical fluids, J. Colloid Interface Sci. 579 (2020) 786–793. <https://doi.org/10.1016/j.jcis.2020.06.104>.

My contribution to this work consisted in:

- Preparation of samples for BLS measurements (20 % of used samples)
- Part in BLS measurements (60 % of measurements at given pressure, temperature and time conditions)
- Part in BLS experimental data analysis (Result presented in Figure 3)
- Preparation of Figures 3 (a), (b), and (c).
- Discussion of the results
- Revising the manuscript

In percentage my contribution to the manuscript is 30%



Supervisor's signature



Signature

Jeena Varghese

Poznan, 30.06.2023

Faculty of Physics

Adam Mickiewicz University

Ul. Uniwersytetu Poznanskiego 2, 61-614 Poznan, Poland.

STATEMENT

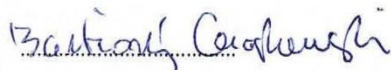
Hereby, I provide a statement about my contribution to the following review article:

*Thomas Vasileiadis, Jeena Varghese, Visnja Babacic, Jordi Gomis-Bresco, Daniel Navarro Urrios, *Bartłomiej Graczykowski.* Progress and perspectives on phononic crystals, Journal of Applied Physics, 129, 160901 (2021); <https://doi.org/10.1063/5.0042337>

My contribution to this work consisted in:

- Writing the article - section II – sub GHz phononic crystals
- Preparation of Figures 2,3
- Review and discussions
- Revising the manuscript

In percentage my contribution to the manuscript is 20%



Supervisor's signature



Signature

Jeena Varghese

Poznan, 30.06.2023

Faculty of Physics

Adam Mickiewicz University

Ul. Uniwersytetu Poznanskiego 2, 61-614 Poznan, Poland.

STATEMENT

Hereby, I provide a statement about my contribution to the following book chapter:

Jeena Varghese, Mikolaj Pochylski, Jacek Gapinski, Brillouin Spectroscopy: probing the acoustic vibrations in colloidal nanoparticles, In the book: "Design, Fabrication and Characterization of multifunctional nanomaterials", Elsevier Ltd. (2022);

<https://doi.org/10.1016/B978-0-12-820558-7.00010-8>

My contribution to this work consisted in:

- Preparation of the full chapter
- Review and discussion
- Revising the manuscript

In percentage my contribution to the manuscript is 80%



Supervisor's signature



Signature

Bartłomiej Graczykowski

Poznan, 30.06.2023

Faculty of Physics

Adam Mickiewicz University

Ul. Uniwersytetu Poznanskiego 2, 61-614 Poznan, Poland.

STATEMENT

Hereby, I provide a statement about my contribution to the following article:

Jeena Varghese, Reza Mohammadi, Mikolaj Pochylski, Visnja Babacic, Jacek Gapinski, Nicolas Vogel, Hans-Juergen Butt, George Fytas, Bartłomiej Graczykowski, Size-dependent nanoscale soldering of polystyrene colloidal crystals by supercritical fluids, J. Colloid Interface Sci. 633 (2023) 314–322. <https://doi.org/10.1016/j.jcis.2022.11.090>.

My contribution to this work consisted in:

- Conceiving the project
- Part of BLS experiments (building set-up)
- Data analysis
- Discussion of results
- Preparation of Figures 3 c, and 4 b
- Revising all figures in the manuscript.
- Editing and rewriting the final manuscript



Signature

Bartłomiej Graczykowski

Poznan, 30.06.2023

Faculty of Physics

Adam Mickiewicz University

Ul. Uniwersytetu Poznanskiego 2, 61-614 Poznan, Poland.

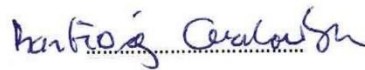
STATEMENT

Hereby, I provide a statement about my contribution to the following article:

Visnja Babacic, Jeena Varghese, Emerson Coy, Eunsoo Kang, Mikolaj Pochylski, Jacek Gapinski, George Fytas, Bartłomiej Graczykowski, Mechanical reinforcement of polymer colloidal crystals by supercritical fluids, J. Colloid Interface Sci. 579 (2020) 786–793. <https://doi.org/10.1016/j.jcis.2020.06.104>.

My contribution to this work consisted in:

- Conceiving the project
- Discussion of the results
- Preparation of Figure 1 a, S1
- Revising and editing the manuscript



Signature

Visnja Babacic

Poznan, 30.06.2023

Faculty of Physics

Adam Mickiewicz University

Ul. Uniwersytetu Poznanskiego 2, 61-614 Poznan, Poland.

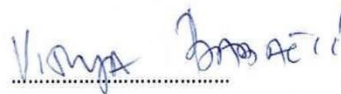
STATEMENT

Hereby, I provide a statement about my contribution to the following article:

Visnja Babacic, Jeena Varghese, Emerson Coy, Eunsoo Kang, Mikolaj Pochylski, Jacek Gapinski, George Fytas, Bartlomiej Graczykowski, Mechanical reinforcement of polymer colloidal crystals by supercritical fluids, J. Colloid Interface Sci. 579 (2020) 786–793. <https://doi.org/10.1016/j.jcis.2020.06.104>.

My contribution to this work consisted in:

- Preparation of samples for BLS measurements (80 % of used samples).
- Part in BLS measurements (40 % of measurements at given pressure, temperature, and time conditions).
- Part in BLS experimental data analysis (Results presented in Figure 2, Figure 4, and Figure 5).
- Calculations presented in manuscript and supporting information.
- Preparation of Figure 1, Figure 2, Figure 3 (d), Figure 4, Figure 5, Figure S1 and Figure S3
- Discussion of results
- Writing the first draft of the manuscript
- Writing the first draft of supporting information



Signature

Visnja Babacic

Poznan, 30.06.2023

Faculty of Physics

Adam Mickiewicz University

Ul. Uniwersytetu Poznanskiego 2, 61-614 Poznan, Poland.

STATEMENT

Hereby, I provide a statement about my contribution to the following article:

Jeena Varghese, Reza Mohammadi, Mikolaj Pochylski, Visnja Babacic, Jacek Gapinski, Nicolas Vogel, Hans-Juergen Butt, George Fytas, Bartlomiej Graczykowski, Size-dependent nanoscale soldering of polystyrene colloidal crystals by supercritical fluids, J. Colloid Interface Sci. 633 (2023) 314–322. <https://doi.org/10.1016/j.jcis.2022.11.090>.

My contribution to this work consisted in:

- Discussion of results
- Preparation of initial drafts of Figure 3c, 4b
- Revising the manuscript



Signature

Emerson Coy

Poznan, 30.06.2023

NanoBioMedical Centre

Adam Mickiewicz University

Wszecznicy Piastowskiej 3, 61-614 Poznań

STATEMENT

Hereby, I provide a statement about my contribution to the following article:

Visnja Babacic, Jeena Varghese, Emerson Coy, Eunsoo Kang, Mikolaj Pochylski, Jacek Gapinski, George Fytas, Bartlomiej Graczykowski, Mechanical reinforcement of polymer colloidal crystals by supercritical fluids, J. Colloid Interface Sci. 579 (2020) 786–793. <https://doi.org/10.1016/j.jcis.2020.06.104>.

My contribution to this work consisted in:

- SEM measurements in Figure 1 (b) and (c), Figure 2 and Figure 4.
- TEM measurements in Figure S2.
- Revising the manuscript.



Signature

Mikolaj Pochylski

Poznan, 30.06.2023

Faculty of Physics

Adam Mickiewicz University

Ul. Uniwersytetu Poznanskiiego 2, 61-614 Poznan, Poland.

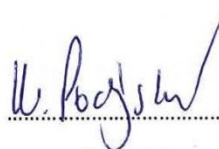
STATEMENT

Hereby, I provide a statement about my contribution to the following article:

Jeena Varghese, Reza Mohammadi, Mikolaj Pochylski, Visnja Babacic, Jacek Gapinski, Nicolas Vogel, Hans-Juergen Butt, George Fytas, Bartlomiej Graczykowski, Size-dependent nanoscale soldering of polystyrene colloidal crystals by supercritical fluids, J. Colloid Interface Sci. 633 (2023) 314–322. <https://doi.org/10.1016/j.jcis.2022.11.090>.

My contribution to this work consisted in:

- Part in BLS measurements (setup alignment).
- Building setup for BLS measurements in different geometries.
- Discussion of results, calculations
- Revising the manuscript



Signature

Mikolaj Pochylski

Poznan, 30.06.2023

Faculty of Physics

Adam Mickiewicz University

Ul. Uniwersytetu Poznanskiego 2, 61-614 Poznan, Poland.

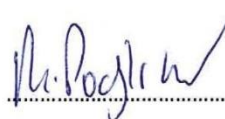
STATEMENT

Hereby, I provide a statement about my contribution to the following article:

Visnja Babacic, Jeena Varghese, Emerson Coy, Eunsoo Kang, Mikolaj Pochylski, Jacek Gapinski, George Fytas, Bartlomiej Graczykowski, Mechanical reinforcement of polymer colloidal crystals by supercritical fluids, J. Colloid Interface Sci. 579 (2020) 786–793. <https://doi.org/10.1016/j.jcis.2020.06.104>.

My contribution to this work consisted in:

- Part in BLS measurements (setup alignment and creation of software for time-dependent measurements)
- Discussion of the results
- Revising the manuscript



Signature

Jacek Gapinski

Poznan, 30.06.2023

Faculty of Physics

Adam Mickiewicz University

Ul. Uniwersytetu Poznanskiego 2, 61-614 Poznan, Poland.

STATEMENT

Hereby, I provide a statement about my contribution to the following article:

Jeena Varghese, Reza Mohammadi, Mikolaj Pochylski, Visnja Babacic, Jacek Gapinski, Nicolas Vogel, Hans-Juergen Butt, George Fytas, Bartlomiej Graczykowski, Size-dependent nanoscale soldering of polystyrene colloidal crystals by supercritical fluids, J. Colloid Interface Sci. 633 (2023) 314–322. <https://doi.org/10.1016/j.jcis.2022.11.090>.

My contribution to this work consisted in:

- BLS measurements (setup alignment)
- Discussion of the results
- Revising the manuscript



Signature

Jacek Gapinski

Poznan, 30.06.2023

Faculty of Physics

Adam Mickiewicz University

Ul. Uniwersytetu Poznanskiego 2, 61-614 Poznan, Poland.

STATEMENT

Hereby, I provide a statement about my contribution to the following article:

Visnja Babacic, Jeena Varghese, Emerson Coy, Eunsoo Kang, Mikolaj Pochylski, Jacek Gapinski, George Fytas, Bartlomiej Graczykowski, Mechanical reinforcement of polymer colloidal crystals by supercritical fluids, J. Colloid Interface Sci. 579 (2020) 786–793. <https://doi.org/10.1016/j.jcis.2020.06.104>.

My contribution to this work consisted in:

- Part in BLS measurements (setup alignment)
- Discussion of the results
- Revising the manuscript



Signature

Acknowledgments

Time flies! Towards the end of my PhD journey, I realize that these years have made me a better research scholar and a better version of myself. I take this opportunity to express my boundless gratitude to all the people who advised, supported and motivated me during my PhD and life in Poznan.

First of all, I sincerely thank my PhD supervisor Prof. UAM Dr. hab. Bartłomiej Graczykowski, for hiring me as a PhD student in his FNP project and giving an excellent opportunity to work in his research group. I learned from him the basics of Brillouin light scattering, especially to work in the optics laboratory. His immense knowledge, advices, and wholehearted support has been precious for the development of this research work and more importantly, for my personal growth. I'm really grateful for his patience and understanding, and letting me work and learn independently. Many thanks Bartek!

I express my deepest gratitude to Prof. UAM Dr. hab. Jacek Gapiński and Prof. UAM Dr. hab. Mikołaj Pochylski for the timely advices, scientific discussions and motivation during my PhD. Thank you for training me to work in the BLS and chemical labs and helping me with the trouble shooting.

I'm greatly indebted to Prof. Dr. George Fytas from Max Planck Institute of Polymer Research, Mainz, Germany, for the collaboration and scientific discussions regarding acoustics of colloidal crystals. Thank you for working with me in Poznan, for reviewing and editing the manuscript.

I express my profound gratitude to Prof. Dr. rer.net. Nicolas Vogel and his research group in the Institute of Particle technology, Friedrich-Alexander Universität Erlangen-Nürnberg, for their guidance and wholehearted support during my internship. I specially thank Dr. Reza Mohammadi for training me with the fabrication of colloidal monolayers.

Now, I sincerely thank my colleagues, Dr. Višnja Babačić, Dr. Thomas Vasileiadis and Prof. UAM Dr. hab. Emerson Coy, for helping and supporting me during my PhD and in my life in Poznan.

I genuinely thank all the members of Zakład Biofizyki Molekularnej (ZBM) for your kindness and support. At many times, I felt ZBM as my second home, when I'm far away from my real family. Thanks for the scientific meetings, Christmas celebrations, and lunch-break discussions. I want to thank Dr. Rafał Białek for being a supportive colleague and especially, for organizing all the "Very Important and Official Meetings". I would like to thank all the present and former colleagues in our research group – Dr. Adam Krysztofik, Dr. Anuj Kumar Dhiman, mgr. Małgorzata Bartkiewicz, mgr. Maciej Kasprzak. I also thank mgr. Alice Goyal for being my good friend and colleague from ZBM.

I would like to thank Faculty of Physics, UAM for providing a friendly working environment. Especially, I thank Prof. Slawomir Breiter for all the advices and suggestions with the PhD procedures. I also express my sincere thanks to the UAM community – especially, mgr. Joanna Barszcz, mgr. Anna Kolańczyk-Marszałek, mgr. Joanna Kubicka and all the other administration employees, for helping me during my PhD.

I thank Foundation for Polish Science (FNP) for providing the research funding during my PhD. I also extend thanks to ID-UB and University of tomorrow project for providing financial support for the participation in international conferences and summer school.

I take this opportunity to remember and thank all my teachers from my school days – especially, Mr. Anal P. Varghese, Dr. N. Ramanujan, Smitha N.G, Vidhubala Venugopal, - who inspired me to learn and take up a career in Science. I specially thank, Dr. Jinesh K. B., Dr. Nandakumar Kalarikkal, and Dr. Nithyaja B., for giving relevant suggestions and advices. I'm greatly thankful to Dr. Vinodkumar R. for the continuous encouragement and advices from my M. Sc. studies.

I sincerely thank, Dr. Prabeesh Punathil, for all the advices and support in my professional and personal life. I specially thank, Dr. Nandan Babu Kuttath Padi, for helping me during the initial days in Poznan. I'm really grateful to my friends in Poznan- Amanda Pereira George and Manu Sabu - for always there for me in my good and bad times. I would like to thank the “Malayali community” in Poznan and Warsaw for organizing amazing celebrations and parties, that cheered me up and made me connected to Kerala. I am thankful to all my friends in the Faculty of Physics and Biology for the wonderful time shared in this beautiful city. I also extend my thanks to all my MSc. classmates and friends from India for organizing get together during my holidays and for the love and support.

A warm thanks to Fr. Radek Rakowski, for introducing me about the Polish culture, and also for inviting me for the Easter celebrations in Poznan.

Finally, I express the deepest gratitude to my parents, for their unconditional love, advices, financial and moral support, that shaped me to be the person who I'm today. To my mom (amma), who was also my first teacher, and to my dad (papa), who was my biggest support system, thank you for motivating me to chase my dreams. I, Jeena Mariam GeeVarghese, dedicate this doctoral dissertation to my dear parents, Mr. Geevarghese Koruthu and Mrs. Gracykutty George.

I would like to thank my (little) brother, Jinu Varghese, for taking care of my parents in my absence. I remember the love and support of my grandma, who passed away during the final year of my PhD. I also extend my sincere thanks to all my relatives from Njekkinavil and Kalayapuram families for supporting me during the last four years.

Thank God.